Fundamentals of Supersonic Wave Drag

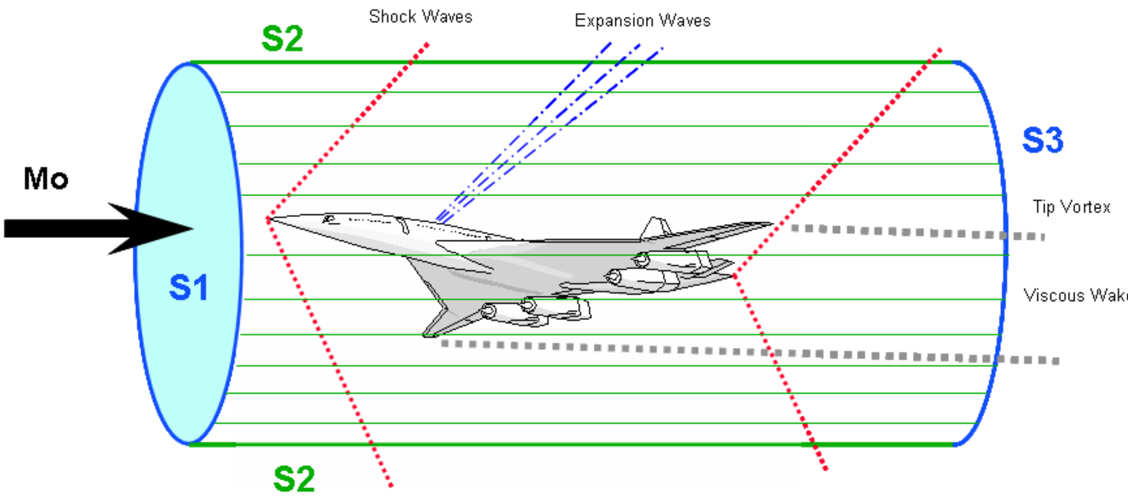

Fourth International Conference on Flow Dynamics

Sendai International Center

Sendai, Japan

September 26-28, 2007

Brenda M. Kulfan

Boeing Commercial Airplanes, Seattle, Washington, 98124

Reports of the Institute
of
Fluid Science
Tohoku University

Vol. 20 2008
pp 11 - 70

Fundamentals of Supersonic Wave Drag

Brenda Kulfan[1]
Boeing Commercial Airplanes, Seattle, Washington, 98124

NASA and Industry, recently ended the High Speed Civil Transport, HSCT, program. The objective of the HSCT program was to develop critical technologies to support the potential development of viable supersonic commercial transport aircraft. The initial phases of the HSCT program utilized the extensive database of methods and knowledge and expertise from the US Supersonic Transport, SST, program and the subsequent NASA sponsored Supersonic Cruise Research, SCR, studies. The aerodynamic design development activities benefited greatly from the use of the prior design, analysis and prediction methods as well as the understanding of the fundamental physics inherent in an efficient supersonic aircraft design. The emerging advanced Computational Fluid Dynamic methods greatly enhanced the supersonic design and analysis process and enabled substantial improvements in achievable aerodynamic performance levels. It was recognized that the critical strengths of the aerodynamic processes included the blending of the computational power offered by CFD methods with the fundamental knowledge and rapid design development and assessment capabilities inherent in the existing linear aerodynamic theory methods.

These prior linear theory methods as well as the wealth of fundamental design knowledge is at risk of being lost for future potential applications, since much of the information is located in often obscure reports and vanishing personal files of prior NASA and industry experts. Consequently, an effort is being made to capture this prior supersonic design and analysis expertise in a series of Fundamentals of Supersonic Aerodynamic Theory Reports. This report is focused on discussions related primarily to volume wave drag of supersonic configurations. Initially the general aerodynamics features of a typical supersonic transport configuration will be discussed. Possible types of flow that can exist over supersonic aircraft at cruise as well as off-design conditions will then be shown. The "tools" that an aerodynamist has at their disposal and that should use in developing efficient supersonic aircraft, will be presented. The simplistic elegance of linear aerodynamic theory will then be used to develop the fundamental prediction methods and understanding for supersonic wave drag calculation, the transonic area rule, the supersonic area rule and the "transfer Rule" for wing / body optimization. The fundamental physics of supersonic favorable aerodynamic interference will be discussed primarily in relation to favorable nacelle / airframe integration. It is then shown how an understanding of the previously discussed fundamental concepts can lead to understanding of non-planar supersonic concepts such as a supersonic ring wing, or an innovative double parasol wing configuration.

This report will also include a brief look at sonic boom. Some answers will be offered to the interesting sonic boom related questions:

- **Is boom-free supersonic flight possible at low supersonic speeds?**
- **Is sonic boom inevitable at supersonic speeds?**
- **Why is a sonic boom signature fundamentally an "N" wave shape?**
- **Why does a concept that alters the front "Lobe" of the Sonic boom signature also modify the aft lobe?**

[1] Engineer/Scientist – Technical Fellow, Enabling Technology & Research, PO Box 3707, Seattle, WA 98124 / MS 67-LF, AIAA Member.

I. Introduction

NASA and Industry, recently ended the High Speed Civil Transport, HSCT, program. The objective of the HSCT program was to develop critical technologies to support the potential development of viable supersonic commercial transport aircraft. The initial phases of the HSCT program utilized the extensive database of methods and knowledge and expertise from the US Supersonic Transport, SST, program and the subsequent NASA sponsored Supersonic Cruise Research, SCR, studies. The aerodynamic design development activities benefited greatly from the use of the prior design, analysis and prediction methods as well as the understanding of the fundamental physics inherent in an efficient supersonic aircraft design. The emerging advanced Computational Fluid Dynamic methods greatly enhanced the supersonic design and analysis process and enabled substantial improvements in achievable aerodynamic performance levels. It was recognized that the critical strengths of the aerodynamic processes included the blending of the computational power offered by CFD methods with the fundamental knowledge and rapid design development and assessment capabilities inherent in the existing linear aerodynamic theory methods.

The significant influence that aerodynamic design integration has on the general features of a typical supersonic transport configuration is shown in figure 1. The wing planform shape is specified to provide a balance between the supersonic cruise, transonic cruise/climb and high lift conditions. The wing leading edge geometry is carefully designed to control the nature of the flow on the wing and to maximize the overall aerodynamic performance. The wing typically has optimized camber and twist to reduce the supersonic cruise wave drag due to lift and induced drag. The wing thickness distribution is usually highly constrained by wing volume and localized depth requirements and designed to minimize the volume wave drag within the constraints.

Wing leading and trailing edges provide an "adaptive' wing geometry for control, to minimize off -design drag and to maximize high lift performance.

The fuselage is generally long and slender, cambered and "area ruled" to minimize supersonic cruise wave drag and for trim considerations.

The nacelles are located aft under the wing and positioned and shaped to minimize wave drag and maximize favorable interference effects. The local wing surface in front of the inlets is tailored to provide acceptable inlet flow distortion.

The vertical tail is thin, swept for low wave drag and has a rudder for control purposes. The movable horizontal tail provides longitudinal control and low trim drag.

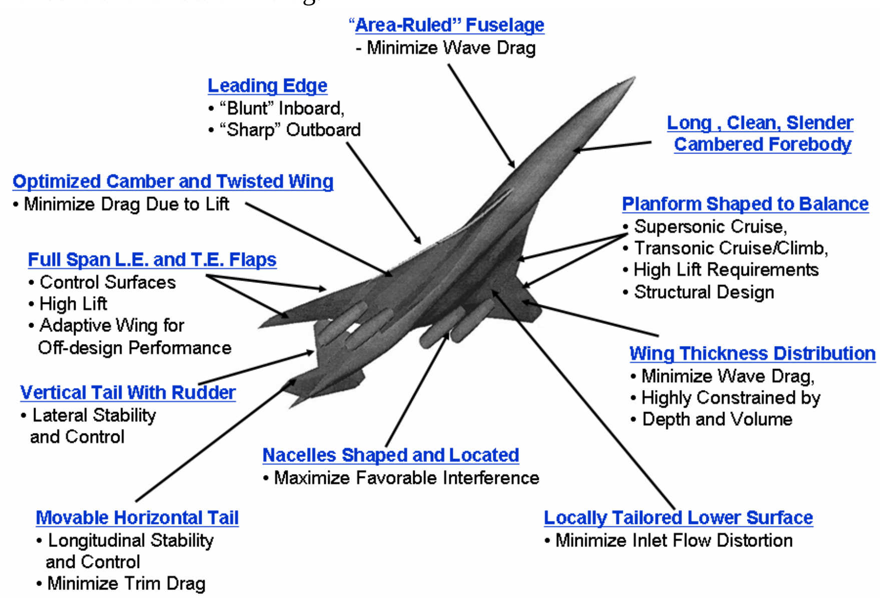

Figure 1. Aerodynamic Design Features of a High Speed Civil Transport

Aerodynamic cruise drag has a highly leveraged effect on the size and performance of an HSCT design. As shown in figure 2, a design improvement that results in a reduction of supersonic drag of 1% , which is approximately 1 drag count, (ΔCD ~ 0.0001), will result in a reduction of approximately 10,400 lb. in the design Maximum Takeoff Gross Weight, MTOW. This also results in a fuel saving of about 7,500 lb. The net benefits are equivalent to reduction in the structural weight of more then one ton.
A reduction of one count of drag for the subsonic climb / cruise portion of the HSCT mission profile will reduce the design gross weight by about 1500 lb. A reduction of one drag count over the transonic / low-supersonic portion of the flight profile results in a design gross weight reduction of more then 1000 lbs.
In addition, an unexpected increase in supersonic drag for a specific HSCT design would result in a 50 mile loss in range capability and thus could be a significant consideration in meeting the design objectives and performance guarantees. Relatively small changes in drag can therefore greatly impact the design selection and definition of the features of an optimized supersonic configuration, as well as determining its ultimate performance capabilities. Consequently this emphasizes the need to clearly understand sources of aerodynamic drag and to develop methods, concepts and techniques to improve the overall aerodynamic efficiency of a supersonic aircraft.

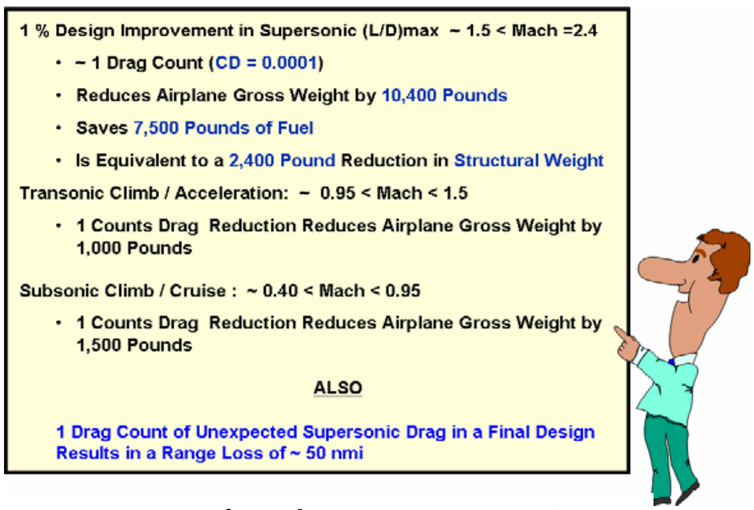

Figure 2.Impact of Aerodynamic Drag on an HSCT

For most engineering applications, it is convenient to consider the drag to be composed of a number of some what independent drag elements. In reality, it is very possible that strong interactions between these elements may occur. In these cases, the concept of independent drag elements may not be applicable. However, for slender supersonic configurations near the cruise conditions, the use of individual drag component assessment can be quite advantageous.
The drag components of a slender supersonic configuration flying at supersonic speeds as shown in figure 3, consists primarily of friction drag, CDF, wave drag due to volume, CDWV, wave drag due to lift, CDWL, induced drag, CDi and other miscellaneous drag items.

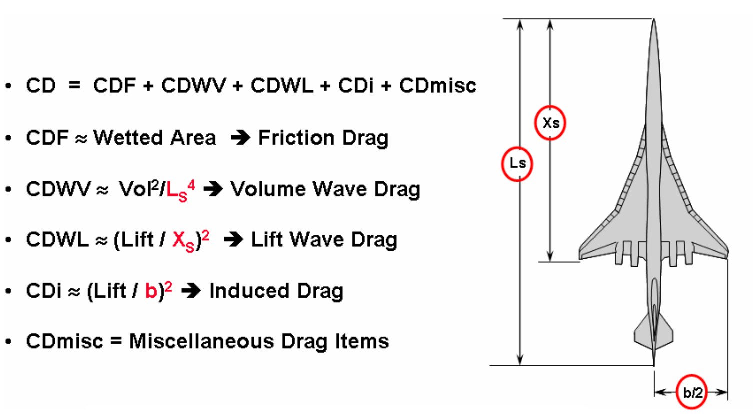

Figure 3: Supersonic Drag Components

The friction drag is approximately equal to flat plate skin friction drag on all of the component surfaces. The friction drag, therefore, depends primarily on the wetted area but decreases slightly with component length increases.

The volume wave drag of a slender supersonic type configuration, to a first order, varies with the overall volume of the configuration squared divided by the configuration length raised to the fourth power.

The induced drag varies with the ratio of lift squared over wing span squared.

The wave drag due to lift varies with lift squared over the streamwise length of the lifting surface squared. The wave drag due to lift vanishes as the supersonic Mach number approaches one.

It is evident that for low drag, supersonic configurations tend to be long, thin and slender, and have highly swept low aspect wings. Consequently as shown in figure 4 the configuration features of a supersonic transport configuration are significantly different that those of a subsonic transport aircraft. Further more, very little of the knowledge and techniques for developing an efficient subsonic transport airplane are directly transferable to the development of a supersonic transport airplane.

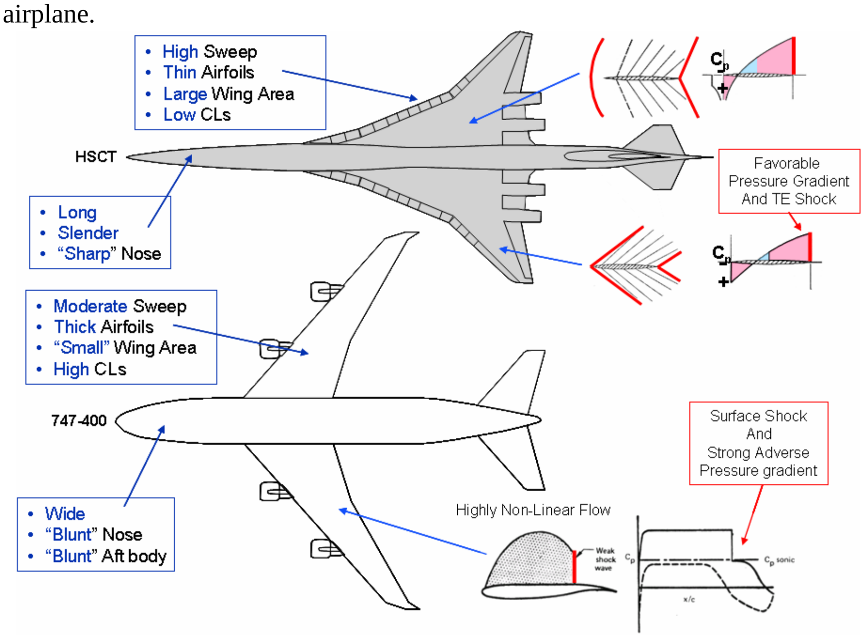

Figure 4. Comparison of Subsonic and Supersonic Transport Aircraft Design Features

Supersonic designs are completely integrated and aerodynamic interference effects between the components must be included in the design processes. However because of the existence of wave drag, the configurations tend to have thin wings, and long slender bodies. The wing airfoil shapes and thickness distribution; body shape and area distribution; nacelle shape, size and locations all contribute to volume wave drag. The wing spanwise lift distribution determines the induced drag. Both the wing spanwise and chordwise lift distributions affect the wave drag due to lift. Nacelle induced pressure fields can provide significant additional wing lift as well as favorable aerodynamic interference. The high dynamic pressure associated with the supersonic conditions results in relatively low lift coefficients. Consequently, the thin-wings, low CL and fully supersonic flows over the configuration allows the use of linear theory for supersonic design and analysis applications. However when using linear theory one must proceed carefully with discretion and understanding.

II. Aerodynamic Tools

In this report we will focus primarily on fundamental concepts and techniques related to the supersonic wave drag applicable to supersonic transport type configurations. We will use the complete set of "aerodynamic tools" shown in figure 5 to gain a fundamental understanding of the topics listed in the figure.

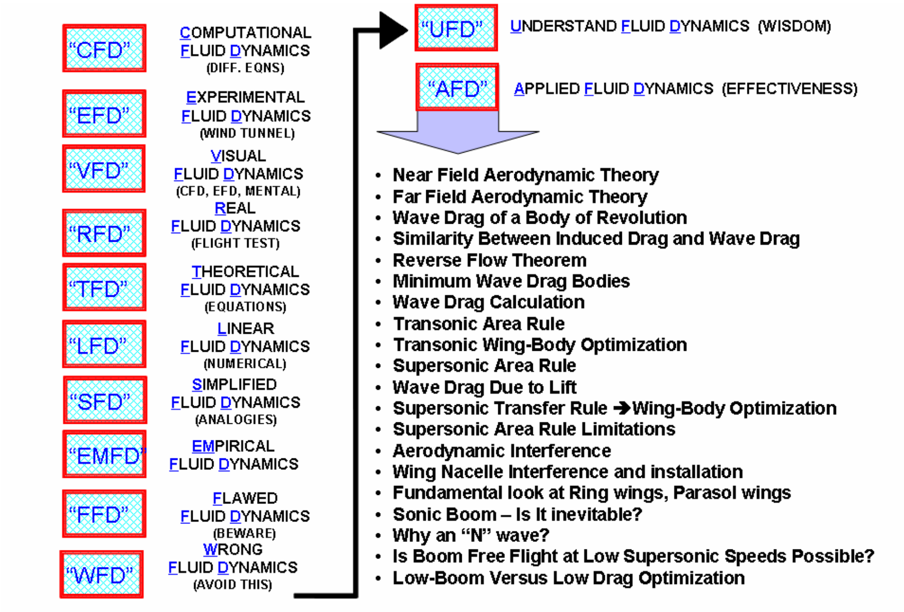

Figure 5. Aerodynamic Tools and the Historical Search for Knowledge

The most common tools of today's aerodynamist are *Computational Fluid Dynamics*, "CFD", along with *Experimental Fluid Dyamics*, "EFD" such as wind tunnel testing. *Visual Fluid Dynamics*, "VFD", obtained either from CFD calculations or from special test measurements can provide very powerful insights in developing an understanding of the flow phenomena These include such things as surface flow streamline patterns and oil flow pictures, and streamline traces and flow field measurements. The ultimate test for the aerodynamist is often *Real Fluid Dynamics*, "RFD" which is flight testing.

The other tools which are often overlooked have played a significant role in the development of the methods and techniques and fundamental understanding related to supersonic aerodynamics. These include:

- *Theoretical Fluid Dynamics*, "TFD" which are methods related to direct analytical solutions of the aerodynamic or fluid dynamic equations.
- *Linear Fluid Dynamics*, "LFD", this is a numerically simpler or lower order version of CFD but can provide unique fundamental understanding of the flow phenomena directly from the nature of the equations.
- *Simplified Fluid Dynamics*, "SFD", these are usually calculation procedures or techniques based on simplified analogies between two somewhat similar flows
- *Empirical Fluid Dynamics*, EMFD" are formulations derived to enrich or extend the usefulness of experimental data.
- *Flawed Fluid Dynamics*, "FFD" and Wrong Fluid Dynamics, "WFD" are typically the result of misapplication of the other tools which is most often due to carelessness or not understanding the limitations of the tools.
- *Understanding Fluid Dynamics*, "UFD", is perhaps the most important aerodynamic tool, Understanding is the ability, developed through education, exploration, experience, insight and reflection, to discern truth and exercise good judgment This tool is the power of wisdom that includes knowledge of fundamental flow physics and the general nature of the flow characteristics over supersonic aircraft configurations, and the ability to assess the adequacy and limitations of the CFD codes used to predict full scale conditions.

In this paper our most heavily relied upon tool will be "LFD" and the focus will be "UFD"

III. Flows at Supersonic Speeds

Figure 6 shows the types of flows that have been observed over a class of supersonic wing planforms having highly swept subsonic leading edges and supersonic trailing edges[1,2]. Many of these flow features have also been observed on hybrid planforms having a combination of subsonic and supersonic leading edges.

At the primary supersonic cruise condition, an aerodynamically efficient wing is typically designed to have attached flow over the entire wing surface. With a supersonic trailing edge, the flow over the upper surface will encounter a trailing edge shock as it readjusts to the local free stream conditions. The trailing edge shock will not be initially sufficiently strong to separate the flow over the wing.

At slightly off design conditions, weak oblique shocks may develop on the upper surface. Depending on the sweep of the trailing edge, strong span wise flow may develop in the region of the trailing edge.

At off design conditions the wing may encounter a combination of separated flow behind shocks that originate near the leading edge as well as flow separation due to the increased strength of the trailing edge shock. Because of the thin highly swept leading edges, the flow may separate as it flows from the lower surface attachment line around the leading edge to the upper surface forming coiled up leading edge vortices.

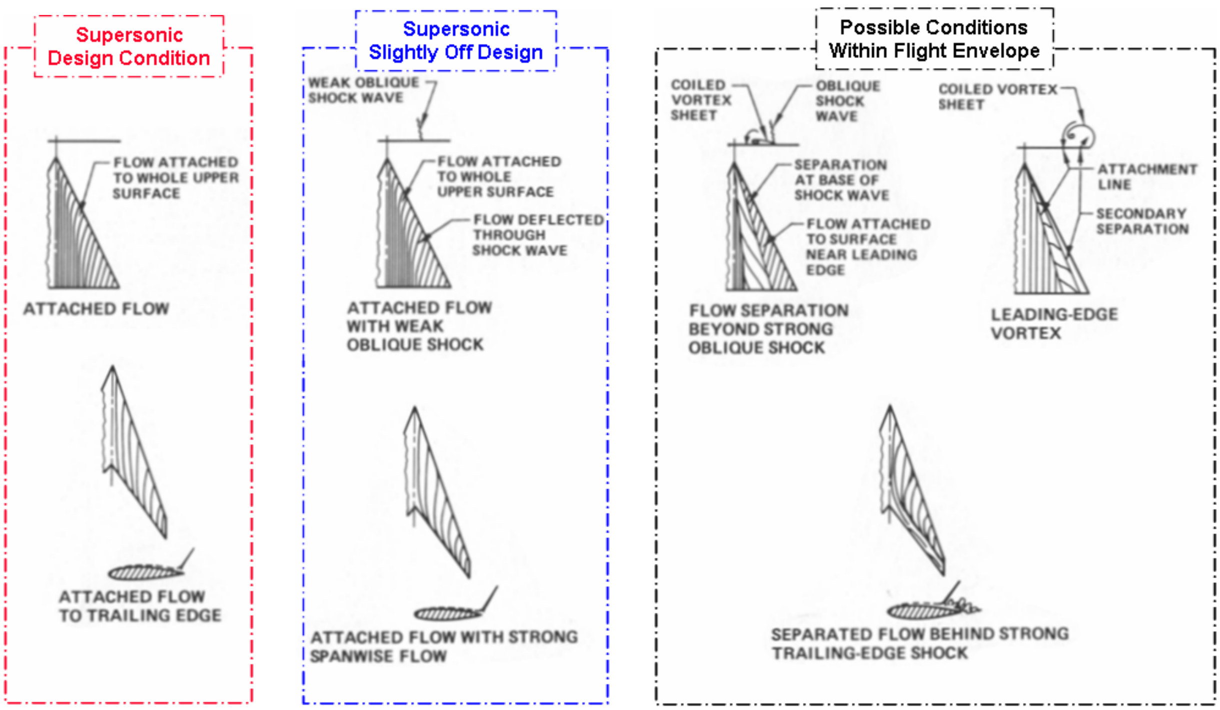

Figure 6. Various Types of Flow on Highly Swept Wings at Supersonic

The flow visualization pictures, VFD, in figure 7 show the changing flow characteristics as the angle of attack in increased above the design condition for a highly swept wing planform.

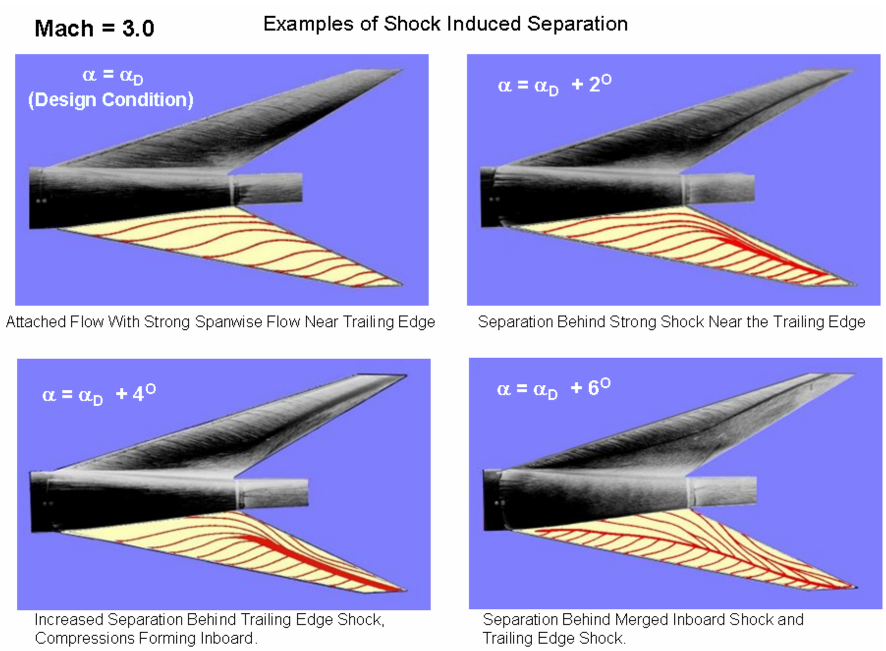

Figure 7. Supersonic Flow on a Highly Swept Wing

For this particular geometry, the shock induced separations develop as the angle of attack is increased above the design attitude. Simple flow analogies, SFD, have been developed [1, 2] that explain the fundamental nature of these shock induced separations. Design criteria necessary to avoid the conditions that may lead these adverse flow effects are discussed in References 1 and 2.

IV. Linear Theory and CFD

One of the great joys of my career was to meet and become friends with Dr. Robert T. Jones. He possessed, among many other things, the remarkable ability to share his wisdom, blended with a touch of humor.
One time when discussing linear theory and CFD, he said with a twinkle in his eyes: Linear theory is long on ideas but short on arithmetic, CFD is long on arithmetic but short on ideas.
Although, linear theory can provide some unique insights and ideas, it does require both understanding and insight to correctly apply the theory because of its numerical and physical limitations.
Similarly, the non-linear CFD methods also require a basic understanding of the inherent limitations of the methodology. However CFD can provide both answers and visibility for flow solutions and flow conditions far beyond the applicability limits of linear theory.
By using both CFD and linear theory and exploiting the benefits of each, we can have the "ideas" and the "arithmetic" plus the added bonus of increased synergistic understanding and design capability.

Since the advent of the utilization of the powerful CFD design and analysis methods, the value of linear theory methods is often questioned. Being "old" or restrictive does not imply "useless". In fact many of the contributions derived from linear theory are still useful today:

- Elliptic load distribution for minimum induced drag
- Thin airfoil theory
- Conformal transformations
- Supersonic area rule wave drag calculation
- Transfer rule wing body optimization
- Sears-Haack, Haack-Adams and Karmen ogive minimum wave drag bodies of revolution
- Conical flow theory
- Reverse flow theorems
- Supersonic nacelle / airframe integration guidelines
- Supersonic favorable interference predictions and concepts
- Sonic boom prediction
- Understanding sonic boom configuration design factors
- Supersonic trade and sensitivity studies
- Baseline configuration for non-linear design optimization

There are two fundamental properties of any linear system of equations such as the linear potential flow equations. These include;

- Homogeneity or Scalar Rule (eg Doubling a surface slopes doubles the pressure)
- Additivity: (eg: obtain a composite solution as a scaled sum of component solutions)

These two properties define the concept of superposition. Perhaps one of the most powerful attributes of linear theory is the superposition of fundamental solutions of the potential flow equation. The strengths of the required local elementary solutions are determined from the local boundary condition that the flow must be tangent to the surface. The fundamental elements commonly used for volume or thickness are supersonic sources or sinks. A source involves the concept of introducing fluid into the free stream and thus causes a splitting of the streamlines. A sink extracts fluid from the free stream and therefore causes the streamlines to close. By adjusting the strengths of the sources and sinks the streamlines will enclose the wing or body surface.

The most common elements used for lifting effects are either the supersonic vortex elements or the supersonic doublet with vertical axes. These elements introduce no net amount of fluid into the stream, but they do generate circulation and thus can produce a jump in potential or pressure in their plane of distribution respectively for doublets or for vortex elements. Superposition allows the separation of volume effects and lifting on aerodynamic forces. Superposition is the fundamental ingredient of the methodology presented in this report.

Some of the key features of linear potential flow analyses include:

- Direct numerical formulation of design optimization. In some simplified cases it is even possible to obtain analytic optimum solutions.
- Linear theory solution formulations as well as the solution equations can provide direct insights and understanding into the effects of geometry and on the nature of the flow phenomena.
- Applications of classical text book theory that provides realistic answers.
- Because of the general ease of application and consistency of results, linear theory is used for sensitivity and trade studies, and to generate the large amount of data required for performance studies.
- Linear theory is often used to define the initial optimized baseline configuration that is used to initiate non-linear design optimization studies.
- It is important to understand the limitations of linear theory and to use discretion when applying the theory so that the solutions are physically meaningful.

Understanding fundamental differences between results obtained with linear theory analysis tools and those obtained with non-linear CFD analyses is very important in helping to establish the usefulness of linear theory. Some of these differences include:

- Linear theory under estimates compression pressures and over estimates expansion pressures.
- Linear theory disturbances are propagated along free stream Mach lines and therefore do not adequately predict shock formations.
- Linear theory does not predict interferences between lift and volume. These differences typically are not significant effects for long slender, thin configurations at low lift coefficients, which correspond to the geometric characteristics of low drag supersonic configurations.
- Linear theory as discussed in this report is linear potential flow theory with planar boundary conditions. Consequently it is easy to incorrectly apply the theory by application to configurations for which planar boundary conditions are not appropriate or in situations in which viscous effects become significant.
- It is very important to understand the limitations of linear theory and to use discretion when applying the theory so that the solutions are physically meaningful.
- Properly used linear theory, however, can predict the drag characteristics of well behaved configurations quite accurately.

Early US SST development studies such as shown in figure 8, have confirmed that linear theory aerodynamic designs that satisfy the set of pressure coefficient limiting real flow design criteria described in references 1 and 2, achieve in the wind tunnel, (EFD), the theoretical linear theory, (LFD), inviscid drag levels.

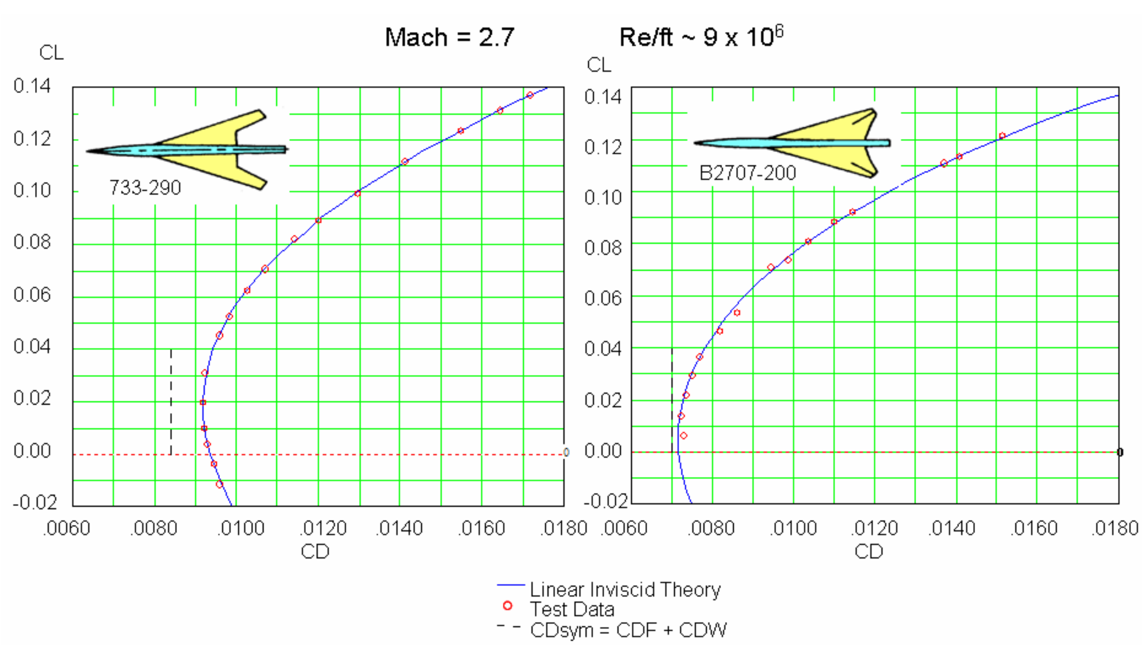

Figure 8. Early SST Linear Theory Optimized Configurations Test vs Theory Comparisons

The figure on the left is a comparison of the drag polar predicted by linear theory with Boeing test data for US SST model 733-290. This was a linear theory optimized design of the configuration that allowed Boeing to win the SST design development Government contract.
The friction drag, CDF, was computed by the T* method [3]. The volume wave drag, CDW, was calculated by Boeing developed zero lift wave drag program which was the basis for the NASA wave drag program [4]. The drag due to lift, CDL was calculated using the Boeing / NASA system of supersonic and analysis programs [5, 6]. The linear theory prediction agrees very well with the test data.
The figure on the right is a comparison the linear theory predictions with test data for the US SST model B2707-200. This was a linear design of the last variable sweep configuration that Boeing studied before the final switch to the US SST double delta configuration, B2707-300. The same drag prediction methods were used as for the 733-290 configuration. Again, the linear theory prediction agrees very well with the test data. Designs developed by linear theory designs are heavily constrained by the real flow constraints and are therefore considered to be on the conservative side in terms of the aerodynamic performance. Hence it is not surprising that the inviscid predictions of drag match the wind tunnel test data

Force calculations obtained with the inviscid and viscous CFD and with linear theory, are compared with wind tunnel test data at Mach 2.4 in figure 9 for two refined linear theory designs developed during HSCT program [7, 8].

The inviscid codes included linear theory, the TRANAIR full potential code, and a parabolized Euler code. The viscous analyses were obtained with a parabolized Navier-Stokes code. Flat plate skin friction drag estimates were added to the inviscid CFD drag calculations, and to the linear theory and Euler predictions to obtain the total aerodynamic drag. The viscous and inviscid force and moment predictions all agree quite well with the test data. The linear theory drag predictions agree well with the test data near the design condition but depart from the test data at the higher CLs.

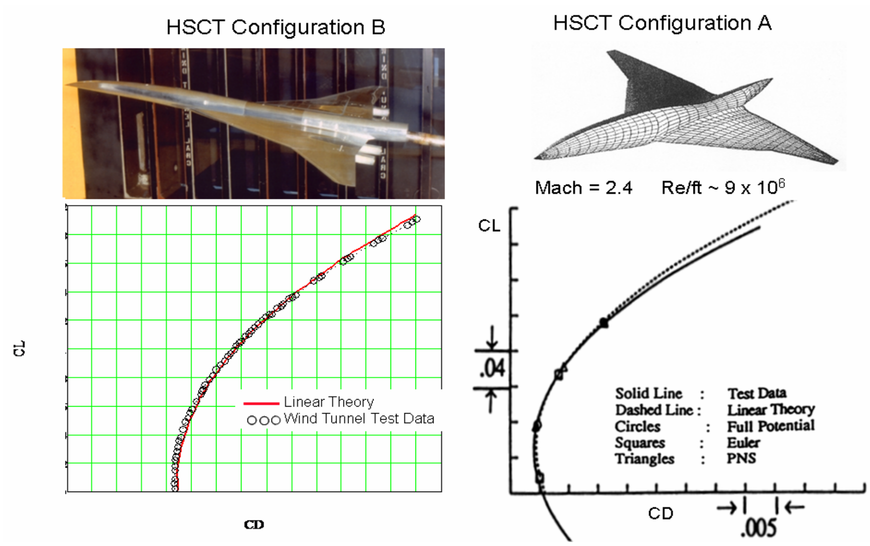

Figure 9. Typical HSCT Configurations Drag Polars Mach = 2.4

Figure 10 contains colored oil flow runs were made during the previously discussed wind tunnel experiments to examine the nature of the flow on the wing upper surface, in particular near the cruise point at Mach 2.4. Inviscid and viscous particle traces were calculated using the non-linear theory[7] near the surface at the same Mach number and lift coefficient. The computed particle traces are compared with the experimental oil flow in the figure.

The viscous flow calculated particle trace matches the details oil flow surface patterns quite well. The inviscid particle trace matches the overall flow characteristics but does not capture the viscous related detailed features that include:

- the inboard flow turning near the wing leading edge / body intersection region
- the flow turning across the mild inboard flow related forward swept shock
- the body off-flow onto the wing near the wing body junction area

These differences in the flow field characteristics apparently did not result in measurable differences in either the forces or moments as shown in fig.9. Consequently the linear theory predictions also matched the test data.

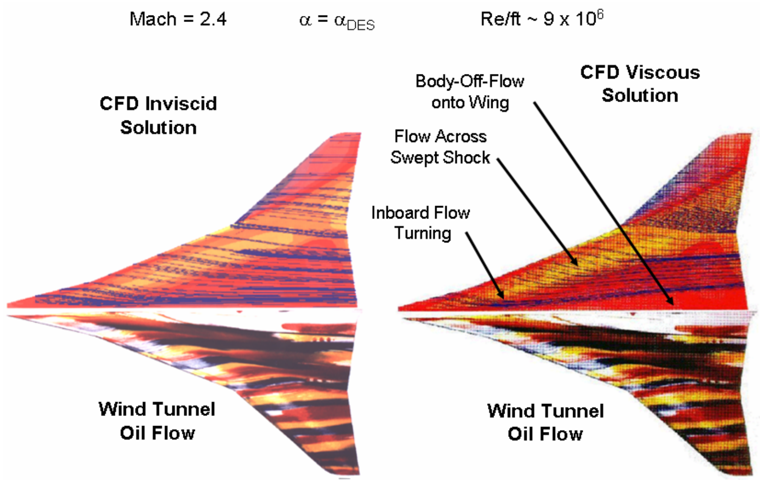

Figure 10. Comparisons of CFD Surface Particle Traces with Wind Tunnel Oil Flow Data

Figure 11 contains comparisons of modified linear theory predictions [9] with test data [10] for a parasol-wing-body configuration. The agreement between theory and test data is quite good. These results imply that linear theory methods are capable of predicting interference lift, mutual body interference, body wave drag cancellation effects such as inherent in the parasol wing concept providing that the limitations of planar linear theory methods are clearly understood and that volume and lift interference are properly accounted for.

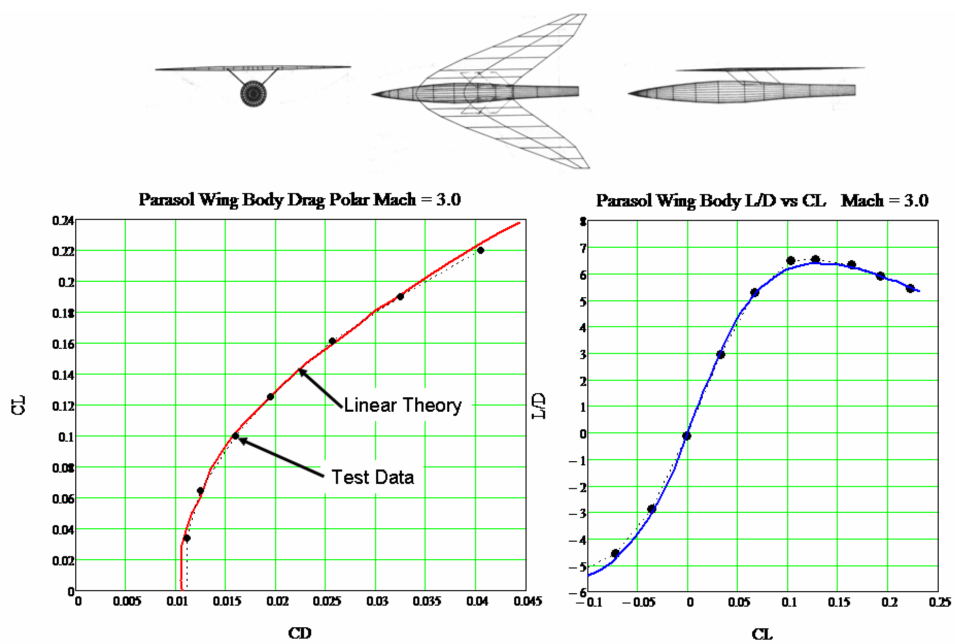

Figure 11. Parasol Wing / Body Test vs Theory Comparisons

These various test versus theory comparisons indicate that linear theory as used in this report can provide accurate assessments of the aerodynamic forces near the 1 g cruise conditions which typically correspond to the design optimization conditions.

V. Supersonic Near-Field Theory

There are two commonly used linear theory approaches to calculate the drag components of a supersonic configuration. These include a "near-field" approach and a "Far-field" approach.

In the near-field approach the local force distributions are calculated on the surface of the configuration. The total forces are obtained by integration of the local force distributions.

In the far-field approach, the total forces are obtained by integration of the momentum changes across the surfaces of a control volume surrounding the configuration.

Each approach will be shown to have certain advantages, certain disadvantages, and certain limitations.

The most common technique to either calculate or to measure aerodynamic drag forces is to sum the forces associated with surface pressures acting normal to the surface plus viscous forces acting tangential to it as shown in figure 12. This is the near field technique.

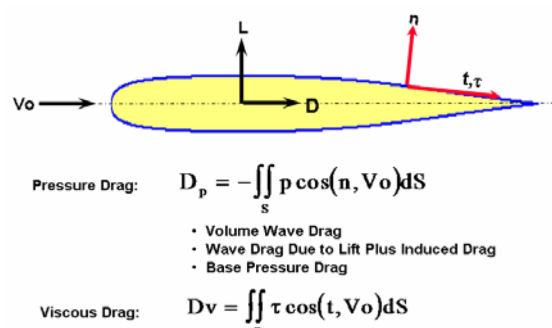

Figure 12 Near Field Calculation Approach

The integration of the forces acting normal to the surface is known as *pressure drag*. The pressure drag is equal to the integral of the surface pressure times the cosine of the angle between the surface local outward normal and the free stream velocity direction

The integration of the forces acting tangential to the surface results from the action of viscosity and is called *viscous drag or skin friction*. . The viscous drag is equal to the integral of the local shear stress times the cosine of the angle between the local surface slope and the free stream velocity direction.

The process of calculating forces by integration of the surface pressures and shear stress over the surface is commonly called Near Field Theory. This is the primary process used in the advanced CFD codes.

The near field velocity and pressure fields are obtained by solution of the supersonic linear theory velocity potential equation.

$$\left(M_\infty^2 - 1\right)\frac{\partial^2\phi}{\partial x^2} - \frac{\partial^2\phi}{\partial y^2} - \frac{\partial^2\phi}{\partial z^2} = 0 \qquad 1$$

The perturbation velocities in any direction, can be obtained as the first derivative of the velocity potential in that direction.

Streamwise perturbation velocity $$\frac{u}{U_\infty} = \frac{\partial\phi}{\partial x} \qquad 2$$

Spanwise perturbation velocity $$\frac{v}{U_\infty} = \frac{\partial\phi}{\partial y} \qquad 3$$

Vertical perturbation velocity $$\frac{w}{U_\infty} = \frac{\partial\phi}{\partial z} \qquad 4$$

The pressure distribution, Cp(x,y), is derived from the streamwise perturbation velocity as:

$$Cp(x,y) = -2\frac{u(x,y)}{U_\infty} = -2\frac{\partial\varphi(x,y)}{\partial x} \qquad 5$$

Linear potential flow analyses are further simplified by the assumption of linear boundary conditions applied in the plane of a wing surface and / or along the axes of a body. The usual boundary condition is that the flow must be tangent to the local wing or body surface. The slope, $\lambda(x,y)$, is related to the surface slope as:

$$\lambda(x,y) = \frac{w(x,y)}{U_\infty} = \frac{\partial\varphi(x,y)}{\partial z} \qquad 6$$

The problem is solved when the velocity potential $\phi(x,y)$ that satisfies the boundary conditions is determined.

The pressure distributions due to wing thickness can be obtained by representing the wing by a distribution of sources and sinks in the plane of the wing. The equation for effect of a unit strength point source located at point ξ,η, on velocity potential at a point x,y is defined by the equation

$$d\Phi(x,y) = -\frac{1}{\pi}\frac{\lambda(\xi,\eta)\,d\xi d\eta}{\sqrt{(x-\xi)^2 - \beta^2(y-\eta)^2}} = -\frac{1}{\pi}\frac{\lambda(\xi,\eta)}{R_h(\xi,\eta)}d\xi d\eta \qquad 7$$

The effect of the incremental source / sink is proportional to the local surface slope and inversely proportional to the hyperbolic radius, R_h.

where :

$$R_h = \sqrt{(x-\xi)^2 - \beta^2(y-\eta)^2} \qquad 8$$

As shown in figure 13, the source at the point ξ,η can influence the regions downstream bounded by left and right Mach lines emulating from the point. This region is commonly called the Mach aft-cone region of the point ξ,η.

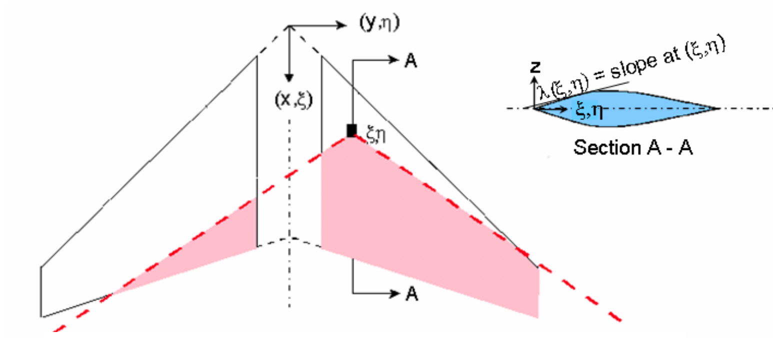

Figure 13. Region of Influence of a Point Source or Sink

Consequently, as shown in figure 14, a point x,y on a wing is influenced only by the elements located in the region of the wing lying within its Mach Forecone bounded by forward lines parallel to the Mach lines.

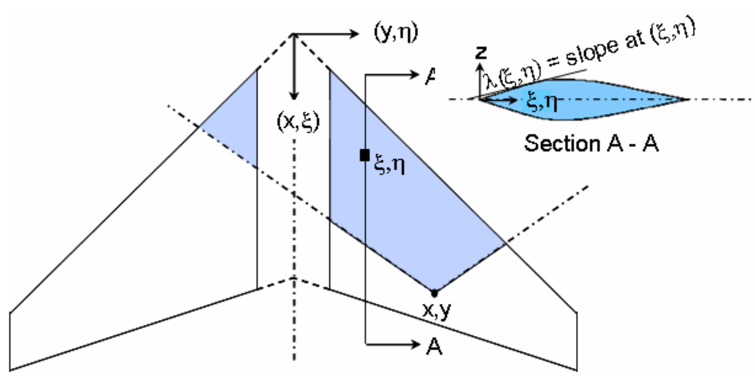

Figure 14. Mach Forecone Region of Influence for a Point x,y

The total velocity potential Φ(x,y) at a point x,y, is then obtained by integration of the incremental velocity potential over the Mach forecone regions, τ.

$$\varphi(x,y) = -\frac{1}{\pi}\iint_{\tau}\frac{\lambda(\xi,\eta)\,d\xi d\eta}{R_h(\xi,\eta)} \qquad 9$$

The pressure coefficient at any point is then obtained from the integral equation as

$$Cp(x,y) = -2\frac{\partial}{\partial x}\Phi(x,y) = \frac{2}{\pi}\frac{\partial}{\partial x}\iint_{\tau}\frac{\lambda(\xi,\eta)\,d\xi d\eta}{R_h(\xi,\eta)} \qquad 10$$

The integral of the velocity potential is an improper integral that has a singularity along the bounding forward Mach lines. The integration therefore requires special methods of evaluation. Calculation of the pressure coefficient requires differentiation of a complicated integral function. It would be advantageous to interchange the order of differentiation and integration by moving the differentiation into the integration. This is legitimate only if the integrand is an analytic function continuous in all derivatives. This is not the case for the integral equation 10.

By utilizing the concept of the "Finite Part of a Divergent Integral [11]" it is possible to move the differentiation into the integrals, as shown in equation 11, providing that the inside integral is evaluated by the special techniques to evaluate a "Finite Part" integral.

$$Cp(x,y) = \frac{2}{\beta}\lambda(x,y) - \frac{2}{\pi}\int_{\tau} d\xi \,⨍ \frac{(x-\xi)\lambda(\xi,\eta)\,d\eta}{R_h^3} \qquad 11$$

The thickness pressure is seen to consist of the 2 dimensional part just associated with the local wing slope plus a 3 dimensional "correction" integral. The integral symbol $⨍$ in equation 12 indicates a finite part integral. The drag associated with a thickness distribution and be obtained by integration the thickness pressure distribution over the wing thickness distribution. Near the leading of a wing with a subsonic round nose airfoils the local slopes become infinite and equation 11 becomes singular. Consequently special techniques [12, 13, 14] are required when using the linear solutions for computing the near field pressure drag.

In principle, given the local wing thickness distribution which defines the wing surface slopes, it is possible to directly calculate the surface pressure distribution. This is known as the "Direct Problem".

Determining the surface shape necessary to produce a given pressure distribution is called the "Indirect Problem". This is a much more complicated process since the unknown is contained within the integral.

The lifting effects of a wing can be represented by a distribution of lifting elements on the plan of the wing. .the strength of the lifting elements is related to the local lifting pressure coefficient.

$$\Phi(x,y,z) = \frac{U}{4\pi}\iint_{\tau}\frac{z(x-\xi)}{\left[(y-\eta)^2+z^2\right]\sqrt{(x-\xi)^2-\beta^2(y-\eta)^2-\beta^2z^2}}\Delta Cp(\xi,\eta)\,d\xi d\eta \qquad 12$$

The total velocity potential due to a plane of vortex elements is then equal to the integral of the elementary elements over the region contained in the Mach forecone of the point itself

For a distribution of vortex elements in the z = 0 plane, the vertical velocity ratio is equal to the derivative of the velocity potential in the vertical direction, evaluated in the plane of the wing. The local wing slope is equal to the vertical velocity ratio

$$\lambda(x,y) = \frac{w(x,y)}{U_\infty} = \lim_{z\to 0}\frac{1}{4\pi}\frac{\partial}{\partial z}\iint_{\tau}\frac{z(x-\xi)\Delta Cp(\xi,\eta)}{\left[(y-\eta)^2+z^2\right]\sqrt{(x-\xi)^2-\beta^2(y-\eta)^2-\beta^2z^2}}d\xi d\eta \qquad 13$$

One way to evaluate this equation is to first perform the integration of this highly improper integral, then differentiate the result, and then perform the limit evaluation as z goes to zero. This is numerically very difficult and highly prone to numerical errors.
Again, it is numerically advantageous to exchange the order of differentiation and integration. However, since the integrand is a singular function this is not possible for a conventional Riemann type integral. However , by utilizing the concept of a "generalized principal part integral" it is possible to move the differentiation though the integrals and then integrate the basic integrand. The resulting integral shown in equation 14, must be evaluated by the special techniques for evaluating principal part integrals.

$$\lambda\left(x,y\right)=-\frac{\beta}{4}\Delta Cp\left(x,y\right)+\frac{1}{4\pi}\,⨎_{\tau} d\xi\int\frac{\left(x-\xi\right)\Delta Cp\left(\xi,\eta\right)d\eta}{\left(y-\eta\right)^{2}R_{h}\left(\xi,\eta\right)} \tag{14}$$

This equation illustrates the basic form of the solution. The local surface slope required to produce a specified load distribution is determined from the two dimensional pressure coefficient plus a 3 dimensional correction obtained by integration over the Mach forecone. The Integral $⨎$ signifies a generalized principal part integral since the integrand is singular.

The direct problem for lifting effects is: given a specified pressure distribution, calculate the necessary shape to produce that pressure distribution.

The indirect problem, and typically more complicated problem, is: Given the shape of the lifting surface determine the resulting lifting pressure distribution.

The drag in any case, is obtained by integration of the lifting pressures over the lifting surface. In some cases, there may be finite leading edge forces [12, 13, 14] that must be accounted for. This leading force, if it exists, is called the "leading Suction".

The linear theory near field theory approach has a number of positive features that include:

+ Common approach for wing camber / twist optimization
+ Can provide distributions of basic drag and interference forces
+ Can judge analyses or designs from the Cp' distributions
+ Can utilize real flow criteria or limitations to establish the validity of the solution
+ Can apply semi-empirical corrections to the solutions
+ Can include higher order corrections to the theory

Conversely, the linear theory near field theory approach has a number of negative features that include:

– Usually requires sophisticated numerical methods
– Special methods are required to deal with edge forces (e.g. leading edge suction) and shapes (e.g. round leading edge)
– Easy to misuse the theory and methods – by not understanding limitations of the theory, or not understanding the implied boundary conditions
– May miss significant interference interactions

VI. Supersonic Far-Field Theory

An alternate way to calculate the drag of a configuration is to use a "far-field" approach as shown in figure 15.

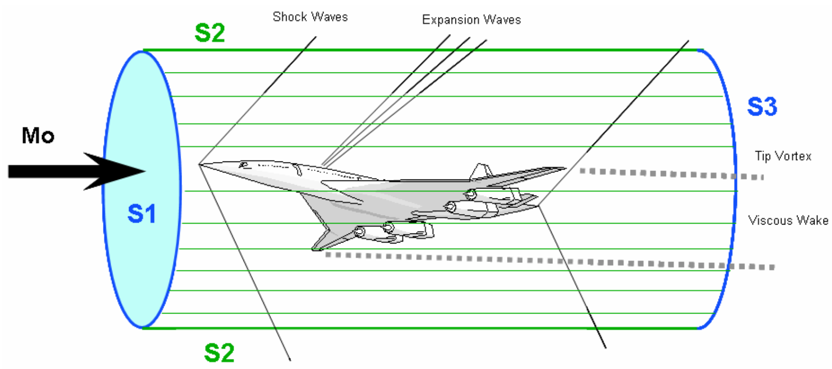

Figure 15 Far Field Drag Calculation Approach

In this approach, the streamwise momentum change, through a control volume containing the configuration, is equal to the drag of the configuration. The control volume typically is cylindrical.

The upstream end, S1 has only free stream undisturbed flow passing through it. The downstream surface, S3, is located far enough down stream of the configuration that the pressure induced flow field becomes essentially two dimensional. This is often called the Treffetz plane.

The momentum change between side S1 and Side S3 is due primarily to the friction drag and the induced drag. Miscellaneous drag items such as wake drag, base drag and excrescence drag are also related to the momentum changes between S1 and S3.

The cylindrical sides are located many body lengths away from the body centerline. At subsonic Mach numbers the flow becomes parallel to the sides of the cylinder and hence there is no flow through this surface and hence no momentum change. At supersonic speeds, because of the shock waves and the expansion waves generated by the configuration, there is mass flow both in and out of the cylinder through the sides. The change in the streamwise momentum associated with this mass flow across the sides of the cylinder is called the wave drag. Since the shock wave structure around a supersonic configuration can change with angle of attack, the wave drag can also vary with angle of attack. Hence the wave drag consists of the wave drag due to the volume distribution of the configuration plus the variation of wave drag with lift which is called "wave drag due to lift".

The drag equation expressed in terms of the momentum changes through the control volume is;

$$D = -\iint\limits_{S3-S1} (p - p_\infty) dS_3 - \rho_\infty U_\infty^2 \iint\limits_{S3-S1} \phi_x (1+\phi_x) dS_3 - \rho_\infty U_\infty^2 \iint\limits_{S_2} \phi_x \phi_r dS_2 + D_F + \sum D_{Misc} \qquad 15$$

Where the miscellaneous drag typically consists of such items as excrescence drag plus localized regions of base drag

$$\sum D_{Misc} = D_{Excres} + D_{Base} \qquad 16$$

In an inviscid potential flow analyses, the viscous and miscellaneous drag are not part of the solution and must be accounted for by some other means. In the discussions that follow we will neglect the miscellaneous drag items

The drag consists of contributions from the three integral relations shown in equation 15

The aft side of the cylindrical control volume is considered to be located far down stream so that the flow is two dimensional in the crossflow plane, the streamwise perturbation velocity is zero. $\phi_x = 0$

This is called the Trefftz plane. Hence the second Integral is zero.

$$\rho_\infty U_\infty^2 \iint_{S3} \phi_x \left(1+\phi_x\right) dS_3 = 0 \tag{17}$$

and the pressure differential is equal to the kinetic energy in the aft crossflow plane.

$$p - p_\infty = -\frac{1}{2}\rho_\infty U_\infty^2 \left(\phi_y^2 + \phi_z^2\right) \tag{18}$$

Therefore, the total inviscid drag equation becomes:

$$D = -\rho_\infty U_\infty^2 \iint_{S2} \phi_x \phi_r dS_2 + \frac{1}{2}\rho_\infty U_\infty^2 \iint_{S3} \left(\phi_y^2 + \phi_z^2\right) dS_3 \tag{19}$$

The first integral is the total wave drag. The wave drag consists of wave drag due to the thickness and volume distributions of the configuration, plus the wave drag due to lift.

$$D_W = -\rho_\infty U_\infty^2 \iint_{S2} \phi_x \phi_r dS_2 \tag{20}$$

The second integral is equal to the induced drag.

$$D_i = \frac{1}{2}\rho_\infty U_\infty^2 \iint_{S2} \left(\varphi_y^2 + \varphi_z^2\right) \tag{21}$$

The induced drag, as in subsonic flow, can be calculated directly from the circulation distribution in the wake in the Treffetz plane.

$$D_i = -\frac{\rho_\infty}{4\pi} \int_{-\frac{b}{2}}^{\frac{b}{2}} \int_{-\frac{b}{2}}^{\frac{b}{2}} \frac{d\Gamma}{dy}\frac{d\Gamma}{d\eta} \ln\left|y-\eta\right| dy d\eta \tag{22}$$

The induced drag integral equation has the well known solution that the minimum induced drag for a given lift is achieved, independently of the wing planform or camber details, by an elliptic spanwise load distribution which is exactly the same as for subsonic flow.

The Far Field Linear Theory has a number of both positive and negative features that include:

+ Easy numerical formulations
+ No numerical difficulty associated with linear theory singularities or leading edge forces
+ Easy volume wave drag calculation
+ Can separate induced drag and wave drag due to lift
+ Direct approach for wing / body area rule optimization
+ New wing thickness / airfoil optimization method
+ New induced drag + wave drag due to lift optimization method
+ Useful for lower bound supersonic drag assessments

– Can not directly judge the physical real flow validity of the analyses or designs
– Very easy to misuse the theory and methods
– Typically requires the simulation of configuration symmetry
– Requires special treatment of non- planar arrangements such as wing / nacelles
– Can not easily incorporate semi-empirical corrections to predictions or analyses

The Far Field Theory has a number of both positive and negative features. On the positive side, the mathematical formulations are rather easy and have no difficulty in dealing with linear theory leading edge forces. The far-field codes provide an easy and consistent approach to evaluate the volume wave drag of a configuration. The far field wave drag method provides a simple and direct method for body area rule design optimization.

A new method for utilizing the far field for optimizing the airfoil shape and thickness distribution of a wing at supersonic speeds has been developed [15]. This method can also be extended to determine the optimum wing lift distribution for minimum wave drag due to lift plus induced drag. The far-field optimization methods can provide a useful process for defining the lower bound drag potential for an arbitrary configuration at supersonic speeds.

On the negative side, Calculation of either induced drag or wave drag to lift by a far field method, requires that the lift distribution be known. Consequently, this method is not normally used to compute drag due to lift since the near-field method would have to be used initially to obtain the lift distribution. Hence the drag due to lift would already be available from the near field analysis. The far-field optimum designs can not be directly judged to assess the potential for success of a particular design since no details are provided about the flow and the configuration. As is the case with any linear theory, it is easy to misuse the theory and the methods. The far field wave drag method essentially requires that the configuration be planar and symmetric. However, it is possible to use images to allow the meaningful analysis of non-planar arrangements such as wing / nacelles.

The linear theory drag calculation options are shown in figure 16. Since the typical commercial supersonic transport has thin slender components and cruises at relatively low lift components, the skin friction drag is calculated by fully turbulent flow skin friction drag. The volume wave drag for the wing-body-tails is usually calculated using far field theory. The installed nacelle drag is usually calculated using a modified near field theory. The induced drag and trim drags are usually calculated using near field theory. In this report we will briefly discuss drag due to lift calculation using a far field theory. The linear theory tools utilized in this report were primarily those contained in the Boeing-NASA system of programs for the aerodynamic design and analysis of supersonic aircraft[5, 6]. The theoretical drag predictions shown in figures 8, 9 and 11 were computed using this system of programs.

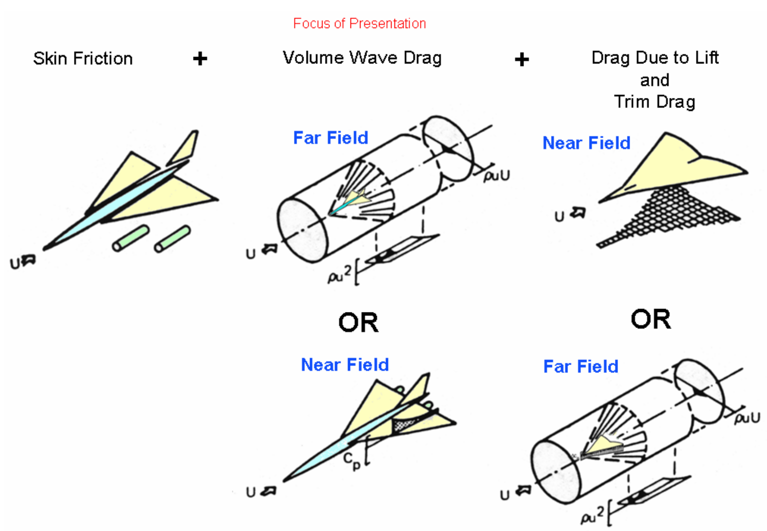

Figure 16. Linear Theory Supersonic Drag Calculations options

XIII. Wave Drag of a Body of Revolution

Von Karman [16] showed that a body of revolution in supersonic flow could be represented mathematically as a linear string of sources and sinks aligned along the body axes as shown in figure 17.

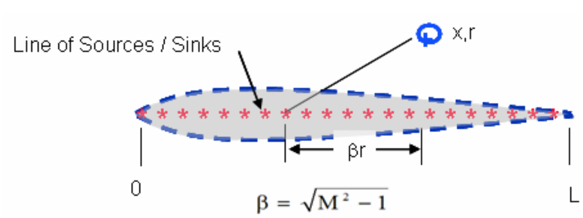

Figure 17. Source / Sink Representation of a Body of Revolution

The velocity potential for the linear string of sources and sinks in terms of the local source strength $f(\xi)$ is:

$$\phi(x,r) = -\frac{1}{2\pi}\int_0^{x-\beta r} \frac{f(\xi)\,d\xi}{\sqrt{(x-\xi)^2-\beta^2 r^2}} \quad 23$$

Where $\beta = \sqrt{M^2-1}$

The streamwise and radial components of perturbation velocity are:

$$u(x) = \phi_x = -\frac{1}{2\pi}\int_0^{x-\beta r} \frac{f'(\xi)\,d\xi}{\sqrt{(x-\xi)^2-\beta^2 r^2}} \quad 24$$

$$vr(x) = \phi_r = -\frac{1}{2\pi}\int_0^{x-\beta r} \frac{(x-\xi)\,f'(\xi)\,d\xi}{\sqrt{(x-\xi)^2-\beta^2 r^2}} \quad 26$$

Substituting equations 25 and 26 into the wave drag equation (eqn. 21) and performing the integration[17] results in the basic wave drag originally developed by von Karman

$$\frac{Dw}{q} = -\frac{1}{\pi}\int_0^{L} f'(x)\,dx\int_0^{x} f'(\xi)\ln|x-\xi|\,d\xi \quad 26$$

For a slender body, the local source strength is directly related to the local rate of change of the area distribution

$$f(x) = A'(x) \quad 27$$

The wave drag equation for a body of revolution becomes

$$\frac{Dw}{q} = -\frac{1}{2\pi}\int_0^{L} A''(x)\,dx\int_0^{x} A''(\xi)\ln|x-\xi|\,d\xi \quad 28$$

This result is only valid if the slopes of the body area distribution are zero at both the nose and aft end of the body.

The slope of the area distribution can be related to the radius distribution as: $$A'(x) = 2\pi r\frac{dr}{dx} \quad 29$$

Consequently, the common wave drag equation for a body of revolution (eqn 29) is only valid if either the radius or slope of the radius distribution is zero at both ends as shown in figure 18

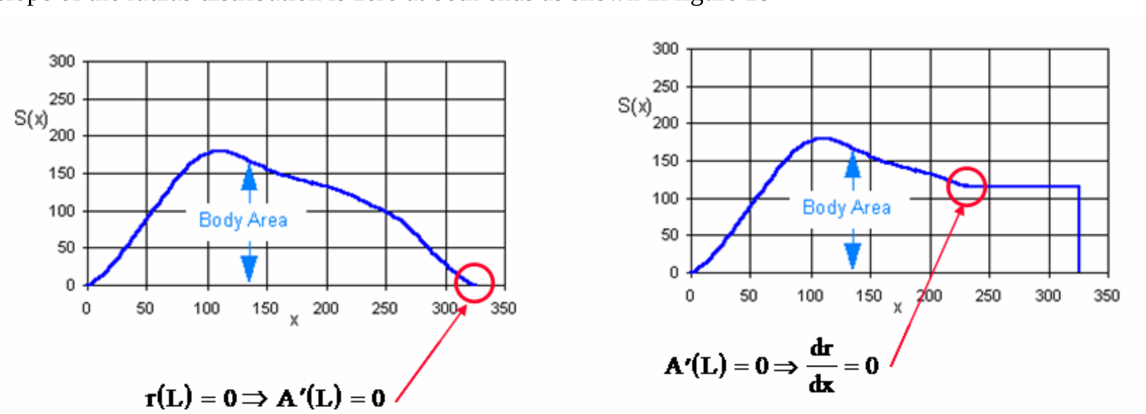

Figure 18. Geometry Restrictions for Common Slender Body Wave Drag Analyses

For body geometries in which the aft slope is non zero, the wave drag calculation must include [11, 17,] the second term shown in equation 30.

$$\frac{Dw}{q}=-\frac{1}{2\pi}\int_0^L A''(x)dx\int_0^x A''(\xi)\ln|x-\xi|d\xi+\frac{A'(L)}{2\pi}\int_0^L A''(\xi)\ln|L-\xi|d\xi-\frac{\left[A'(L)\right]^2}{2\pi}\ln\frac{\beta R(L)}{2} \qquad 30$$

Lighthill [11,18, 19] developed a so called "not so slender body" near field theory that tends to be more accurate than the slender body theory and in addition accounts for supersonic flow past bodies of revolution when A'(x) is discontinuous. Figure 19 is a brief summary of the Lighthill theory.

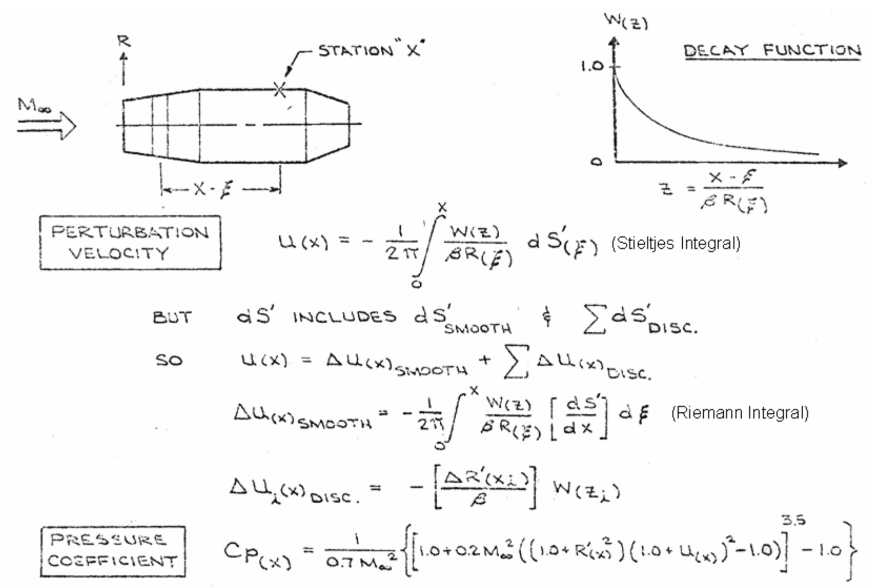

Figure 19. Supersonic Pressure Distribution for a Body With Discontinuities in A'(x)

The results of calculations of slender body wave drag and wave drag calculated by the Lighthill theory [20] are shown in figure 20 along with wind tunnel test data for a number of bodies having finite area distribution slopes at the aft end.. These results as shown give an indication of the magnitude of the surface discontinuity term in equation 30 that is not accounted for with the conventional linear theory wave drag estimates using equation 28. Therefore it is obvious that using the conventional slender body wave drag equation for calculation of drag when there is finite slope at either end of the body may lead to significant errors in the prediction.

However in the remainder of this report, we will primarily consider only geometries where the condition of zero slope of the body area distributions at both the nose and the aft end applies.

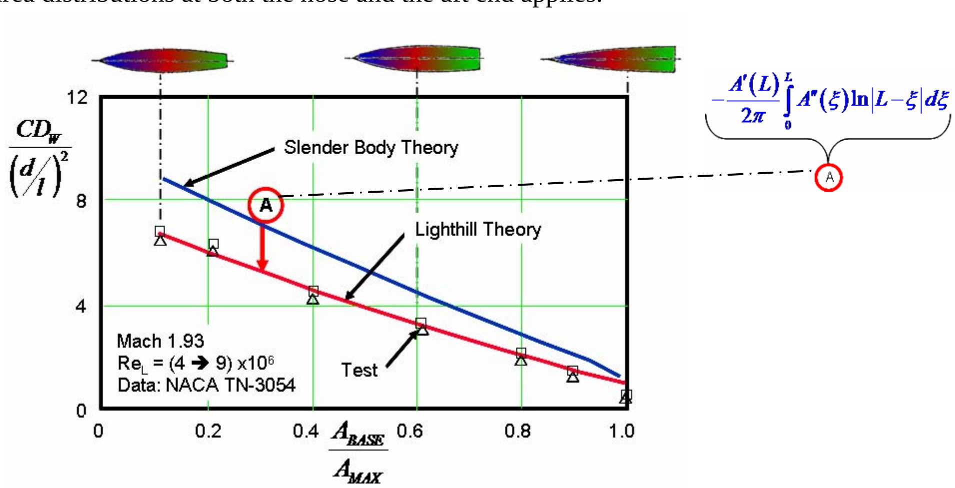

Figure 20. Effect of Aft-Body Slope on Body Wave Drag

VII. Body Wave Drag Observations and Similarities

The body wave drag equation 28, is mathematically identical to the induced drag equation for a lifting surface [17, 22],

$$\frac{D_i}{q} = -\frac{1}{2\pi}\int_{-\frac{b}{2}}^{\frac{b}{2}}\int_{-\frac{b}{2}}^{\frac{b}{2}} \frac{d\Gamma}{dy}\frac{d\Gamma}{d\eta}\ln\left|y-\eta\right| dy d\eta \qquad 31$$

with the similarity relation between the wing circulation Γ, and the slope of a body area distribution.

$$\Gamma \approx \frac{dA}{dx} \qquad 32$$

The lift is proportional to the integral of the circulation over the wing span. $L \approx \int_{-b/2}^{b/2} \Gamma(y) dy$ 32

Similarly, the base area of a body of revolution is equal to the integral of the slope of the area distribution

$$A_{BASE} \approx \int_0^L A'(x) dx \qquad 34$$

It is well known that the optimum load or circulation distribution for minimum induced drag is elliptic

$$\Gamma_{OPT}(y) = \Gamma_0\sqrt{1-\eta^2} \qquad and \qquad -1 \le \eta \le 1 \qquad 35$$

Consequently by similarity of equations, the slope of the optimum body area distribution for minimum wave drag must also be elliptic:

$$\left\{\frac{dA}{dx}\right\}_{Opt} \approx \sqrt{1-(1-2\psi)^2} = 2\sqrt{\psi-\psi^2} \qquad 0 \le \psi \le 1 \quad and \quad \psi = \frac{x}{L} \qquad 36$$

The optimum area distribution is then obtained by integration as:

$$A(\psi) \approx 2\int_0^{\psi} \sqrt{\psi}\sqrt{1-\psi}\, d\psi \qquad 37$$

This optimum body area distribution that is normally derived from the wave drag equation solutions, is called the Karmam Ogive nose[22] and is shown in figure 21. Karmen Ogive defining values from reference 23 are shown as the black dots in the figure.

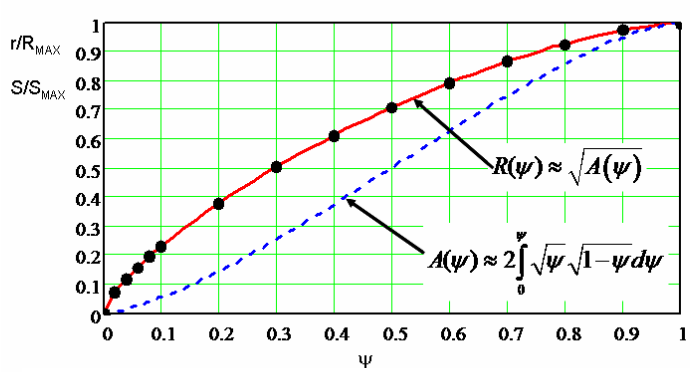

Figure 21. Karman Ogive Radius and area distributions

This result leads to two seemly unexpected results or paradoxes.

Paradox[*] 1: *The Karmen-ogive minimum wave drag body for a specified base area can be derived directly from the subsonic optimum lift distribution for minimum induced drag.*

Another implication of the similarity between induced drag equation and the supersonic wave drag of a body of revolution equation leads us to:

Paradox 2: *Numerical methods used to compute the supersonic wave drag for a body or revolution can be used to numerically compute induced drag for a specified lift distribution.*

[*] Note: in this paper we use the word "Paradox" to mean a statement that is seemingly opposed to common sense or defies intuition and yet is true.

Although the flow physics of the drag mechanisms for subsonic induced drag and for supersonic wave drag are different, the fundamental mathematical solutions are very similar. These are examples where similar knowledge and techniques are transferable from subsonic to supersonic speeds using TFD (Theoretical Fluid Dynamics).

We can also easily derive another interesting observation directly from equation 28.

Assume that we have a body of revolution with area distribution $A_1(\psi)$ with $A_1(0) = A_1(L) = 0$ that is shown in Figure 22.

The wave drag can computed from equation 28 is

$$\frac{Dw_F}{q} = -\frac{1}{2\pi}\int_0^L A_F''(x)dx\int_0^x A_F''(\xi)\ln|x-\xi|d\xi \qquad 38$$

The subscript "F" indicates the drag in forward flow.

Assume we have a second body whose area distribution, $A_R(x)$ is exactly the reverse of body 1. The wave drag for this body is

$$\frac{Dw_R}{q} = -\frac{1}{2\pi}\int_0^L A_R''(\tilde{x})d\tilde{x}\int_0^x A_R''(\tilde{\xi})\ln|\tilde{x}-\tilde{\xi}|d\tilde{\xi} \qquad 39$$

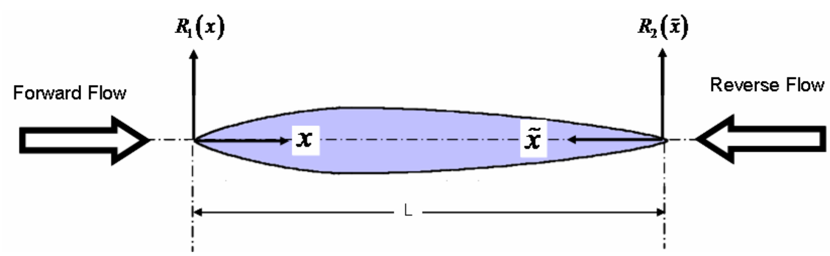

Figure 22. Body of Revolution in Forward and reverse Flow

The axial coordinate system for the body in forward and reverse flow are related by the equation

$$\tilde{x} = L - x \qquad 40$$

Therefore

$$d\tilde{x} = -dx \qquad 41$$

The body areas at the same physical locations are the same $S_R(\tilde{x}) = S_F(L-\tilde{x})$

Therefore $\frac{d}{d\tilde{x}}S_R(\tilde{x}) = \frac{dx}{d\tilde{x}}\frac{d}{dx}S_F(x) = -\frac{d}{dx}S_F(x)$ and $S_R'(\tilde{x}) = -S_F'(x)$ 42

Similarly $$\frac{d^2}{d\tilde{x}^2} S_R\left(\tilde{x}\right) = \frac{dx}{d\tilde{x}}\frac{d}{dx} S_F'\left(x\right) = \left(\frac{dx}{d\tilde{x}}\right)^2 \frac{d^2}{dx^2} S_F\left(x\right) \quad \text{and} \quad S_R''\left(\tilde{x}\right) = S_F''\left(x\right) \tag{43}$$

Substituting equations 40➔ 43 into 39 we obtain:

$$\frac{DR_W}{q} = \frac{1}{2\pi}\int_0^L\int_0^L A_F''\left(x\right) A_F''\left(\xi\right) \ln\left|\left(L-x\right)-\left(L-\xi\right)\right|\left(-dx\right)\left(-d\xi\right) \tag{44}$$

Therefore $$\frac{DR_W}{q} \equiv \frac{DF_W}{q} \tag{45}$$

Consequently we obtain the result that *the drags of a body of revolution in forward and reverse flow are equal.*

This result is commonly called the reverse flow theorem. This result was first noted by von Karman [21] when he noted the invariance of drag with forward and reverse directions of flight for a non-lifting wing at supersonic speeds. The formal statements of the *reverse flow theorem* generally include [17]:

- *The drag of a linear source distribution is equal in forward and reverse flow.*
- *The drag of a given volume or thickness distribution is the same in forward reverse flows*
- *The drag of a given distribution of lift is unchanged by a reversal of the flow direction.* In this case however the physical geometry such as camber, twist and angle of attack will by necessity be different for the forward and reverse flows.
- *The drag of a general distribution of thickness, lift and side force elements in supersonic flow is the same in forward and reverse flight.*

VIII. Body Wave Drag and Optimum Bodies

For most of the remainder of this report we will focus on geometries that have zero slopes at both ends the the area distributions. The slope of the area distributions will look similar to that shown in figure 23.

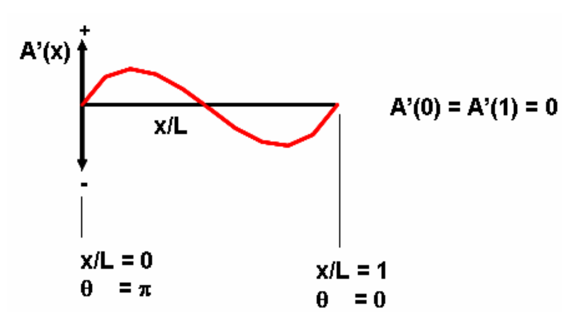

Figure 23. Typical Area Distribution Slopes

Since S'(0) = S'(1) = 0 we can represent the slope of the area distribution as a Fourier sin series in terms of the angle θ defined by equation 46.

$$\frac{x}{L} = \frac{1}{2}\left(1+\cos\theta\right) \tag{45}$$

$$A'\left(x\right) = \pi L \sum_{n=1}^{\infty} b_n \sin\left(n\theta\right) \tag{46}$$

Using equation 46 and carrying out the double integration in the wave drag equation (eqn 28) we obtain the result [22, 23]:

$$\frac{Dw}{q} = \frac{\pi^2 l^2}{4} \sum_{n=1}^{\infty} n b_n^2 \qquad 47$$

The wave drag is related to the sum of the squares of the Fourier series coefficients times the number n of the coefficient.

Consequently it is seen that every term in the Fourier series contributes to positive drag. Furthermore since each term is scaled by increasing values of "n", the higher harmonic terms add increasing amounts of drag. This infers that low drag bodies will be smooth without "wiggles"

The equation for the general area distribution can be obtained by integration [23] of equation 46 as:

$$S(\theta) = \frac{\pi l^2}{4} \left\{ b_1 \left(\pi - \theta + \frac{\sin 2\theta}{2} \right) + \sum_{n=2}^{\infty} b_n \left[\frac{\sin(n+1)\theta}{n+1} - \frac{\sin(n-1)\theta}{n-1} \right] \right\} \qquad 48$$

The base area of a body is given by the value of S(θ) at θ = 0.

Thus $$S(\theta = 0) = S(L) = \frac{\pi L^2}{4} b_1 \qquad 49$$

Only the first terms in the series defines the base area. Integration of equation 49 gives the body volume as

$$Vol. = \frac{\pi^2 l^3}{8} (b_1 - 0.5 b_2) \qquad 50$$

The remaining terms in the body series equation are simply shaping terms that add drag and do not contribute to either the base area or the body volume.

It is obvious from these results that the minimum drag volume for a specified base area is defined as

$$S(\theta) = \frac{S(l)}{\pi} \left(\pi - \theta + \frac{1}{2} \sin 2\theta \right) \qquad 51$$

This defines the Karman ogive, which we previously derived from the wave drag and induced drag similarity condition in equation 37.

The Karman ogive wave drag is given as: $$\frac{Dw}{q} = \frac{4[S(L)]^2}{\pi L^2} = \frac{16\, Vol^2}{\pi L^4} \qquad 52$$

For a pointed body with zero base area, the body volume is defined only by the second term in the series.

$$Vol. = -\frac{\pi^2 l^3}{16} b_2 \qquad 53$$

The area distribution for this case becomes: $$S(\theta) = \frac{\pi l^2}{4} b_2 \left[\frac{\sin 3\theta}{3} - \frac{\sin \theta}{1} \right] \qquad 54$$

However $$\sin 3\theta - 3\sin\theta \equiv 4\sin^3\theta \qquad 55$$

Therefore the *optimum area distribution for minimum wave drag for a specified volume which is called the Sears-Haack body* is given by

$$S_{SH}(\theta) = \frac{16\ Vol \sin^3\theta}{3\pi L} \qquad 56$$

The subscript "SH" stands for the Sears-Haack body
This can be expressed in terms of the non dimensional axial length, ψ = x/L as

$$S_{SH}(\psi) = \frac{16Vol}{3\pi L}\left[1-(1-2\psi)^2\right]^{3/2} = \frac{128Vol}{3\pi L}\left[\psi(1-\psi)\right]^{3/2} \qquad 57$$

The radius distribution is given as $$R_{SH}(\psi) = \sqrt{\frac{128\ Vol}{3\pi^2 L}}\left[\psi(1-\psi)\right]^{0.75} \qquad 58$$

The wave drag is equal to $$\frac{D}{q} = \frac{128Vol^2}{\pi L^4} \qquad 59$$

Notice that the results of equations 52 and 59 indicate, as mentioned in the introduction and shown in figure 3, that the wave drag varies with volume squared divided by the length to the fourth power.

IX. Arbitrary Body Wave Drag Calculation

Initial attempts for calculation of the wave for bodies of revolution followed the approach outlined below

1. Given a body area distribution, calculate A'(x) at M defined body stations

2. Represent A'(x) Distribution as A Finite Fourier Series of K Terms

$$A'(x) = \pi L \sum_{n=1}^{K} b_n \sin(n\theta) \qquad 60$$

3. For the calculated S'(x) values, "fit" A Fourier series through the M defining points

$$b_n = \frac{2}{\pi}\sum_{n=1}^{M} A'(x)\sin(n\theta)\Delta\theta \qquad 61$$

4. Calculate Drag From the Fourier Series Coefficients

$$\frac{Dw}{q} = \frac{\pi}{4}\sum_{n=1}^{K} nb_n^2 \qquad 62$$

Although this approach is seemly very straight forward it did not prove to be mathematically acceptable for a number of reasons including:

- Calculated drag values were highly sensitive to number of curve fit points, M and to the number of the Terms in the Series, K

- Inconsistent Drag Predictions with changes in the number of defining points and / the order of the selected Fourier series
- no practical strategy for determining convergence of the drag prediction

Lord and Eminton [24] resolved this mathematical difficulty by developing a method utilizing the calculus of variations to determine the least drag body shape through specified body area control points. This method which is currently used in most of the present day wave drag programs is described below.

Assume the analysis body area slope distribution can be represented by the following Fourier series.

$$A'(x) = \sum_{n=1}^{M} b_n Sin(n\theta)) \tag{63}$$

b_n are the "To Be Determined" Unknown Coefficients

The area distribution can then be expressed as: $A(x) = A(0) + \frac{1}{4} b_1 \theta + \frac{1}{4} \sum_{n=1}^{M} \frac{1}{n} (b_{n+1} - b_{n-1}) Sin(n\theta)$ 64

The analysis body is defined by a set of the Body area values, $A(x_i)$, at an arbitrary number, k, of specified stations, x_i. Each specified area can be expressed in terms of the "To be determined coefficients" as:

$$A(x_i) = A(0) + \frac{1}{4} b_1 \theta_i + \frac{1}{4} \sum_{n=1}^{N_x} \frac{1}{n} (b_{n+1} - b_{n-1}) Sin(n\theta_i) \tag{65}$$

The drag can be calculated in terms of the "To Be Determined Coefficients" using equation 62.

We will determine the coefficients by the use of Lagrange Multipliers.

Define the area constraint equations as:

$$\Phi_i = A(x_i) - A(0) - \frac{1}{4} b_1 \theta - \frac{1}{4} \sum_{n=1}^{N_x} \frac{1}{n} (b_{n+1} - b_{n-1}) \sin n\theta = 0 \tag{66}$$

Using Lagrange multipliers λ_i, define the objective function F as:

$$F = \frac{D}{q} - \sum_{i=1}^{k} \lambda_i \Phi_i \tag{67}$$

Then the conditions:

$$\frac{\partial F}{\partial b_n} = 0 \quad \text{For} \quad n = 1 \Rightarrow N_x \qquad \text{and} \qquad \frac{\partial F}{\partial \lambda_i} = 0 \qquad \text{for} \qquad i = 1 \Rightarrow k$$

Provides Nx+ k equations for the determination of the Nx+ k Unknowns

The solution of this system of equations includes the following steps [24]:

1. $$U(x) = \frac{1}{\pi} \left[Cos^{-1}(1-2x) - (2-4x)(x-x^2)^{\frac{1}{2}} \right] \tag{68}$$

2. $$C_j = S(x_j) - S(0) - \left[S(1) - S(0) \right] U(x_j) \tag{69}$$

3. $$P(x_i, x_j) = \frac{1}{2} (x_i - x_j)^2 \ln \left[\frac{x_i + x_j - 2x_i x_j - 2\sqrt{x_i x_j (1-x_i)(1-x_j)}}{x_i + x_j - 2x_i x_j + 2\sqrt{x_i x_j (1-x_i)(1-x_j)}} \right] + 2(x_i + x_j - 2x_i x_j) \sqrt{x_i x_j (1-x_i)(1-x_j)}$$

Solve for λi from the system of equations: $$\sum_{i=1}^{k} \lambda_i P\left(x_i, x_j\right) = C_j \tag{71}$$

The optimum area distribution is: $$A(x) = A(0) + \left[A(1) - A(0)\right]U(x) + \sum_{i=1}^{k} \lambda_i P\left(x_i, x_j\right) \tag{72}$$

The minimum wave drag is: $$\frac{D_W}{q} = \frac{4}{\pi}\left[A(1) - A(0)\right]^2 + \sum_{i=1}^{k}\sum_{j=1}^{k}\left[\lambda_i \lambda_j P\left(x_i, x_j\right)\right] \tag{73}$$

This is the drag calculation procedure that is embedded in the system of programs used to obtain the drag predictions described in this report. Figure 24 shows the results of wave drag predictions of a body of revolution that has an ogive nose with a cylindrical mid-section and an ogive aft-body. As shown in the figure, because of the cylindrical mid- section, a rather large number of defining points is required to force the analysis shape to represent the actual geometry.

The analysis with 4 defining points results in a smooth very low drag body that is significantly different than the ogive-cylinder geometry. As the number of defining points is increased it is seen that the analysis geometry is forced to match ultimately match the ogive cylinder geometry and the drag converges smoothly to the final drag prediction.

This example demonstrates the general convergence characteristics of the wave drag calculation procedure embedded in the Boeing developed wave drag program that was ultimately released as the Harris wave drag program [25].

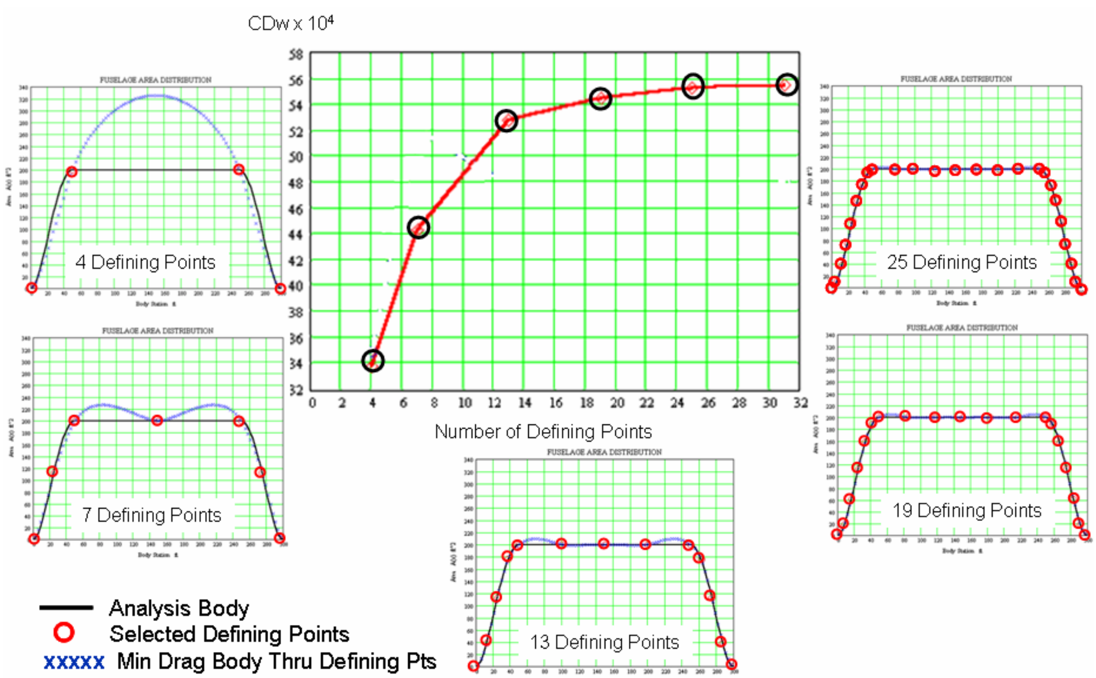

Figure 24: Convergence of the Ogive-Cylinder With Increasing Number of Body Area Defining Points.

Figure 25 shows the results of a study to determine the optimum body shapes as a function of the location of the constraining area location. The bodies in this study were defined by three points that included zero area at the body nose, the body length with zero area at the aft-end, and a specified mid-body area specified to occur at different locations along the body. The minimum body shapes and the corresponding wave drag predictions are shown in the figure. The body wave drag is seen to increase rather rapidly as the location of the mid-body control point station moves either forward or aft of the mid body station. The forward and aft symmetry of the results demonstrate the previously described reverse flow theorem. The three point body with the maximum area at 50% of the body length is actually the Sears Haack minimum drag body. The other 3 point bodies are commonly called Haack-Adams bodies.

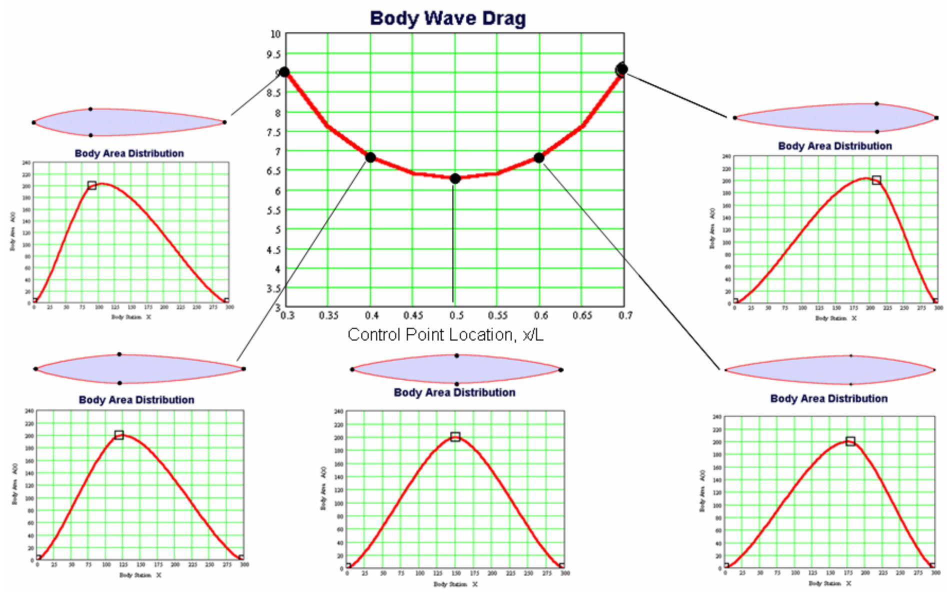

Figure 25. Effect of the Location Maximum Area on Body Shape and Wave Drag

X. NACA Area Rule

The concept of the area rule that will be discussed in this section is shown in figure 26 as an example of arriving at a similar aerodynamic concept or discovery by various individuals who followed different paths to discovery while using predominately different aerodynamic tools.

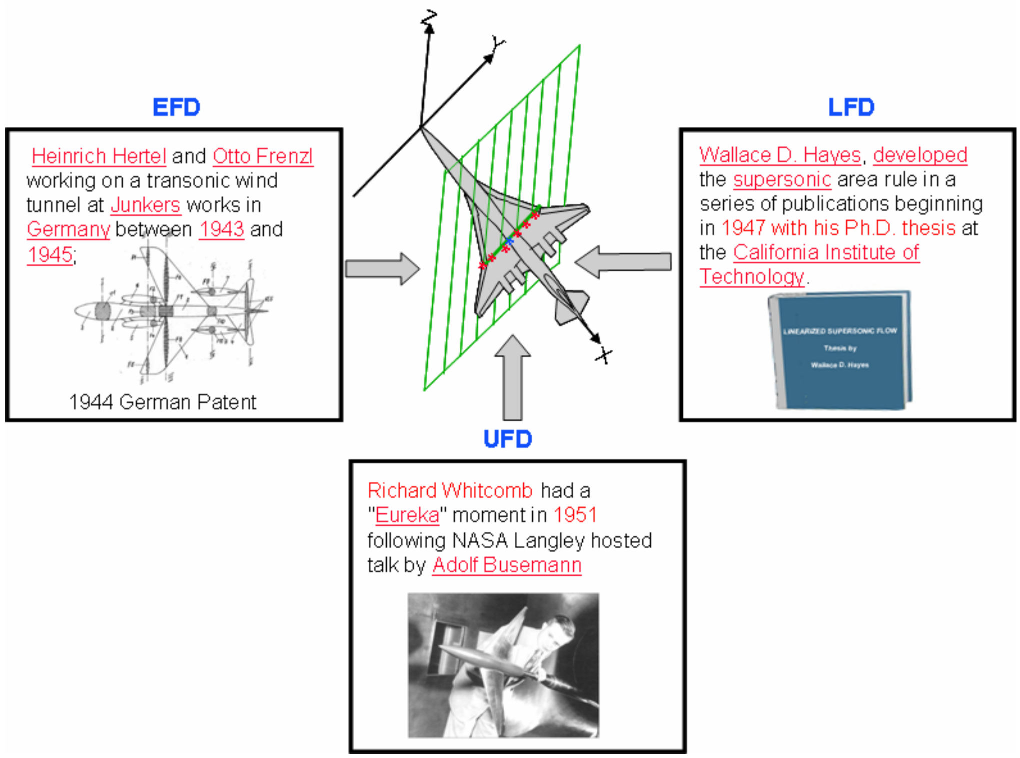

Figure 26. Various Paths Leading to the Development of the NACA Area Rule

The area rule was first discovered by a team including Heinrich Hertel and Otto Frenzl working in a transonic wind tunnel, (EFD) at Junkers in Germany between 1943 and 1945; it is defined in a patent filed in 1944. The design concept was applied to a variety of German wartime aircraft,

Richard Whitcomb [26] was testing wing-body combinations in 1952, in the new NACA eight–foot high speed slotted-throat wind tunnel that could operate at Mach numbers up to Mach 0.95. He was surprised by the increase in drag due to shock wave formation. The schlieren pictures had shown that shock waves were greater than anticipated. Undoubtedly, it was the losses from these unexpected shock patterns that were causing the sharp increase in drag at transonic speeds. The reason why the shocks occurred, sometimes as low as Mach 0.70, remained something of a mystery.

Whitcomb attended a talk by Adolf Busemann, a world-famous German aerodynamicist at NACA Langley. Busemann talked about the difference in the behavior of airflow at speeds approaching supersonic speeds, where it no longer behaved as an incompressible fluid. He explained that the airflow streamlines no longer contracted with the air flowing smoothly around an aircraft. At high speeds it simply didn't have time to "get out of the way“. Instead the flow streamlines behaved as constant area pipes of flow bending around a configuration.

Several days later Whitcomb had a "Eureka" moment, (UFD). The reason for the high drag was that the "pipes" of air were interfering with each other in three dimensions. You could not simply consider the air flowing over a 2D cross-section of the aircraft as you could in the past; now you also had to consider the air to the "sides" of the aircraft which would also interact with these streampipes. Whitcomb realized the wave drag was caused by the entire cross-sectional area of the wing body configuration. The details of the shape itself were not as critical in the creation of drag, but the rate of change in the area had the most significant effect. This also meant the extra cross sectional area of the wings and tail had to be accounted for in the overall shaping of the body for low drag. Consequently he concluded that the flow at near sonic speeds depended on the total cross-sectional area of the configuration. This became known as the “NACA area rule”.

The equation for the equivalent body area distribution, $S_{Eq}(x)$ is shown in equation

$$S_{Eq}\left(x\right) = S_W\left(x\right) + A_B\left(x\right) \tag{74}$$

Where $S_W(x)$ is the wing cross sectional area and $A_B(x)$ is the body cross-sectional area.

$$\frac{D_W}{q} = -\frac{1}{2\pi}\int_0^L\int_0^x S''_{Eq}\left(x\right)S''_{Eq}\left(\xi\right)\ln\left|x-\xi\right|dx\,d\xi \tag{75}$$

Once experimental verifications were made of the NACA area rule, its theoretical basis based on the earlier work by Hayes, was recognized, (TFD). Some of the first glimpses into the physics of the area rule were provided by Hayes in his 1946 thesis report [27]. The linearized equations he developed for predicting supersonic wave drag showed that as the Mach number approached unity the wave drag calculation simplified to that of a body of revolution.

A simple way to explain the area rule is shown in figure 27. Close to Mach 1, all of the disturbances from each of the sources that define the aircraft components radiate disturbances radially out to the control volume surface which is considered to be located a great distance from the centerline of the body. The distances between the sources on the wing and those defining the body is very small compared to the distance from the body to the control volume. Consequently the wing sources can be “slid” to the body axes along the normal cutting planes without altering the momentum loss through the sides of the control volume.

Sliding the wing sources in the normal cutting planes to the axes of the body results in an effective body of revolution with a cross-sectional area equal to that of the total configuration. Consequently the streamwise momentum variations at any station along the control volume are equal around the circumference of the control volume.

As shown schematically in figure 27, close to Mach 1, the flow field around a wing-body configuration ultimately collapses into a circumferently uniform flow field so that at any station the streamwise momentum loss through the control volume is uniform around the circumference of the control volume. An example Wing plus body cross sectional area distribution is also shown in the figure.

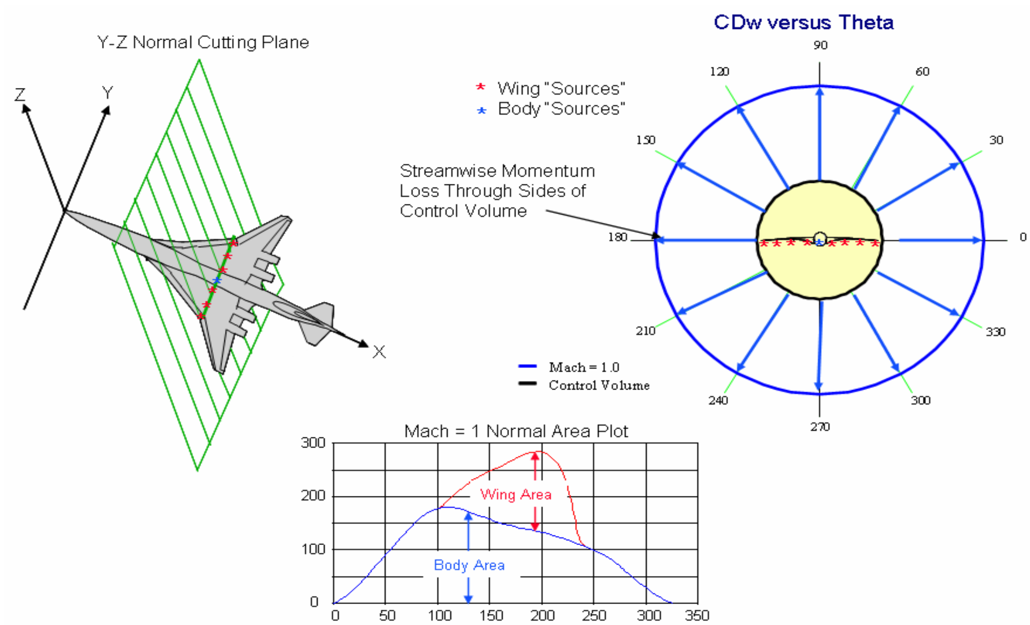

Figure 27. NACA Area Rule

Whitcomb's curiosity-driven, experimental approach was especially significant in discovering the area rule, because there was no available theory to explain the unusual drag encountered at transonic speeds. Researchers had to come up with a creative way of reaching beyond the known. Conducting hands-on experiments with an aircraft model in a wind tunnel also helped Whitcomb "see" the airflow phenomena in a way that the existing mathematical formulas could not have provided.

The breakthrough still required the wisdom, understanding and insight of a creative mind; a mind able to "see" the problem and able to step back from accepted rules of design to contemplate a solution based on an entirely new approach. The process by which Whitcomb was able to do that offers insight itself as to how break through scientific or technological innovation often occur.

It should be noted that until NACA Langley developed a "slotted throat" modification for the 8-foot wind tunnel in 1950 that transonic flows could be thoroughly explored. The slotted-throat modification prevented the flow choking that had limited the speeds in the test section of the tunnel, and allowed the air to go through the speed of sound. For the first time, researchers had a tool to investigate precisely what airflow did in that speed range and what might be causing the puzzling drag they had observed. The wind tunnel as previously mentioned was a critical element in Whitcomb's discovery of the area rule. This illustrates fact that breakthrough technology advances most often require breakthrough technology advancements on many fronts.

Wind tunnel results obtained by Whitcomb that demonstrate the NACA area rule are shown in figure 28. The wave drag increments shown in the figure are equal to the zero lift drag of a configuration minus its sub-critical viscous drag. Results are shown for an isolated body, a wing and body configuration, and an equivalent body with a cross-sectional area equal to that of the wing and body. It is seen that the wave drag increments of the wing and body are essentially equal to those the equivalent body. The equivalent body wave drag is however much greater that the isolated body.

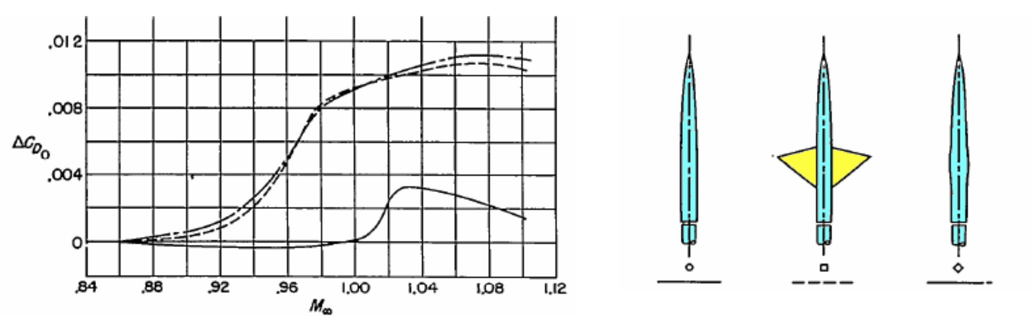

Figure 28: Wind Tunnel Data Demonstrating the NACA Area Rule

Whitcomb also reasoned that since the wave drag of a aircraft configuration is equal to that of the equivalent cross-sectional area body of revolution [26], that *the near sonic wave drag could be reduced by shaping the body so that the overall equivalent body area distribution would be smooth and close to that of an ideal Sears-Haack body.*

Figure 29 is an experimental demonstration of this concept. In this example, the optimized fuselage body is shaped so that the combined wing plus shaped body area distribution matches that of the reference isolated body. The measured wave drag of the isolated body, the wing plus original body and the wing plus reshaped body are shown in the figure. It is seen that the wave drag of the wing plus reshaped body is nearly equally to that of the isolated body up to about Mach 1.04.

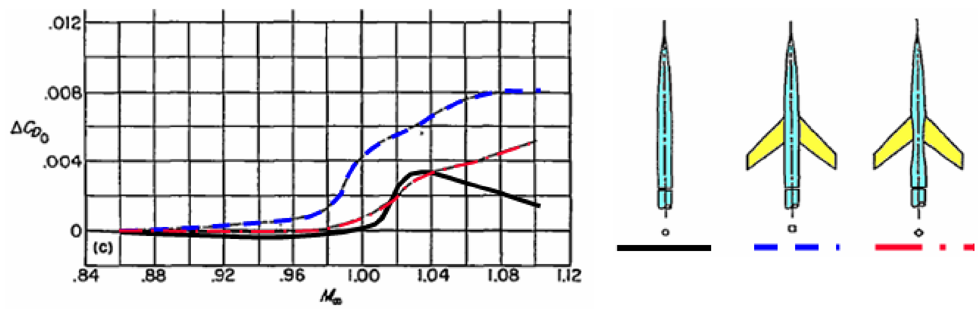

Figure 29. Example of Wind Tunnel Validation NACA Area Rule Application To Reduce Wave Drag

Whitcomb's research was a major breakthrough in supersonic aerodynamics and had an immediate effect on the design of the development of the F-102 fighter. Initial designs of the F-102 encountered near sonic drag and fell far short of meeting the design performance objectives. Convair engineers redesigned the aircraft's fuselage, taking the area rule concept into account, to create the "waisted" or "coke-bottle" fuselage. This modification, plus a new engine, allowed the aircraft to easily exceed Mach 1 and achieve a maximum speed over Mach 1.5.

Figure 30 shows the area distributions of the original F-102A and the modified F-102A after area ruling. Rocket launched flight models of both configurations, that were used to help in the validation process, are also shown. The area rule had imncreased the speed of the F-102 design by an estimated twenty-five percent.

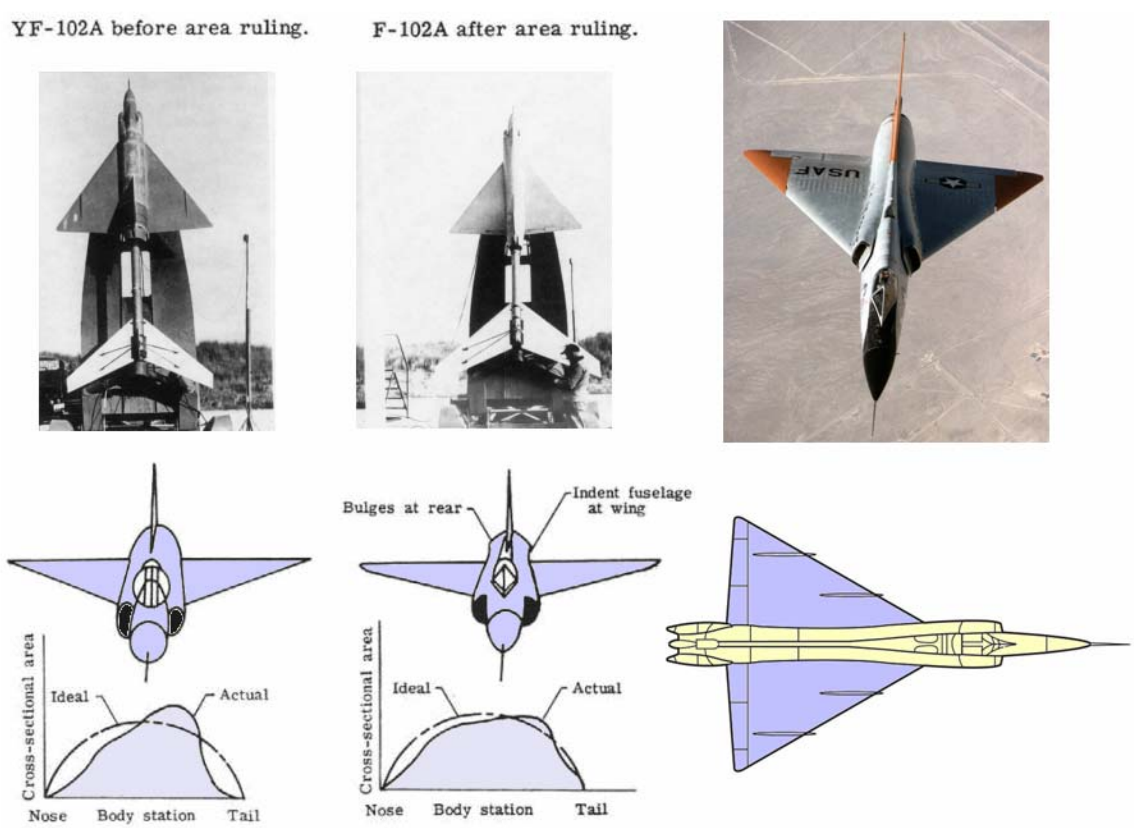

Figure 30. Area Rule Development of the F-102A

XI. Supersonic Area Rule

Heaslet and Lomax [28, 29, 30], and R.T. Jones [31] extended the concept of the area rule equivalent body to supersonic speeds. The cutting planes however become oblique planes tangent to the freestream Mach cones as shown in Figure 31.

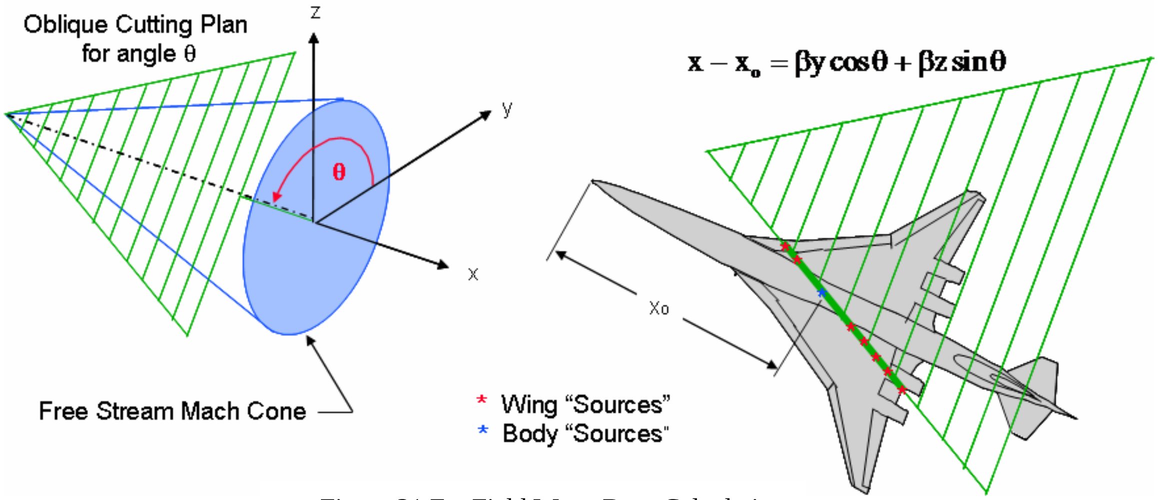

Figure 31 Far Field Wave Drag Calculation

The cutting planes are identified by the tangency angle θ as shown in the figure. The $\theta = 90^O$ cutting plane is tangent to the top of the Mach forecone. This defines the moment loss through the thin streamwise strip on top of the control volume. The $\theta = 0^O$ cutting plane is tangent to the side of the Mach cone and defines the loss of momentum through the thin strip on the side of the control volume. The cutting planes identified by values of θ between 0^O and 90^O define the momentum loss in the streamwise strips around the cylinder between the top and the side. For a symmetric configuration, the momentum loss is symmetric in all quadrants. The total wave drag of the configuration is equal to the integrated sum of the momentum losses around the surface of the control volume as shown in equation 76.

$$\frac{D}{q} = -\frac{1}{4\pi^2}\int_0^{2\pi} d\theta \int_0^{l(\theta)}\int_0^{l(\theta)} S''(x,\theta)S''(\xi,\theta)\ln\left|x-\xi\right| dx d\theta \qquad 76$$

The equation for the cutting plane is $x - \beta y\cos\theta - \beta z\sin\theta = x_0$ 77

Where $\beta = \sqrt{M^2 - 1}$

This is the far field wave drag equation for a symmetric non-lifting configuration. The volume wave drag is the average of the of the wave drags of the theta dependent equivalent bodies.

Supersonic wave drag can therefore be calculated as the average of a series of equivalent bodies cut by oblique planes tangent to a free stream Mach cone for $\theta = 0^O$ *to* 360^O

Because of the similarity of this equation with the near sonic wing / body equation 75, it follows that the lower bound zero lift wave drag for any symmetric configuration occurs if each of the theta dependent equivalent body is a Sears-Haack body for the same length and maximum area. This lower bound is exact for a yawed elliptic wing with a circular arc wing section and constant spanwise curvature. However, it is generally impossible to define such a volume distribution for an arbitrary wing / body configuration. Thus we need a more realistic lower bound for wave drag. This is discussed in greater detail in reference 15.

Figure 32 shows results of wave drag calculations for a supersonic wing plus body configuration at Mach 2.4. The wave drag distribution around the configuration is shown along with the Mach 1 drag distribution. The maximum drag occurs for $\theta = \pm 90$ degrees which is above and below the configuration. The drag at these stations is equal to that at Mach 1. Some of the combined area distribution plots are shown for different angular stations around the configuration. At the higher Mach number, the angular distribution rapidly decreases to a minimum off to the side of the configuration. This is associated with the peak of the wing area distribution being reduced and the wing volume spread over a longer length.

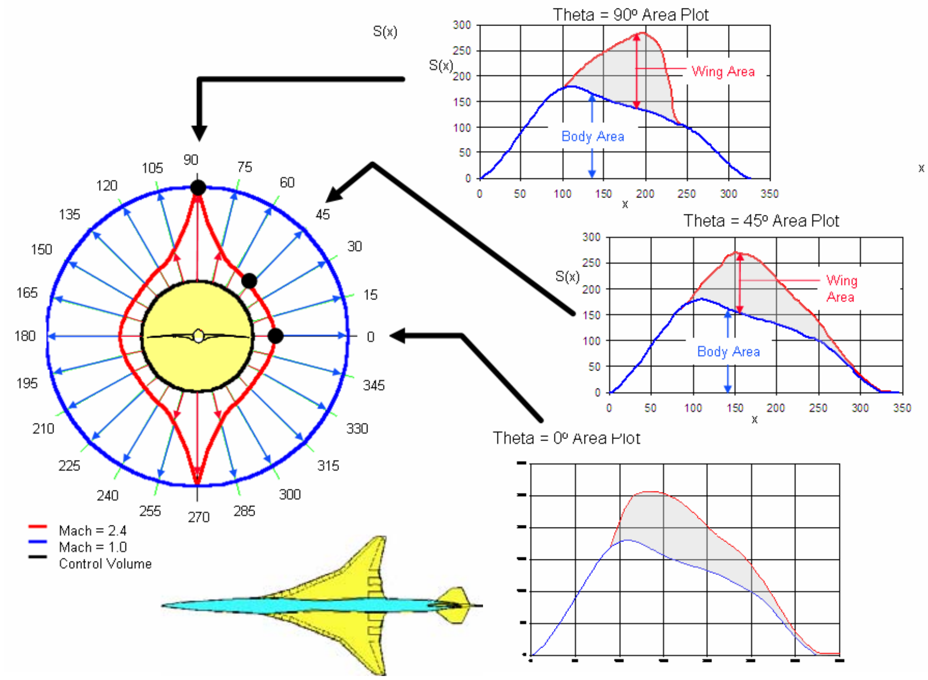

Figure 32. Typical HSCT Wave Drag Distribution About the Control Volume

Figure 33 shows the effect of free stream Mach number on the angular distribution of drag about the configuration and also on the total wave drag. The individual drag distribution figures are identified both by the free stream Mach number and by the Mach number normal to the inboard wing leading edge. The angular drag distribution as well as the total wave drag rapidly decrease with Mach number until a free stream Mach number of about 2.4 corresponding to an inboard normal Mach number of approximately 0.8. Above a free stream Mach number of 2.4 the wave drag begins to increase to the side of the configuration. This is associated with the inboard wing leading edge approaching a sonic condition with the normal Mach number becoming close to 1.

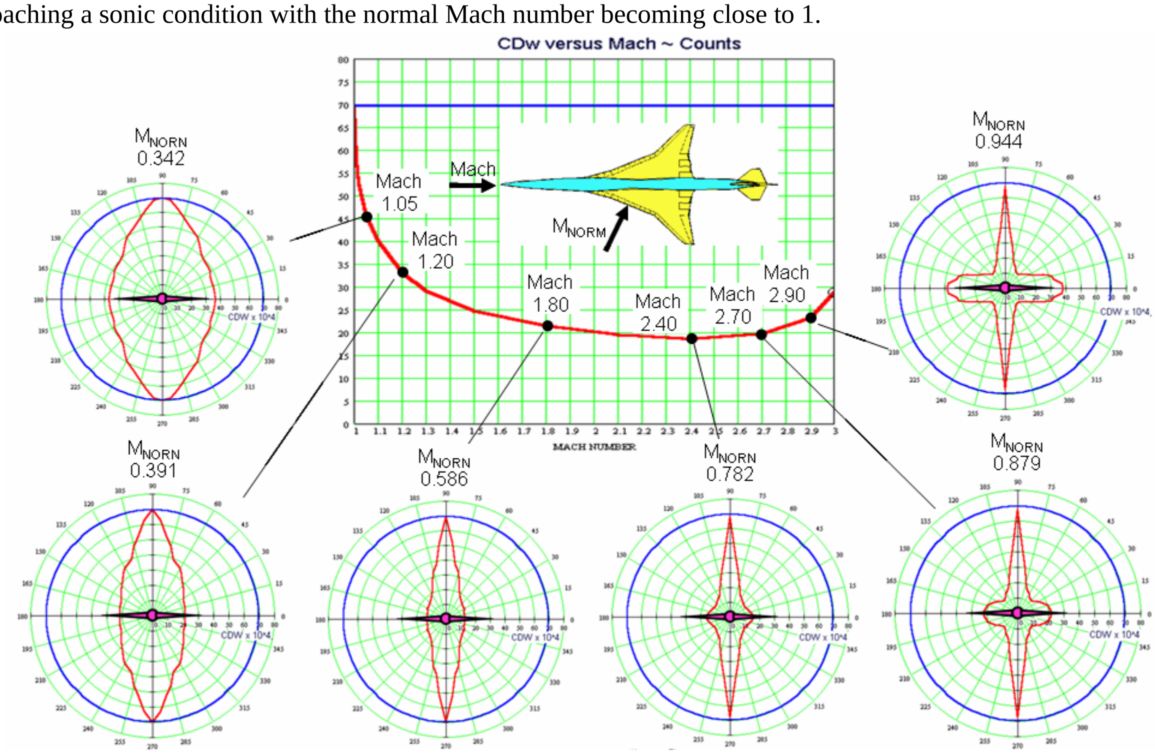

Figure 33. Effect of Mach Number on Wave Drag and Wave Drag Distribution

Numerically, the angular variations in wave drag with free stream Mach number are associated with two effects that include both the shape and the length of the corresponding wing equivalent area distributions. As shown in figures 34, 35 and 36, these two effects are very dependent on the free stream Mach number.

The figures show the effect of just the increase in the equivalent body length on the angular drag distributions while maintaining the same shape characteristics. The objective is to clearly illustrate the relative effects of the increased length of the wing equivalent bodies and the effects of the shape change of the equivalent bodies with Mach number as the equivalent bodies lengths are changed

As previously discussed, the drag of a body of revolution varies with the volume squared divided by the streamwise length raised to the 4th power. Since all of the angular equivalent bodies have equal volume, the effect of the increased length on drag can be calculated as.

$$CDw(\theta) = CDw(90^O)\left[\frac{X_S(90^o)}{X_S(\theta)}\right]^4 \qquad 78$$

Where CDw(90^O) is the wave drag for $\theta = 90^O$

$X_S(90^O)$ is the equilalent body length for $\theta = 90^O$

$X_S(\theta)$ is the equivalent length for the specified angle θ.

Figure 34 shows the angular distribution for a free stream Mach number of 1.3. The nose of the equivalent body is set by the cutting planes touching the wing apex. The end of the equivalent is determined by the cutting plane just touching the trailing edge of the wing tip. As shown in the figure, the rapid change in drag with "θ" is due almost entirely to the increased effective body length. There appears to be a very slight beneficial body shape change as θ is reduced from 90^O.

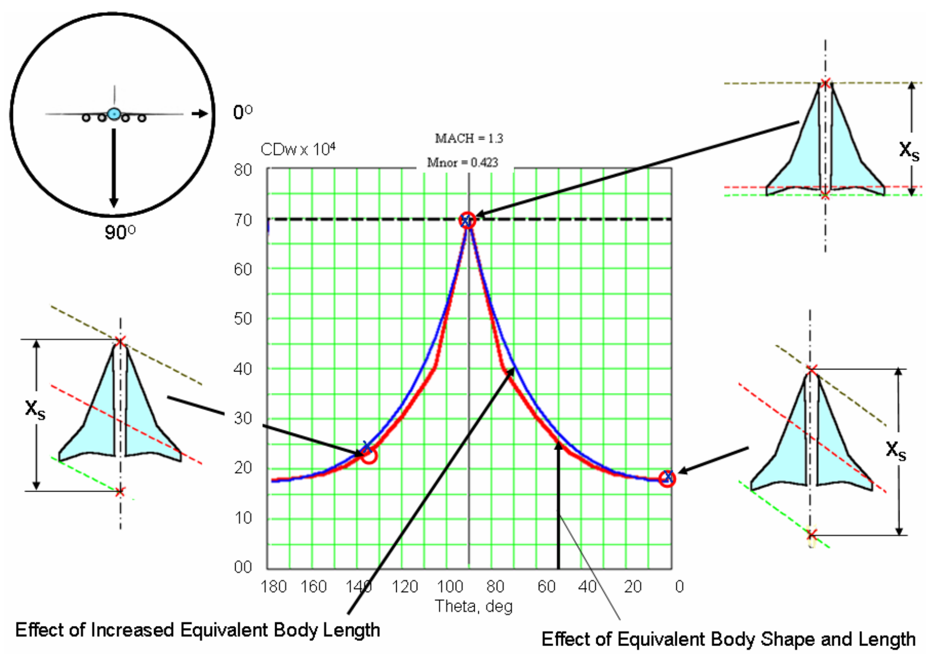

Figure 34. Equivalent Body Length and Wave Drag Distribution at Mach 1.3

The angular distribution of wave drag at Mach 2.4 is shown in Figure 35. As the cutting plane angle is reduced from 90 deg. to approximately 60 deg the dramatic equivalent wave drag decrease is due to the increased length of the equivalent body. For lower cutting plane angles adverse shape changes in the equivalent bodies tends to reduce the beneficial effects of the increased length of the wave drag.

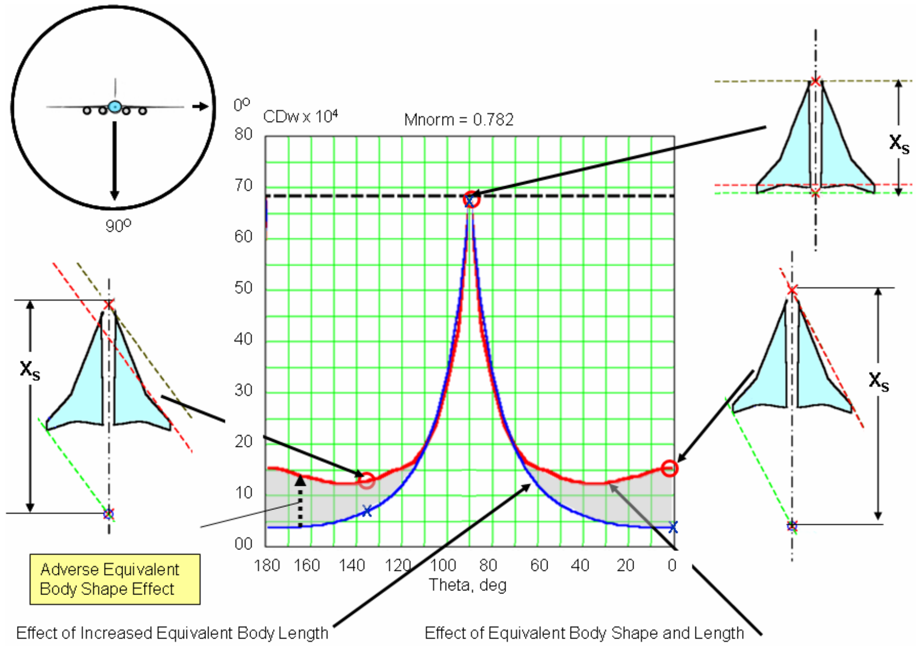

Figure 35. Equivalent Body Length and Wave Drag Distribution at Mach 2.4

The angular wave drag distribution for Mach 2.9 is shown in figure 36. It is seen that the angular increase in wave drag due to the adverse shape changes becomes very significant. The inboard wing normal Mach number is equal to 0.944. Consequently this means that the cutting plane angles for the lower angles are nearly parallel to the inboard wing leading edge. This means that the equivalent body will have a very sudden area increase which leads to the increased wave drag.

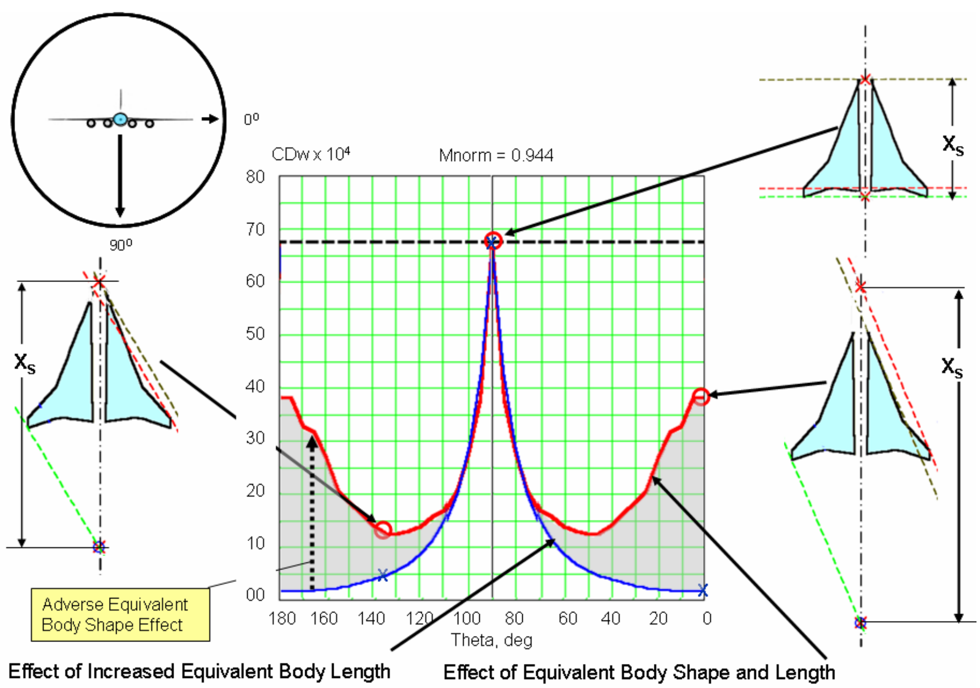

Figure 36. Equivalent Body Length and Wave Drag Distribution at Mach 2.9

Figure 37 shows test versus theory comparisons for two different symmetric supersonic wing plus body configurations. The highly swept wing configuration on the right has a subsonic leading for all of the analysis Mach numbers. The moderately swept wing for the configuration on the left has a subsonic leading edge for Mach numbers below Mach 2.0 and a supersonic leading at the higher mach numbers. The viscous drag was calculated as fully turbulent skin friction drag, the wave drag was calculated using the supersonic area rule theory. The theoretical predictions match the test data quite well.

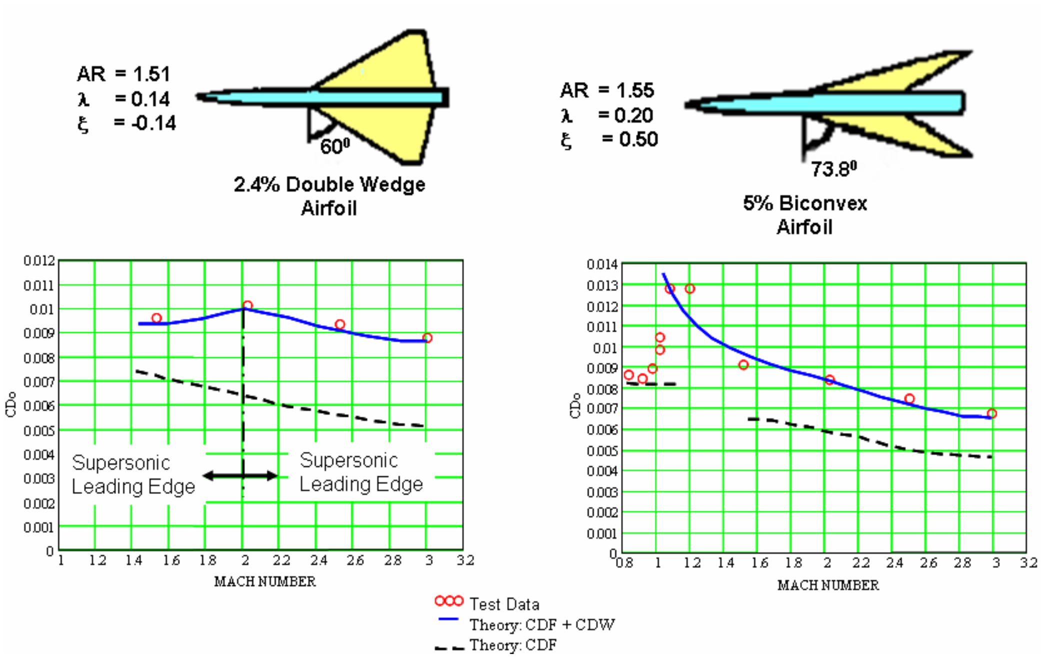

Figure 37. Zero Lift Drag Predictions Comparisons With Test Data

XIX. The Transfer Rule ➔ Supersonic Wing/Body Optimization

The supersonic area rule provides a technique to calculate the supersonic wave drag for a specified configuration. The Lord and Eminton method which is embedded in the supersonic area rule programs can be used to optimize an isolated body. The “transfer rule” which will be discussed below provides the concept and guidance to optimize a complete configuration.

Wing plus body wave drag for a specified Mach number can be calculated using the previously shown equation 76. In that equation, the area distribution consists of the wing area plus the body body in the various cutting planes. Since the body is slender symmetric body of revolution, the body area cuts do not depend on the angle of the cutting plane. Therefore we can express the total equivalent area to consist of the wing part that depends both on the streamwise station of the cutting plane and the angle of the cutting plane, plus the body part that depends only on the stream wise station.

$$S(x,\theta) = S_W(x,\theta) + A_B(x) \qquad 79$$

Substituting equation 79 into equation 76 the wave drag equation becomes.

$$\frac{D}{q} = -\frac{1}{4\pi^2}\int_0^{2\pi} d\theta \int_0^{l(\theta)}\int_0^{l(\theta)} \left[S''_W(x,\theta) + A''_B(x)\right]\left[S''_W(\xi,\theta) + A_B(\xi)\right]\ln|x-\xi|\,dx\,d\theta \qquad 80$$

The wing plus body drag, therefore consists of three components:

$$\frac{D}{q} = \frac{D_W}{q} + \frac{D_{WB}}{q} + \frac{D_B}{q} \qquad 81$$

Drag of the Isolated Wing:

$$\frac{D_W}{q} = I_1 = -\frac{1}{4\pi^2}\int_0^{2\pi} d\theta \int_0^{l(\theta)}\int_0^{l(\theta)} S_W''(x,\theta) S_W''(x,\xi)\ln|x-\xi|\,dxd\xi \tag{82}$$

Plus the Wing / Body Interference Drag:

$$\frac{D_{WB}}{q} = I_2 = -\frac{2}{4\pi^2}\int_0^{2\pi} d\theta \int_0^{l(\theta)}\int_0^{l(\theta)} S_W''(x,\theta) A_B''(x,\xi)\ln|x-\xi|\,dxd\xi \tag{83}$$

Plus the Drag of the Isolated Body:

$$\frac{D_B}{q} = I_3 = -\frac{1}{4\pi^2}\int_0^{2\pi} d\theta \int_0^{l(\theta)}\int_0^{l(\theta)} A_B''(x) A_B''(x,\xi)\ln|x-\xi|\,dxd\xi \tag{84}$$

Since the Body Does Not Vary With "θ", the Second Integral can be rewritten as:

$$I_2 \equiv -\frac{2}{2\pi}\int_0^{l_B} A_B''(\xi)d\xi \int_0^{l_M} \frac{1}{2\pi}[\int_0^{2\pi} S_W''(\theta,x)\,d\theta]\ln|x-\xi|\,dx \tag{85}$$

Define an "Average Wing Equivalent Body" as: $T(x) = \frac{1}{2\pi}\int_0^{2\pi} S_W(\theta,x)\,d\theta$ (86)

The wing equivalent body is obtained as the average of all the θ dependent areas for each cutting plane for every spanwise station. Figure 38 shows the average wing equivalent body area distribution along with equivalent body area distributions for two different cutting plane angles.

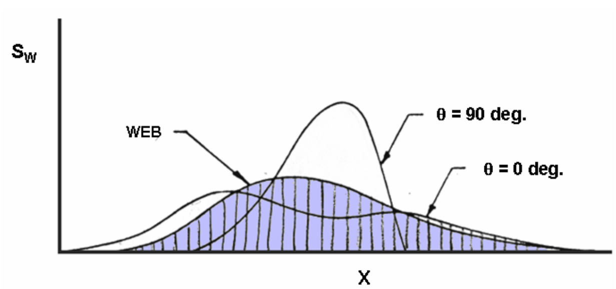

Figure 38 Equivalent Body and Average Equivalent Body Area Distributions Comparisons

Using the definition of the average wing equivalent body, we can write the second integral as

$$I_2 = -\frac{1}{2\pi}\int_0^{l_B}\int_0^{l} 2A_B''(\xi)T''(x)\ln(x-\xi)\,dxd\theta \tag{87}$$

however: $$I_4 \triangleq \left[T(x)+A_B(x)\right]^2 \equiv T^2(x) + \underbrace{2T(x)A_B(x)}_{\text{Integral "}I_2\text{"}} + \underbrace{A_B^2(x)}_{\text{Integral "}I_3\text{"}} \tag{88}$$

Or:

$$\underbrace{2T(x)A_B(x)}_{\text{Integral “}I_2\text{”}}+\underbrace{A_B^2(x)}_{\text{Integral “}I_3\text{”}}=\underbrace{\left[T(x)+A_B(x)\right]^2}_{\text{Integral “}I_4\text{”}}-\underbrace{T^2(x)}_{\text{Integral “}I_5\text{”}} \qquad 89$$

Replace the integrals I_2 and I_3 by the integrals I_4 and I_5:

The wing plus body drag, can be calculated as the sum of three components:

$$\frac{D}{q}=\frac{D_W}{q}-\frac{D_{WEB}}{q}+\frac{D_{WEB+B}}{q} \qquad 90$$

Drag of the Isolated Wing:

$$\frac{D_W}{q}=I_1=-\frac{1}{4\pi^2}\int_0^{2\pi}d\theta\int_0^{l(\theta)}\int_0^{l(\theta)}S_W''(x,\theta)S_W''(x,\xi)\ln|x-\xi|dxd\xi \qquad 91$$

Minus the drag of a fictitious body, the wing average equivalent body, WEB :

$$\frac{D_{WEB}}{q}=-\frac{1}{4\pi^2}\int_0^l\int_0^x T''(x)T''(x)\ln|x-\xi|dxd\xi \qquad 92$$

Plus the drag of another fictitious body defined as the fuselage area plus wing equivalent body area distributions:

$$\frac{D_{WEB+B}}{q}=I_5=-\frac{1}{2\pi}\int_0^{l_B}\int_0^{l}\left[T''(x)+A''(x)\right]\left[T''(\xi)+A''(\xi)\right]\ln(x-\xi)dxd\theta \qquad 93$$

The wing plus body drag can therefore be calculated as :

$$\frac{D}{q}=\frac{D_W}{q}-\frac{D_{WEB}}{q}+\frac{D_{WEB+B}}{q} \qquad 94$$

This approach is seldom if ever used calculation of wave drag. However it can be useful to study the effects of different body control points since only the wave drag in the third term would need to either be calculated or scaled. Similarly the transfer rule equation can be used to determine the effect of variations in wing area on the wave drag. In this case the first two terms would be scaled by the new wing area and the third term would be scaled by the new maximum control point area.

The real significance of this equation is the message that it provides.

The first two terms depend only on the wing geometry. Body area only appears with the wing average equivalent body in the third term. This term is available for optimization. Therefore for a given wing geometry, the minimum wing plus body drag can be determined and the corresponding optimum body can be defined by using the wave drag program. to optimize the shape of the combined body plus wing average equivalent body area distribution.

- *For a given wing definition, the wing plus body drag is minimized when the body is shaped so that the combined body plus the average wing equivalent body area distribution is an optimum shape.*

- *This defines the lowest wave drag wing + body combination for a specified wing definition.*

Paradox 3: *The supersonic area rule, which is based on the implicit assumption that the control volume surfaces are so far from the body axes that shape does not matter, can define the shape of the optimum body to minimize the wing-body wave drag.*

Throughout the above derivation, reference was made to only the wing plus body. However the concept can be applied to a complete wing body empennage configuration. However in this case the average equivalent body is the average area for all of the aircraft components except the body

The supersonic body optimization process includes the following steps shown in figure 39:

1. *Define required body area constraints*
2. *Calculate the average equivalent body area distribution for the configuration components.*
3. *Define the desired total area constraints*
4. *Calculate optimum area distribution that passes through the total area constraints using the wave drag program.*
5. *Subtract the average equivalent area from the optimum total area to obtain the optimized body area distribution*

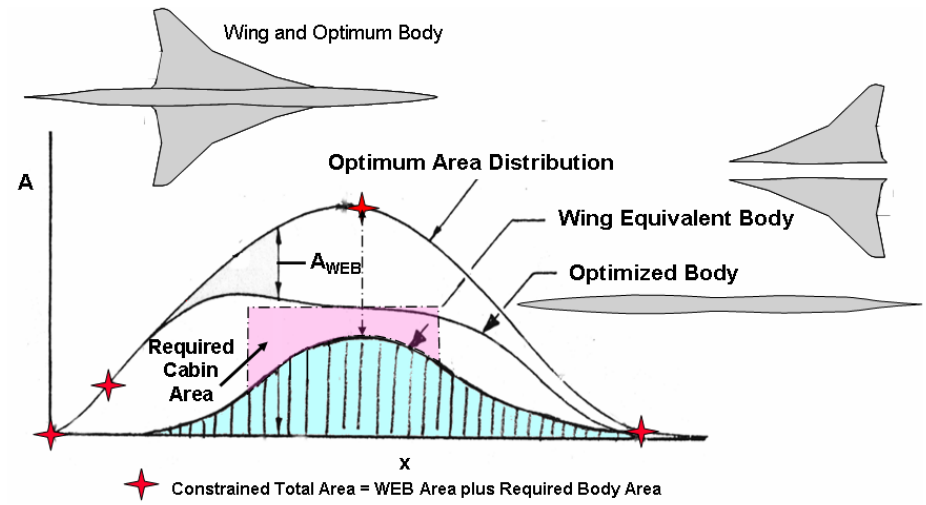

Figure 39 Supersonic Body Optimization Process

What is the minimum drag body shape for a given wing geometry? This was an interesting problem and solution provided by Armand Sigalla in 1962.

The "Minimum" is given by the smallest value of the drag of the fictitious body with an area distribution equal to the sum of the desired body area plus the area of the wing equivalent body:

$$\frac{D_{WEB+B}}{q} = -\frac{1}{2\pi}\int_0^{l_B}\int_0^{l}\left[T''(x)+A''(x)\right]\left[T''(\xi)+A''(\xi)\right]\ln(x-\xi)\,dx\,d\theta \qquad 95$$

We are given the Constraint that A"(z) > A''_{MIN}.

The Minimum Drag Occurs When $$T''(\xi)+A''(\xi)=0 \qquad 96$$

How do we achieve this**?**

As shown in figure 40, the condition for minimum drag as specified in equation 98 can be achieved with a constant combined area distribution. Consequently the drag for the configuration will have a drag less than the drag of the isolated wing drag.

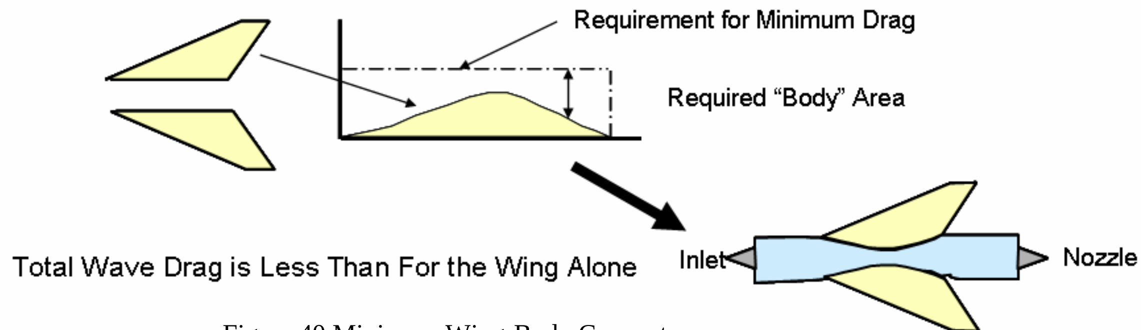

Figure 40 Minimum Wing-Body Concept

We have discussed the three transonic–supersonic ”Area rules” that include the “NACA Area Rule”, the “Supersonic Area Rule” and the “Transfer Rule”. The NACA Area Rule really consists of two sub “rules” that are distinguished by the different flow phenomena involved these can be called the “Sonic Area Rule” and the “Transonic Area Rule”. The sonic area rule is discussed in reference 31. The various features of these different “rules” are summarized in figure 41.

	NACA Area Rule		Supersonic Area Rule	Transfer Rule
	Near-Sonic M < 1	Transonic M > 1		
Basis	Experiment / Theory	Experiment / Theory	Theory	Theory
Primary Objective	1. Delay Drag Rise 2. Minimize Local Mach Number Distribution	Reduce Transonic Drag	Calculate Supersonic Drag	Optimize Wing / Body
Approach	Smooth Area Distribution	Smooth Area Distribution	Average Sum of Equivalent Body Drag Calculations	Apply Wing + Body Optimization "Rule"
Uses	Design Guidance	1. Design Guidance 2. Drag Estimation	1. Wave Drag Calculation 2. Body Optimization 3. Wing Optimization ----------------------------------- 4. Wave Drag Due to Lift Calculation 5. Induced Drag Calculation	1. For Given Optimize Wing + Body ----------------------------------- 2. Simple Wing Wave Drag Scaling 3. Vary Body Design Constraints [4. Alternate Wave Drag Calculation]

Figure 41. The four Area Rules

XX. Wave Drag Due to Lift

The wave drag discussions so far have focused on volume and thickness effects using source distributions to represent the aircraft geometry. For a supersonic configuration lift and side forces cannot be represented by only a distribution of sources. Sources essentially represent thickness or volume elements. Lift and side force elements, however, may be represented by doublets or by vortex elements.

Following Hayes [27], we can define a general singularity element representing thickness together with lift and side forces as:

$$h = f - \beta(l \sin\theta + s\cos\theta) \qquad 97$$

Where f = S’ is the volume singularity strength

And $\rho_\infty U_\infty{}^2 l(x,y,z) =$ Lift /unit volume

And $\rho_\infty U_\infty{}^2 s(x,y,z) =$ side force per unit volume

The total drag for the a distribution of generalized singularity elements is then

$$\frac{D}{q} = -\frac{1}{4\pi^2}\int_0^{2\pi} d\theta \int_0^{l(\theta)}\int_0^{l(\theta)} h'(x,\theta)h'(\xi,\theta)\ln|x-\xi|\,dx\,d\theta \qquad 98$$

The equation for wave drag due to lift can be obtained by setting the volume and side force elements equal to zero. This gives:

$$\frac{Dwl}{q} = -\frac{\beta^2}{4\pi^2}\int_0^{2\pi}\sin^2\theta\, d\theta \int_0^{l(\theta)}\int_0^{l(\theta)} l'(x,\theta)l'(\xi,\theta)\ln|x-\xi|\,dx\,d\theta \qquad 99$$

From this equation, we can draw some important conclusions.

- *The wave drag due to lift is proportional to β^2 and consequently vanishes as M ➔ 1.0*
- *The wave drag due to lift is an absolute minimum of the lift distribution for each θ cut is elliptic.* This condition is known as the Jones lower bound wave drag due to lift which can only be achieved with yawed elliptic wing with a uniform load distribution
- *The wave drag due to lift can be calculated using the volume wave drag equation with the local steamwise integrals of lift input as equivalent blunt base airfoils and accounting for the β^2 and $\sin^2\theta$ in equation 99*

Because of the previously discussed similarity between the wave drag due to volume equation and the induced drag equation, the induced drag of a aircraft configuration at subsonic or supersonic speeds can be calculated using a supersonic area rule wave drag program by inputing the integral of 1/2 the spanwise load distribution as an equivalent body of revolution of length equal to the wing span.

$$Ab(\psi)_{equivalent} \approx \int_{-\frac{b}{2}}^{\psi} \frac{1}{2} C\ell(\eta)\, d\eta \qquad \frac{-b}{2} \le \psi \le \frac{b}{2} \tag{100}$$

In order to validate the accuracy of wave drag due to lift and induced drag predictions using far field theory, comparisons were made of the far field predictions for a number of wing planforms with the corresponding predictions obtained from linear theory exact conical flow solutions. A conical flow as originally conceived by Busemann [33] is defined as a flow field in which all of the physical properties such as pressure, density, velocity, energy and entropy remain constant along every straight line starting from a given point called the apex of the flow which in most cases for highly swept wings is the wing apex. The use of the conical flow solutions presented in reference 33 can provide a great deal of insight into the effects of various geometries and their related aerodynamic characteristics.

Conical flow solutions obtained from reference 33 for flat lifting triangles having subsonic leading edges, or supersonic leading edges are shown in figure 42. The local lifting pressures can be obtained directly from the streamwise perturbation velocity as ΔCP(x,y) = 4u(x,y). The pressures can be integrated over any highly swept wing planform shape to obtain the total aerodynamic forces including lift and drag as long as the trailing and side edges are supersonic so that now part of the trailing wake can be felt on the wing.

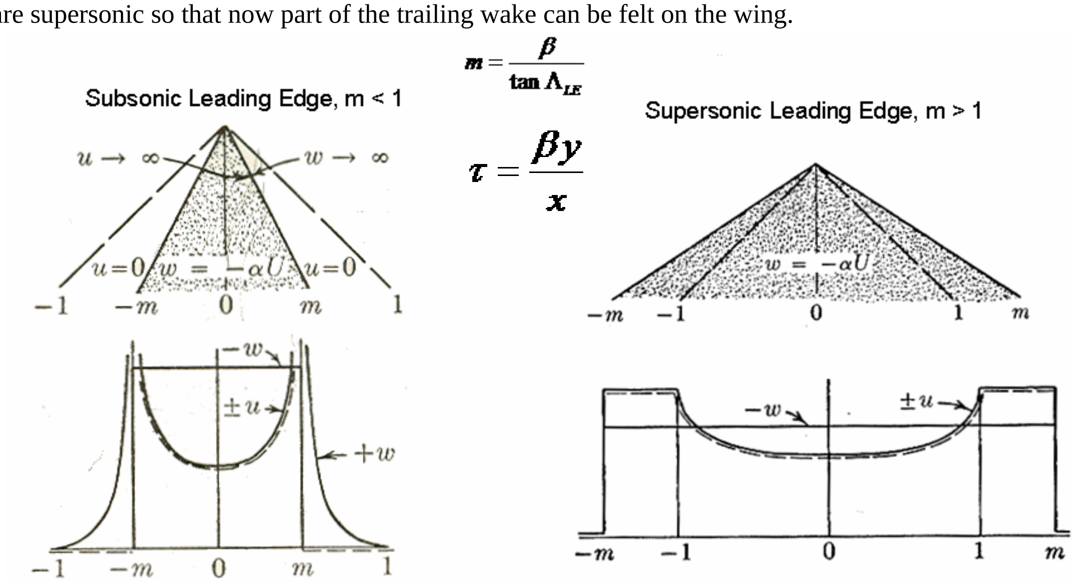

$$u = \text{R.P.}\, \frac{m^2 \alpha U}{\beta E(k)} \frac{1}{\sqrt{m^2 - \tau^2}}$$

$$w = \text{R.P.}\, \frac{\alpha U}{\beta E(k)} \left[\tau \sqrt{\frac{1-\tau^2}{\tau^2 - m^2}} - E(\vartheta, k) \right]$$

$$\vartheta = \sin^{-1}\sqrt{\frac{1-\tau^2}{1-m^2}}, \qquad k = \sqrt{1-m^2}$$

$$u = \pm\text{R.P.}\, \frac{\alpha U}{\beta\pi} \frac{m}{\sqrt{m^2-1}} \left(\cos^{-1}\frac{1-m\tau}{m-\tau} + \cos^{-1}\frac{1+m\tau}{m+\tau} \right)$$

$$w = \mp\text{R.P.}\, i \frac{\alpha U}{\beta\pi} \ln\frac{\tau+m}{\tau-m}, \qquad \beta = \sqrt{M_\infty^2 - 1}$$

Figure 42. Conical Flow Solutions for Flat Lifting Triangular

The conical flow equations shown in figure 42 have been used to calculate equivalent wave drag due to lift airfoils and the equivalent induced drag body of revolutions for a delta wing and also for an arrow wing. The results for the delta wing at a Mach number of 2.4 are shown in figure 43.

The lift equivalent airfoils are shown normalized relative to the local streamwise lengths. The integrated spanwise load distribution and the integrated spanwise load distribution are also shown. The spanwise load distributon for the delta wing is elliptic. Therefore the integrated spanwise load distribution is also seen to be the same as the area distribution of a Karman ogive nose.

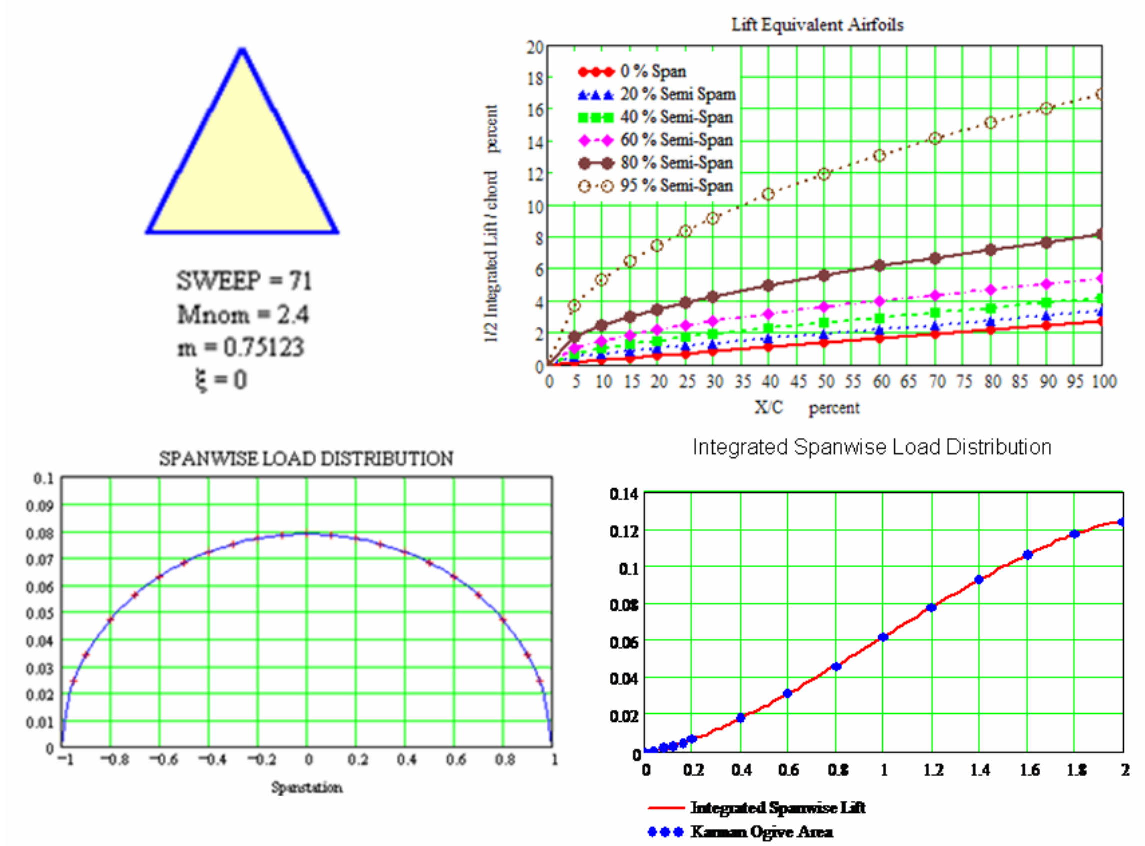

Figure 43 Delta Wing Lift Equivalent Airfoils and Spanwise Load Equivalent Body, Mach 2.4

Figure 44 shows comparisons of the drag due to lift calculations obtained with far field theory are compared with the comparable results obtained using conical flow theory. The results shown in the figure on the left are expressed in terms of the similarity parameters KE/β and m where

$$KE = \frac{CDL}{CL^2} \qquad \beta = \sqrt{M^2 - 1} \qquad \text{and} \qquad m = \frac{\beta}{\tan \Lambda_{LE}}$$

Values of m > 1 indicates that the wing leading edge is supersonic. Values of M<1 indicate the wing normal Mach number at the leading edge is subsonic.

The figure on the left in terms of the similarity parameters shows the drag due to lift for all delta wings and all supersonic Mach numbers. The conical flow solutions indicate two solutions below m = 1. These solutions include the drag due to lift with and without the leading edge suction force. The wave drag due to lift and the induced drags calculated by far field theory as shown in the figure to agree very well with the exact conical flow theory, The far field induced drag calculations are seen to be identical to the minimum induced drag obtain with an elliptic load distribution.

The figure on the right presents the same data in the form of the drag due to lift for a fixed leading edge sweep as a function of Mach number. In this form, the rapid increase of wave drag due to lift with Mach number is readily apparent. The RT Jones lower bound wave drag due to lift is also shown for reference. As previously mentioned, this level is not numerically achievable for most planforms including the delta wing.

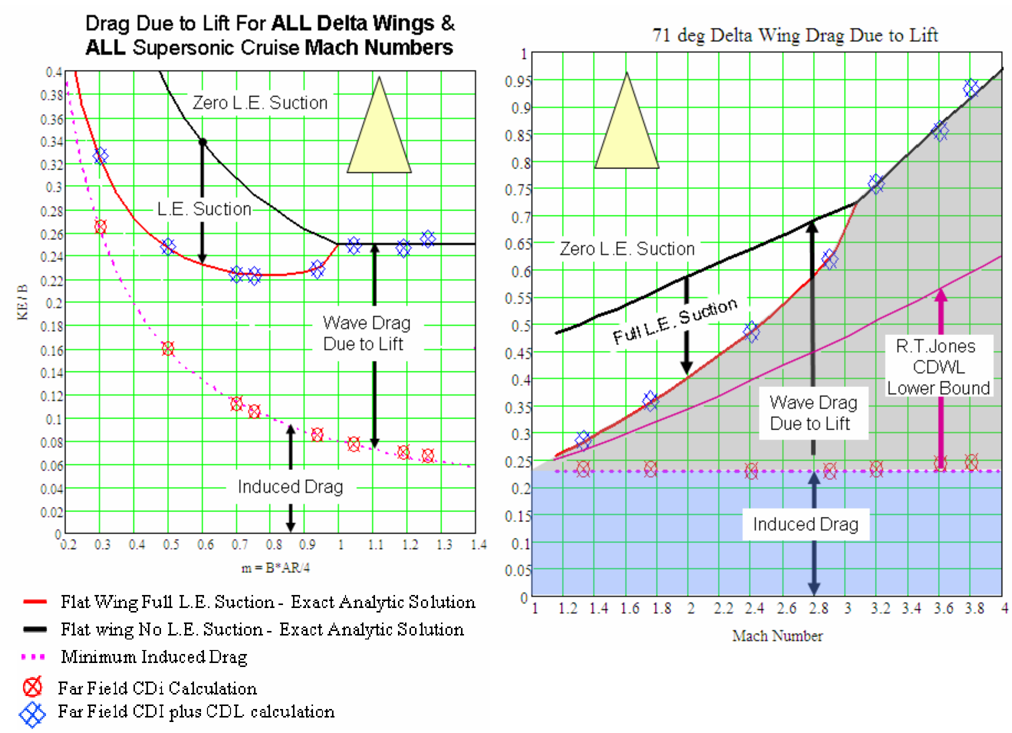

Figure 44. Validation of Far Field Drag Due to Lift Calculation – Delta Wing

Figure 45 shows the integrated lift equivalent airfoils of an arrow wing for computing the wave drag due to lift. The spanwise load distribution is also shown along with the integrated spanwise load equivalent body nose. The spanwise load distribution has a slight dip near the centerline of the wing. The integrated equivalent body is compared with a Karman ogive in the figure.

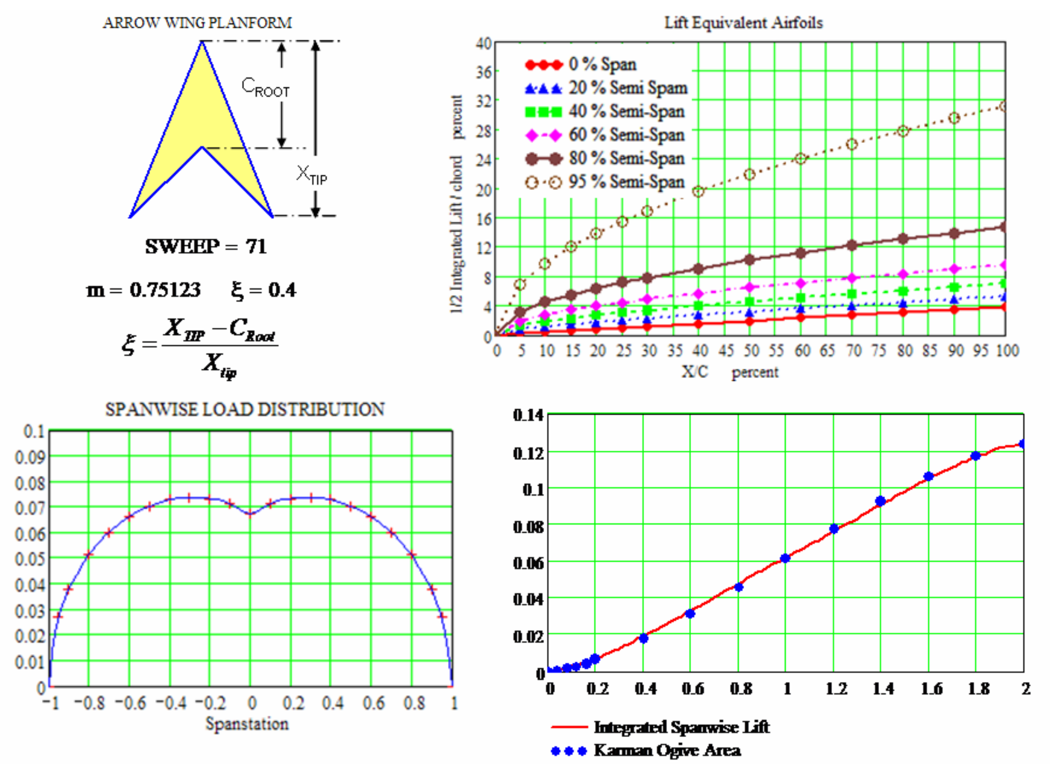

Figure 45 Arrow Wing Lift Equivalent Airfoils and Spanwise Load Equivalent Body, Mach 2.4

Calculated far-field wave drag due to lift and induced drag are compared with the near field conical flow theory exact values in figure 46. In spite of the slight dip in the spanwise load distribution, the induced drag is seen to be very close to the minimum induced drag.

The combined far field wave drag due to lift plus induced drag is close to the conical flow values except the region where the leading edge becomes supersonic. This is believed to be due to the rather sparce definition of the equivalent airfoils used in the wave drag due to lift calculations. Comparing the results in figures 44 and 46 it is seen that the drag due to lift of the arrow wing is significantly lower that that of the delta wing. This is the result of removal of the less efficient area of the wing for producing lift.

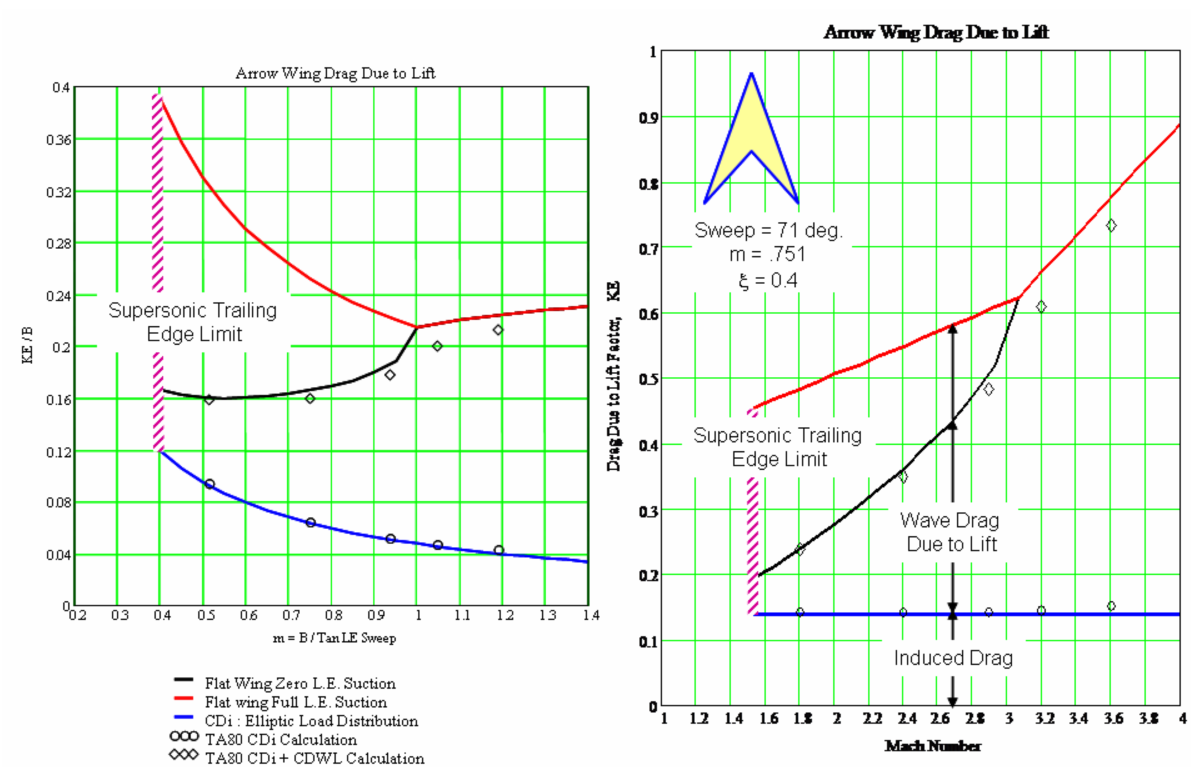

Figure 46. Supersonic Drag Due to Lift for a Notched Arrow Wing

XXI.   Fundamental Assumptions of the Area Rule

It is important to understand the fundamental assumptions and resulting restriction of the far field wave drag calculation method in order to be confident in the drag predictions. A common source of “FFD” (flawed fluid dynamics) as well as “WFD” (wrong fluid dynamics) is careless and or / uneducated use of the various computational methods.

The primary assumptions inherent in far field wave drag calculation methodology:

- *A complete aircraft configuration can be represented by linear combinations of planar and/or line source / sink distributions.*
- *The required source / sink distributions for the complete aircraft geometry is equal to the sum of the source / sink distributions of the individual components of the airplane*
- *The source / sink distribution necessary to represent any of the configuration components is not affected by the presence of other near by component geometries*
- *Consequently the interference potential between adjacent components is neglected.*

These assumptions mean that the area rule calculation method is essentially restricted to symmetric mid-wing body plus tail configurations.

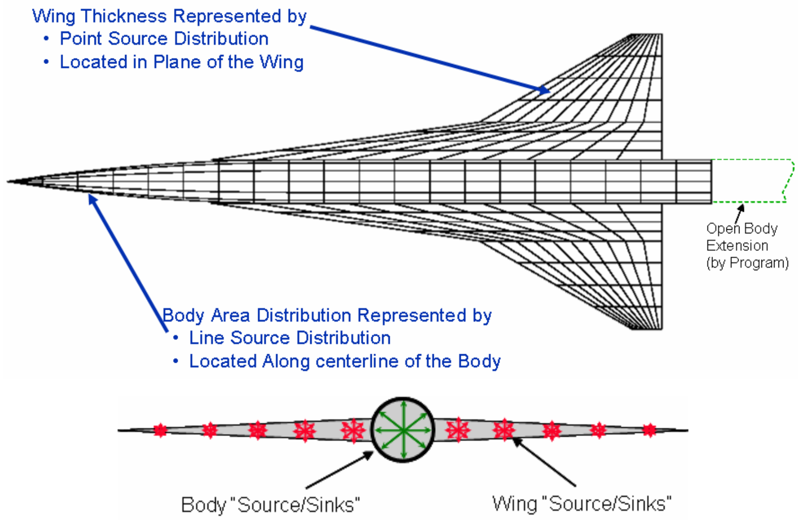

Figure 47. Symmetric Wing Plus Body Configuration

For a wing the boundary condition is: $\dfrac{w(x,y)}{V} = \lambda(x,y)$

As shown in figure 47, only the wing source located at the point x,y contributes to the vertical velocity at that point. The body sources do not contribute the vertical velocity in the plan of the wing.

The wing sources from the left and right wing panel cancel each other on the body axes. Therefore the body required source distribution is exactly the same as for an isolated body.

Direct calculations of the wave drag for non- symmetric configurations such as cambered wings, high or low mounted wings, wing mounted nacelles violate these restrictions and can lead to either small prediction errors (FFD) or in some instances large errors (WFD).

In some instances the judicious use of geometric images can result in accurate answers.

Figure 46 shows a typical aft mounted nacelle configuration. For this type of configuration, the nacelles can be represented by linear source distributions. Since the nacelles are located below the wing, the nacelle sources can induce vertical velocities in the plane of the wing as well as on the body. Consequently neglecting the interference potential necessary to cancel the nacelle induced velocities on the wing and body can lead to significant drag prediction errors.

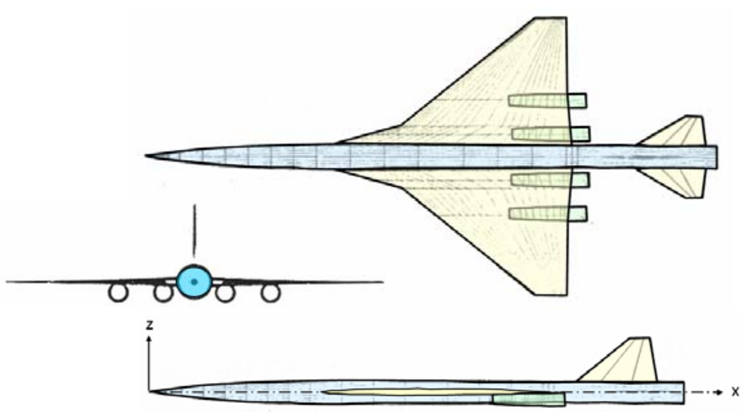

Figure 48 Typical HSCT Configuration

The effect of the neglecting the interference potential can be understood by examining the various nacelle / airframe aerodynamic interactions. As shown in figure 49.

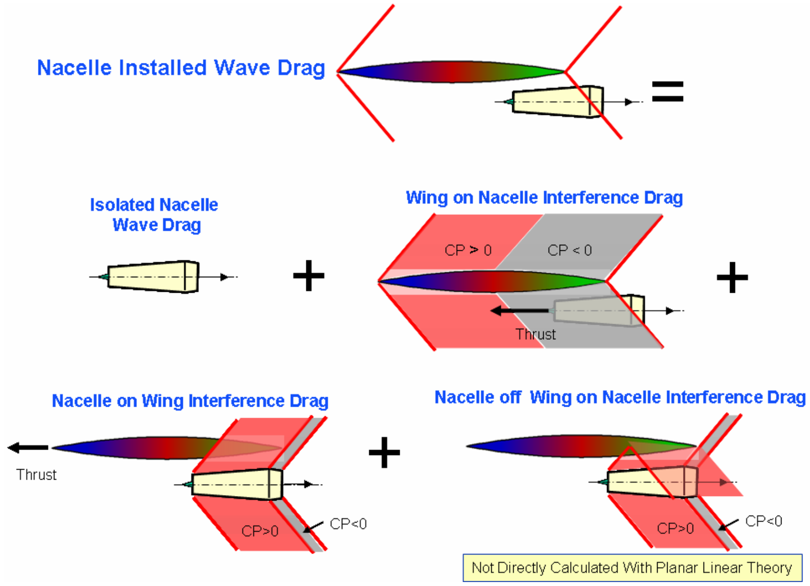

Figure 49 Wing mounted nacelle Aerodynamic Interactions

The nacelle installed wave drag includes:

- the isolated nacelle drag
- the buoyancy drag of the wing pressures acting on the nacelles
- the nacelle pressures pushing on the wing
- the mutual nacelle interference
- The nacelle pressures glancing off the wing lower surface back onto the nacelles.

The first four drag components are correctly calculated with the nacelles located below the wing and body with the supersonic area rule. The fifth drag component is not correctly calculated since supersonic area rule methodology effectively allows the nacelle pressures to “pass through” the wing surface without reflecting back on the nacelles. In order to “block” the nacelle pressures from passing through the wing surface additional singularities of the lifting type would be required. These additional singularities are examples of the interference potential that is lacking in the standard area rule theory.

The effect of the nacelle pressures reflecting off the wing and back on to the nacelles can have a significant effect on the drag of the nacelles as shown in figure 50. The effect of a reflection plane, as shown in the figure can also be represented by the use of images. The linear theory predictions obtained with an image body match the test data quite well except at the Mach numbers close to 1.

The plane of symmetry between the pair of nacelles is equivalent to a reflection surface.

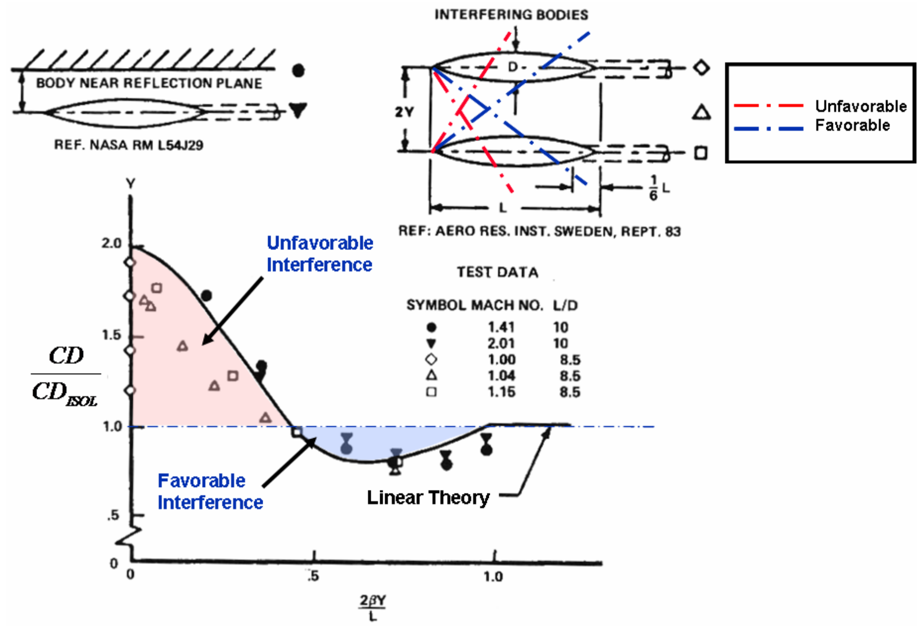

Figure 50. Use of Images to Simulate Nacelle Reflection Interference or Mutual Nacelle Interference

Consequently, through the use of images as shown in figure 51, the nacelle installed nacelle effects on wave drag can be calculated including all of the drag elements as shown in the figure. Notice that the images used in the nacelles plus images analyses represent that portion of the nacelle for which the nacelle pressures are reflected off the wing surface.

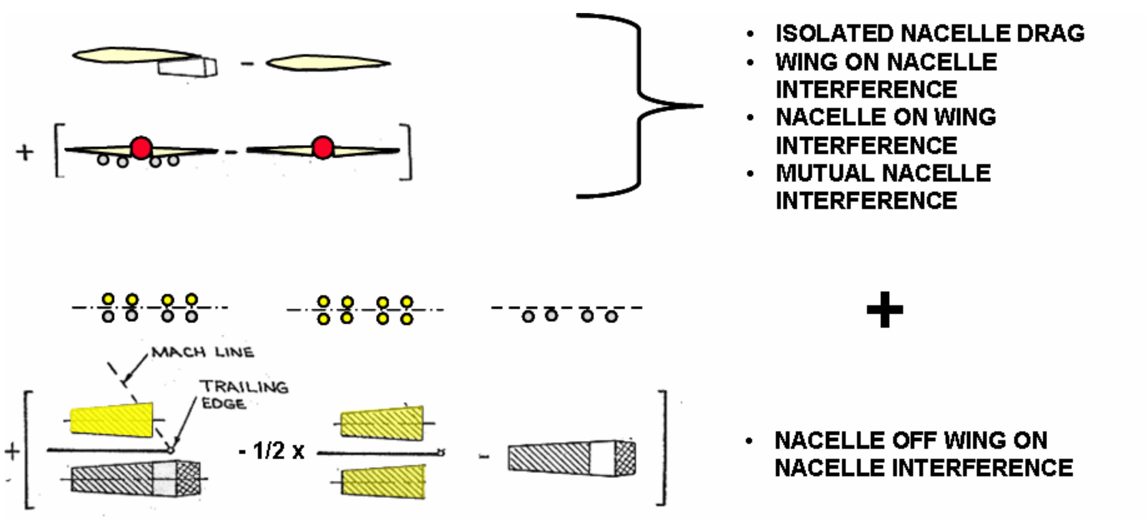

Figure 51. Far-Field Calculation of Nacelle Wave Drag With Images

XIII. Nacelle Airframe Integration

The nacelle / airframe interference effects can have a profound effect on the aerodynamic efficiency of a supersonic aircraft as shown in figure 52. This figure contains three drag polars including the wing + body, the wing + body + a drag increment equal to the isolated drag of the nacelles, the drag of an efficiently integrated wing + body + nacelles configuration. The differences between the drag of the integrated wing + body + nacelles configuration and the wing + body configuration + the drag of the isolated nacelles is the favorable aerodynamic interference inherent in the complete configuration. As shown in the figure, the favorable nacelle interference drag equaled nine drag counts, ($\Delta CD = -0.0009$). This resulted in a maximum takeoff weight reduction, ($\Delta TOGW$) for the airplane equal to approximately 90,000 lbs. This also resulted in a fuel savings for the design mission equal to 67,500 lbs. The drag reduction effect is equivalent to a structural weight of approximately 18,000 lbs.

It should be noted that a poor nacelle installation could result in a nacelle installed even greater the isolated drag level.

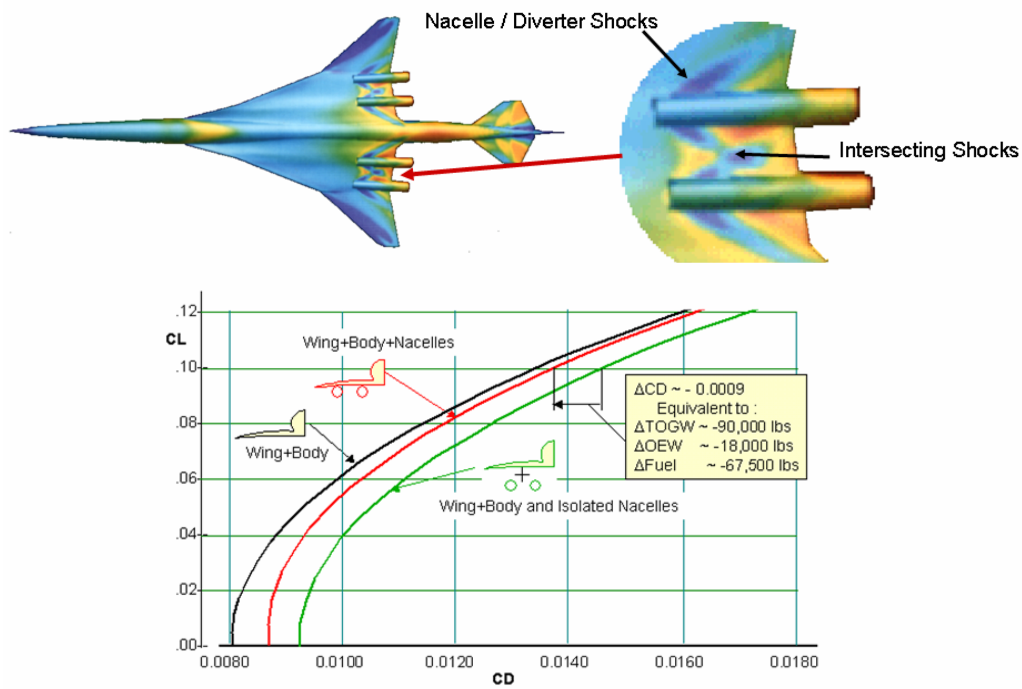

Figure 52 Impact of Favorable Nacelle – Airframe Favorable Aerodynamic Interference.

In order to explore the design features that affect the efficiency of the nacelle installation, let us first identify all of the drag components.

Typically, the nacelle installed drag [34], as shown in figure 53, is calculated as the sum of the friction drag of the nacelles, the net wave drag, and the lift interference effects.

The net nacelle wave drag as previously discussed includes:

- Nacelle pressure drag.
- Nacelle pressures acting on the wing-body volume or thickness
- The wing-body thickness pressures acting on the nacelles .
- Mutual nacelle interference which consists of the effect of the pressure field of the nacelles acting directly on the other nacelles plus the effect of the pressure field reflecting off the wing surface back onto the nacelles.

The lift interference consists of three items:

- The nacelle pressures reflecting off the wing produce an interference lift, ΔCL. Because of the interference lift, the wing-body incidence required to produce a specified total lift is reduced. This results in a reduction in the wing-body drag due t o lift.
- The nacelle pressures acting on mean lifting surface produce a drag or thrust force.
- The wing lifting pressures produce a buoyancy force on the nacelles.

The net nacelle drag is therefore dependent not only on flight conditions and the shape of the nacelles but also on the shape and location of adjacent components of the airplane.

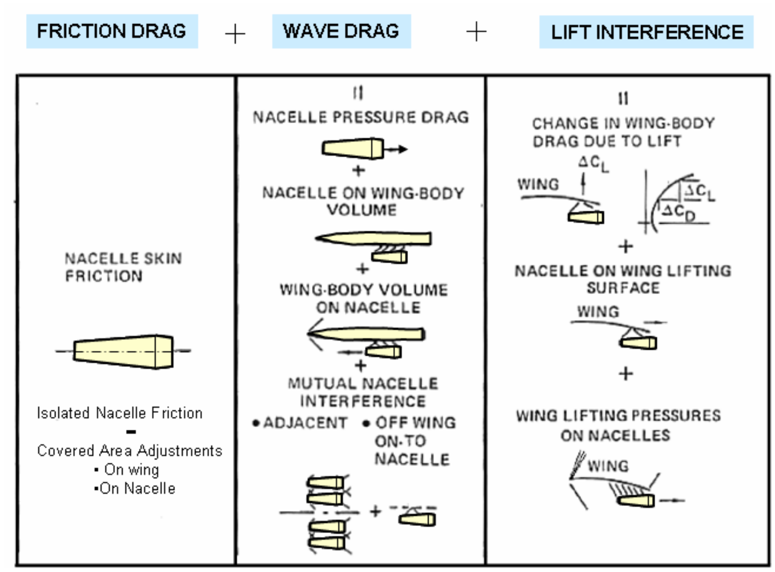

Figure 53. Nacelle Installed Supersonic Drag Components

The shape of the nacelle is very important in achieving an efficient nacelle installation[35, 36]. This is illustrated in figure 54. The upper nacelle has a long conical shape back to the fully expanded jet nozzle. This nacelle geometry produces a large region of positive pressures associated with the expanding fore-cowl geometry, followed by small region of negative pressures resulting from the flow expansion from the fore-cowl onto the nozzle. This design offers the potential for the creation of a significant amount of favorable interference lift.

The second nacelle geometry has a short conical fore-cowl followed by a cylindrical mid section, followed an under expanded jet contracting nozzle. The fore-cowl produces a small region of positive pressures followed by a large region of negative pressures that essentially cancel the positive pressure field.

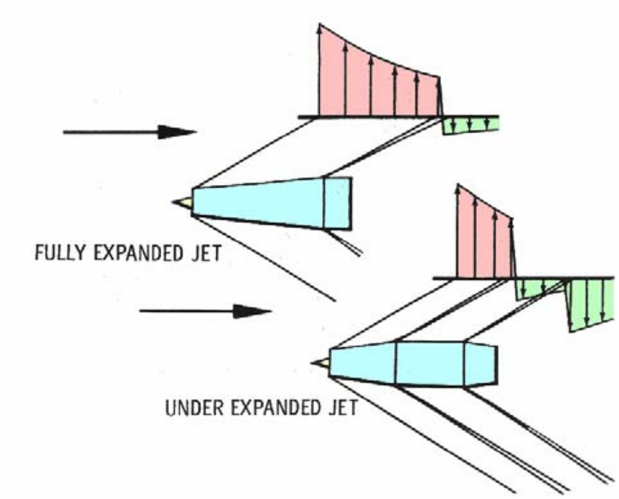

Figure 54 Effect of Nacelle Shape on Interference
Pressure Distribution

Figure 55 shows both desirable and undesirable locations for the expanding nacelle design. Locating the nacelles aft of the wing maximum thickness allows the nacelles fore-cowl pressures to produce a thrust force by pushing forward on the wing. The wing thickness pressures tend to be negative aft of the maximum thickness creating a favorable buoyancy thrust force on the nacelles. Conversely, locating the nacelles further forward on the wing can result in interference drag rather interference thrust effects.

The lateral spacing of the nacelles and the distance of the nacelles below the wing surface affect the mutual nacelle interference.

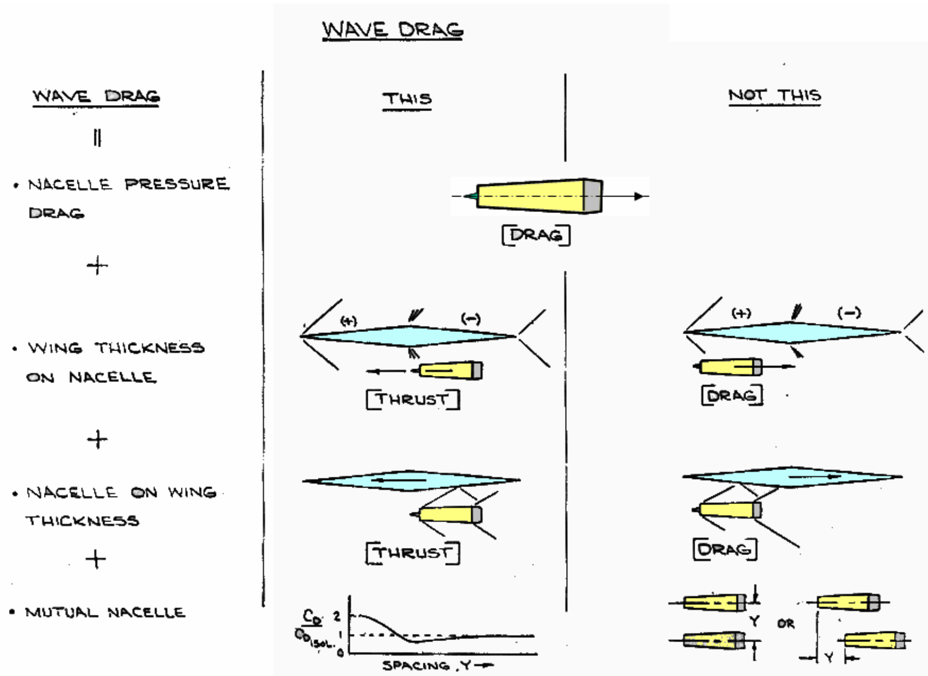

Figure 55. Nacelle and Wing Thickness Interference Installation Considerations

For the favorable nacelle shape, the nacelles locations have a significant effect on the lift interference effects as shown in figure 56. The lift interference effects consist of three components. The first component is the induced lift increment. For a constant total airplane lift, a positive lift increment can result in a savings in wing-body drag due to lift due to the associated reduction in angle of attack. The sign of the lift increment is very dependent on whether the nacelles are located above or below the wing.

The other two components include the nacelle pressures acting on the wing camber plus the wing lifting pressures acting on the nacelles producing either a buoyancy drag or thrust. These two components are typically of opposite sign to the first component. A moderate amount of wing reflex can be used to moderate these latter two effects.

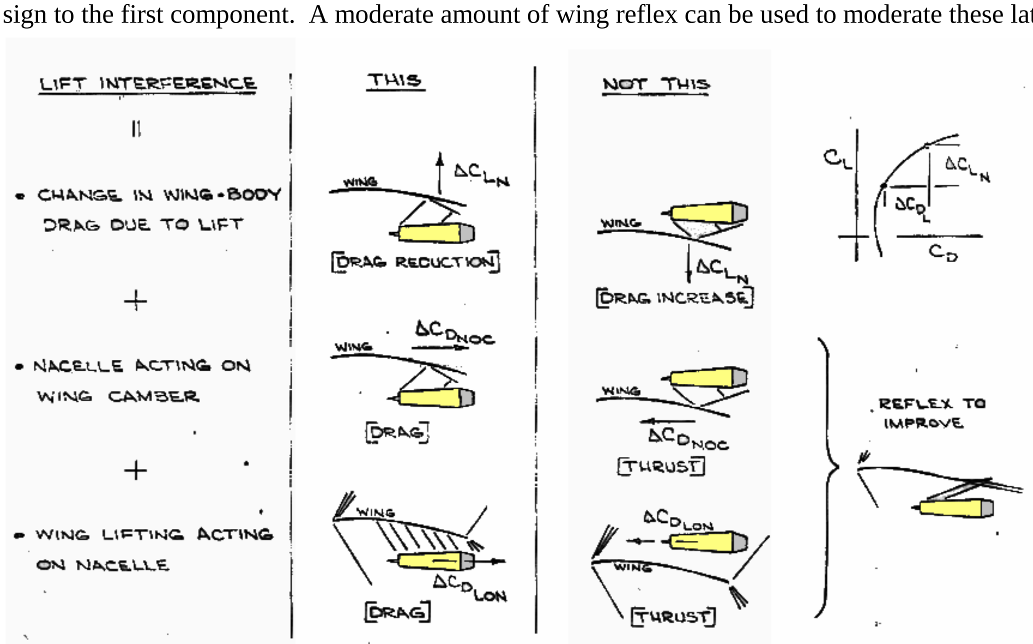

Figure 56. Nacelle and Wing Camber Interference Installation Considerations

Figure 57 illustrates how the nacelle shape and location can significantly affect the nacelle induced lift for a below wing installation

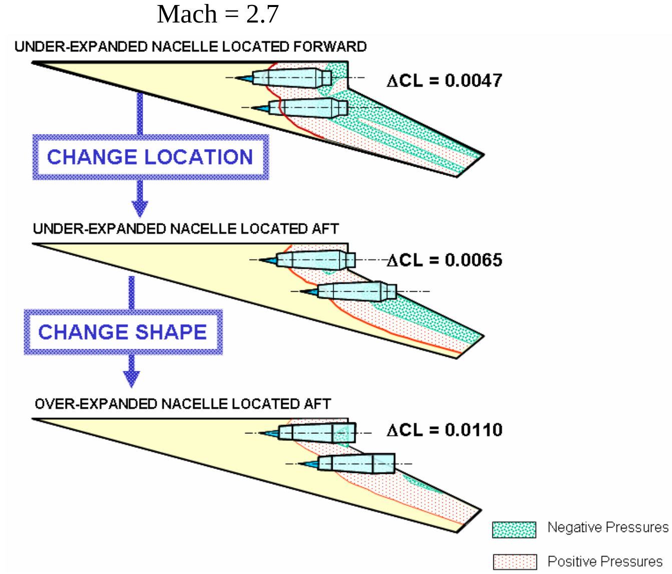

Figure 57. Effect of Nacelle Location and Shape on Interference Lift

Figure 58 shows a picture of the model geometry used in a highly sophisticated wind tunnel test program conducted to measure the nacelle / airframe interference forces. The NASA experimental program was conducted in the NASA Ames 11- by 11-foot Unitary Wind Tunnel [37, 38, 39].

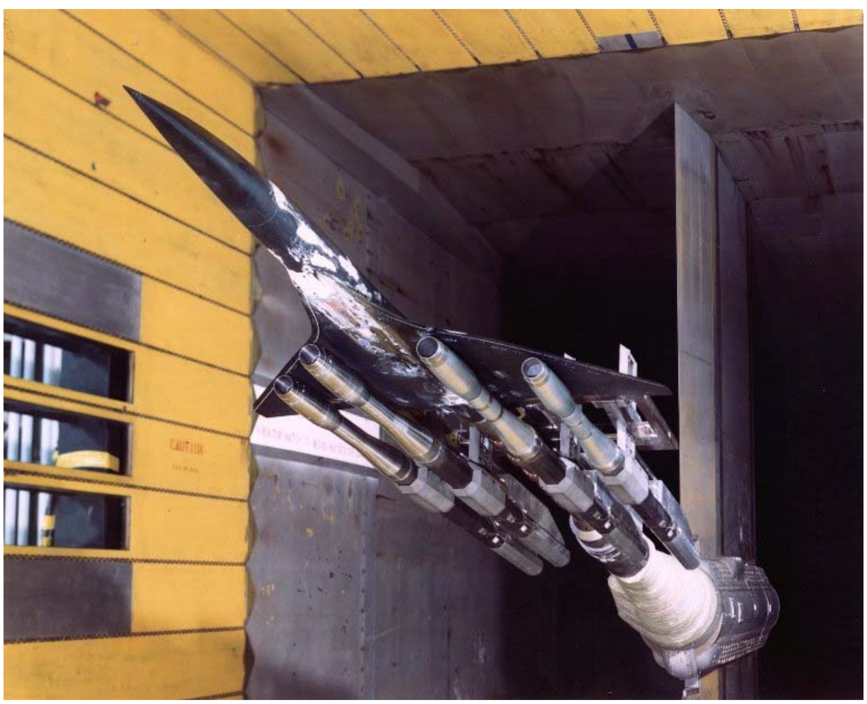

Figure 55. NASA Ames Propulsion-Aerodynamic Interference Wind tunnel Model

The wing-body configuration was a .024 scale model of the 1971 SST. The wing-body was sting mounted with a six-component internal strain-gage balance. The left-hand wing had 126 static pressure orifices with 95 on the lower surface and 31 on the upper surface. The nacelles centerlines were located approximately 1.2 inlet diameters below the wing chord plane. This resulted in a gap between the nacelles and the wing lower surface that does not exist in an actual nacelle/airframe installation.

The four individual nacelles were supported below the wing-body model on individual flow-through-stings. The two left-hand side nacelles (looking upstream) were pressure instrumented. The two right-hand side nacelles were mounted individually on separate six-component internal strain-gage balances.

The pressure instrumented nacelles had 40 static-pressure orifices.

The six-component force balances used to support the right-hand nacelles were housed in the thickness of each nacelle. A two-shell flow-through balance located in each nacelle used four instrumented flexures located 90 deg. apart at two axial locations. The nacelle balances measured the aerodynamic forces on the external surface of the nacelle, plus the forces on a small portion of the internal duct near the inlet. The wind tunnel data corrections included removal of the estimated skin friction drag on this small internal duct area.

The nacelle support system provided the flexibility of positioning the nacelles vertical, streamwise, and spanwise, relative to the wing-body combination and to each other.

The support system also provided for independent control and measurement of mass flow through each nacelle by means of a mass-flow control plug and appropriate pressure instrumentation.

The test configurations included:

- Isolated wing-body
- Isolated nacelle
- Four nacelles in various relative positions
- Wing-body plus nacelles in various locations
- Isolated nacelle

The test data included:

- Wing-body lift (CL), drag (CD) and pitching moment (CM) data
- Wing pressure measurements.
- Lift, drag and pitching moment measurements of the individual inboard and outboard nacelles .
- Nacelle surface pressures

These tested configurations provided the following measurements of isolated and interference data:

- Isolated wing-body data → measurements on wing body without the nacelles present.
- Isolated nacelle data → measurements on a singly tested nacelle.
- Mutual nacelle interference → difference in nacelle measurements with and without the other nacelles present.
- Nacelle interference on wing-body → difference in wing-body measurements with and without the other nacelles present.
- Wing-body interference on the nacelles → difference in nacelle measurements with and without the wing-body present.
- Total wing-body plus nacelle data → sum of wing-body data plus nacelle data.
- Spillage interference → difference in measurements on identical configurations with the nacelles spilling according to a specific controlled mass flow ratio (MFR), and the corresponding data obtained without spillage.

This extensive results from this test program provides an extensive database for code validation studies as well as a fundamental understanding of the components of nacelle airframe interference.

Detailed studies [34, 40] were made to compare the linear theory predictions of the tested configurations with the experimental test data. Some of the results of these studies are shown in figures 59, 60, and 61 to illustrate some of the interference concepts that have been discussed above.

Figure 59 shows measured mutual nacelle interference effects at two different Mach numbers for different nacelle longitudinal arrangements.

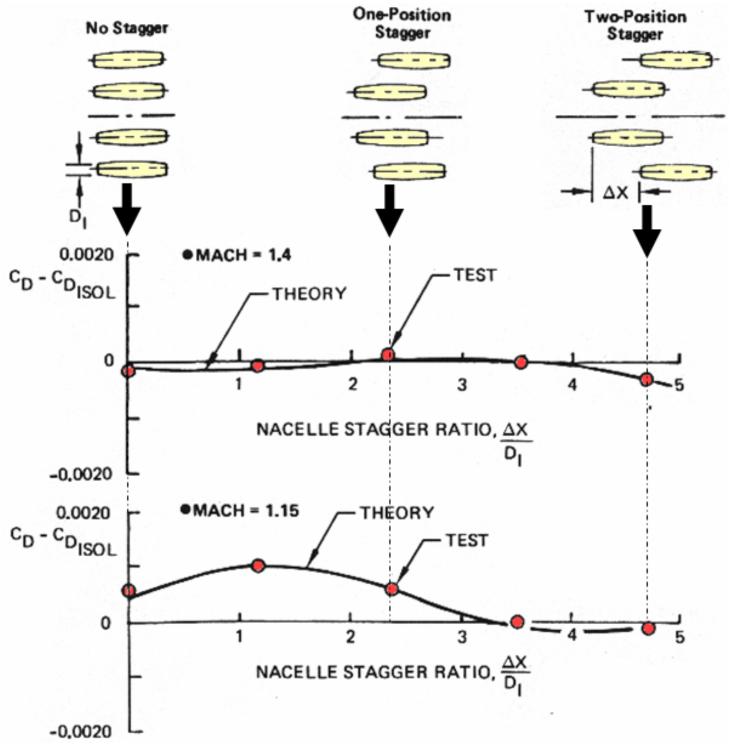

Figure 59. Effect of Nacelle Stagger on Nacelle Mutual Aerodynamic Interference

It is seen that the predicted mutual interference drag closely matches the test data. Nacelle stagger is seen to have a significant on the interference drag at the lower Mach number.

Figure 60 shows various wing interference components as they are affected by the angle of attack for an aft located nacelles location. The linear theory predictions are seen to agree well with the test data.

The net interference of the nacelles on the wing body is seen to be highly favorable and increase significantly with angle of attack. For a typical cruise lift coefficient of about CL ~ 0.15 to 0.20 for this test Mach number, The wing + Body acting on the nacelle is slightly unfavorable. The nacelle induced interference lift is seen to be approximately constant with increasing angle of attack. The measured isolated nacelle drag for the four nacelles agrees with the theoretical skin friction plus wave drag predictions. As a result of the favorable aerodynamic interference the total nacelle installed drag is seen to be significantly less than the isolated nacelle drag and ultimately cancels the nacelle isolated wave drag.

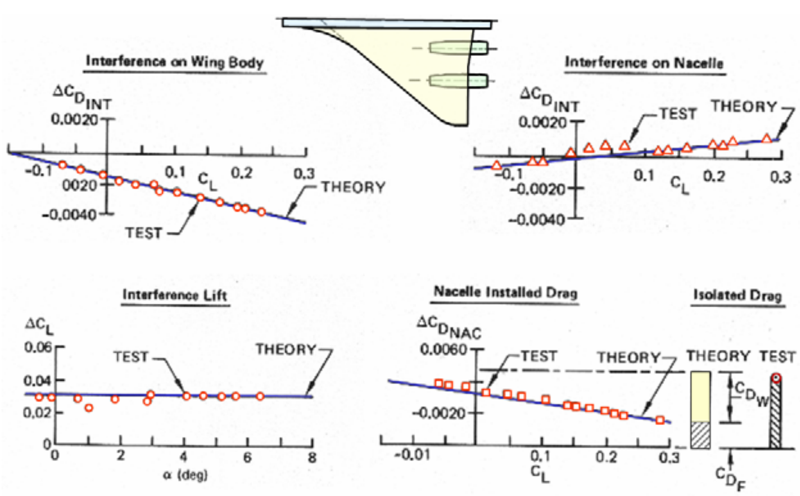

Figure 60. Example of Aft Located Nacelles Favorable Aerodynamic Installation – Mach 1.4

Similar results are shown in figure 61for a forward nacelle location at Mach 1.4. In this instance, the linear theory predictions do not match the test data well although the trends are similar. The strongly unfavorable aerodynamic interference affect of this installation resulted in an installed nacelle drag approximately equal to twice that of the isolated drag.

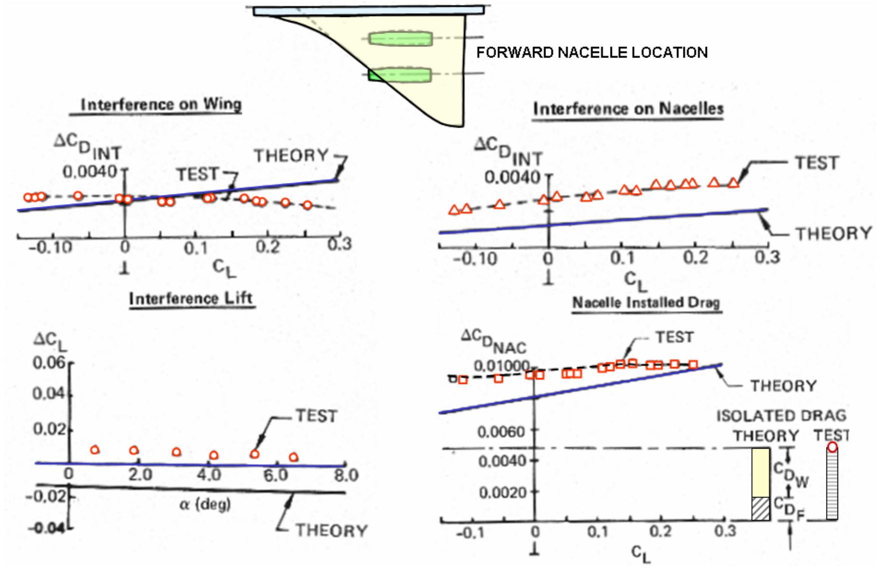

Figure 61. Unfavorable Aerodynamic Interference Forward Nacelle Location

Figure 62 shows the installed nacelle drag for the optimized nacelle installation on the Boeing US SST configuration. It is seen that beneficial effects of the wave drag interference and the lift interference combine to produce a total nacelle installed drag increment that is less than the skin friction drag of the isolated nacelles. This result is typical of an aerodynamically efficient supersonic nacelle installation.

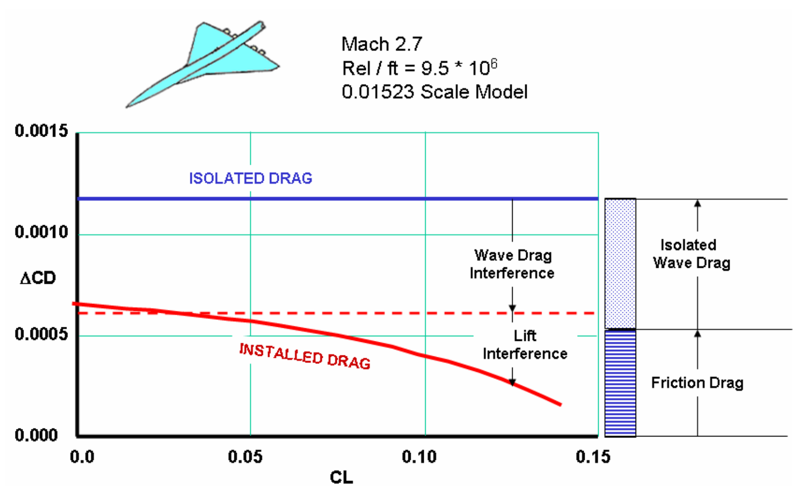

Figure 62. Nacelle Installed Drag for an Aerodynamically Efficient Installation

XIV. Parasol Wing Aerodynamics

In this section we will use some of the previously described aerodynamic tools and concepts to explore the fundamental nature of the rather complicated aerodynamic interactions for a parasol wing. We will use a combination. of "UFD" (understanding fluid dynamics), "LFD" (linear fluid dynamics) , "SFD" (simplified fluid dynamics) and "AFD" (approximate fluid dynamics).

Previous investigations [9, 41 to 47] have shown that the parasol wing-body arrangement can combine wave cancellation and interference lift effects into an aerodynamically efficient design. The body in a parasol wing arrangement is positioned below the wing, so that, at supersonic speeds, the bow shock and forebody pressure field impact on the wing lower surface. The body wave cancellation effect is produced by the body pressures glancing off the wing surface, and back onto the aft end of the body. This effect produces a thrusting force. The body pressures reflecting off the wing also produce a favorable interference lift force. The wing lower surface lifting pressures push on the aft end of the body to produce a favorable thrust force. The fundamental aerodynamic interactions [46, 47] of a parasol wing are shown in Figure 63.

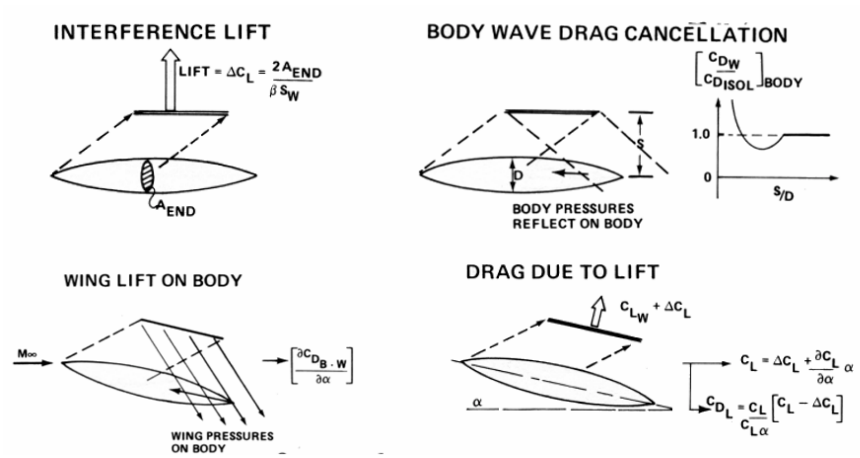

Figure 63 Parasol Wing fundamental Aerodynamic Interactions

A number of parametric studies were made to investigate the body wave drag cancellation and interference lift generation for a body located below a wing [46,47]. Some of the results are shown figures 54 through 67. The analyses were made for Mach 3.0. However, the results can be applied to other Mach numbers by scaling the spacing between the body and the reflection surfaces distances by the ratio $2\sqrt{2/\beta}$.

Wing anhedral can have a significant effect on the aerodynamics of the parasol. To study these effects we can use the image approach developed on reference 9 and shown in figure 50 to represent body pressure reflecting off adjacent surfaces. In figure 50 it was shown that a single image located at twice the distance of the body to the surface, can represent the interference effects between the surface located on the plane of symmetry located midway between the body and the image body.

Using results from the calculations of the interference effects of a single image nacelle located at different distances from the body, we can study the effects of wing anhedral and the approximate effects of a half ring-wing and a ring-wing by applying the principal of superposition. Results of such analyses are shown in figure 64.

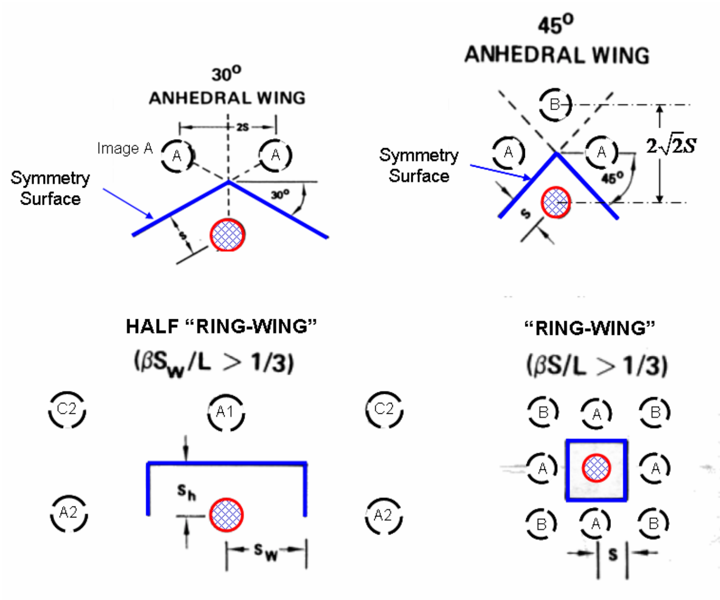

Figure 64 Simple Image Representation of Body Wave Drag Cancellation

The effect of 30 degrees of anhedral can be determined using two images "A" located at distances equal to two times the distance of the body from the reflection surface. The basic body and the two images are all located on the vertices of an equilateral triangle. Consequently the effect of 30 degrees of anhedral is to double the body reflection interference effect of a flat surface.

The effect of 45 degrees of anhedral can be simulated by three images. Two of the images are located at exactly the same distance as the images ("A") used for 30 degrees of anhedral. The third image ("B") is located at a distance $\sqrt{2}$ farther from the body than images "A". The interference effect of a simple square "ring-wing" can be calculated as the sum of the interferences of 4 images "A" plus 4 images "B". The interference effects of a simple square "half ring-wing" calculated as the sum of three images "A" plus two images "B".

Figure 65 shows the beneficial effect of anhedral on the interference wave drag of a body of revolution at Mach 3.0. It is seen that the favorable interference effect of 30 degrees anhedral doubles the interference relative to a flat reflection surface. The effect of 45 degrees of dihedral at the optimum spacing distance is nearly three times that of a flat surface.

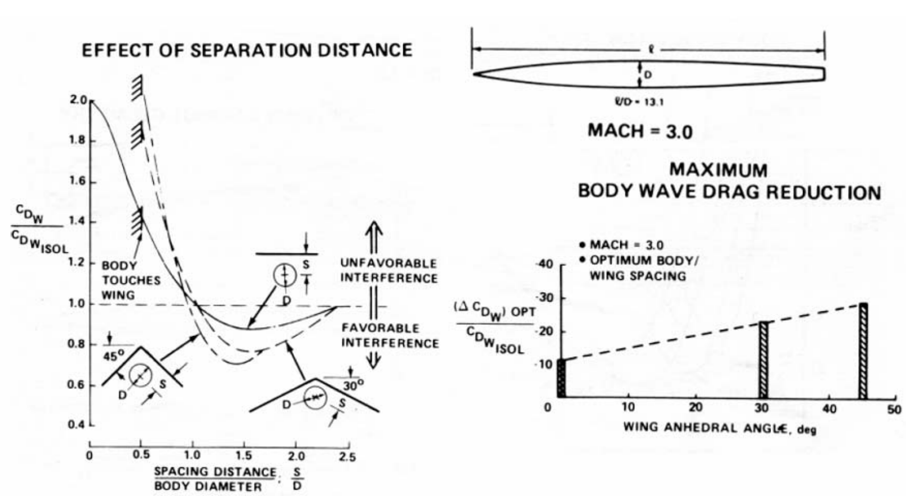

Figure 65. Wing Anhedral Effect on Body Wave Drag

The interference effects of the square "half ring wing" and the square "ring-wing" are compared with the results for the flat surface and 45 degrees of anhedral in figure 66. The "square" simulation of the half-ring and the ring-wing underestimates the theoretical interference for these geometries however the trends are certainly reasonable. The half ring wing geometry would reduce the body wave drag by 50% and the full ring wing would totally cancel the body wave drag.

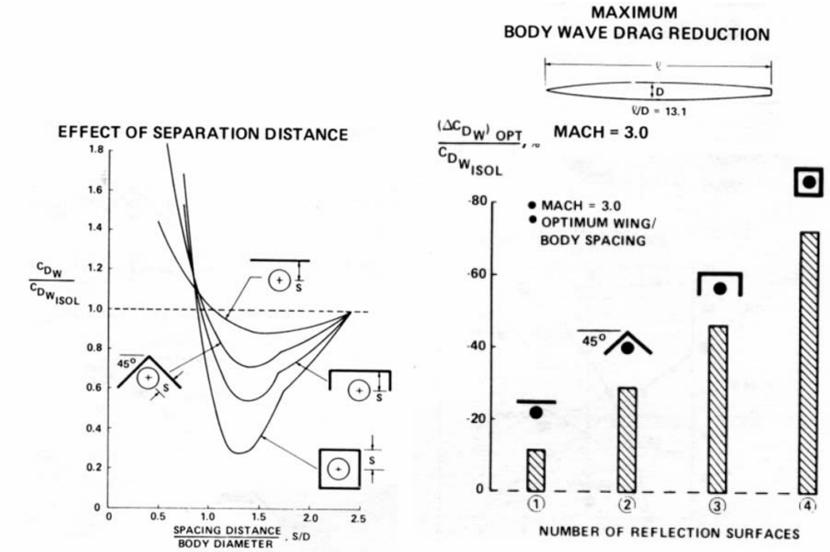

Figure 66. Ring-Wing and Parasol-Wing Body Wave Drag Cancellation Effects

The results of a simple study of the effects of the aspect ratio of a rectangular parasol wing are shown in figure 67.

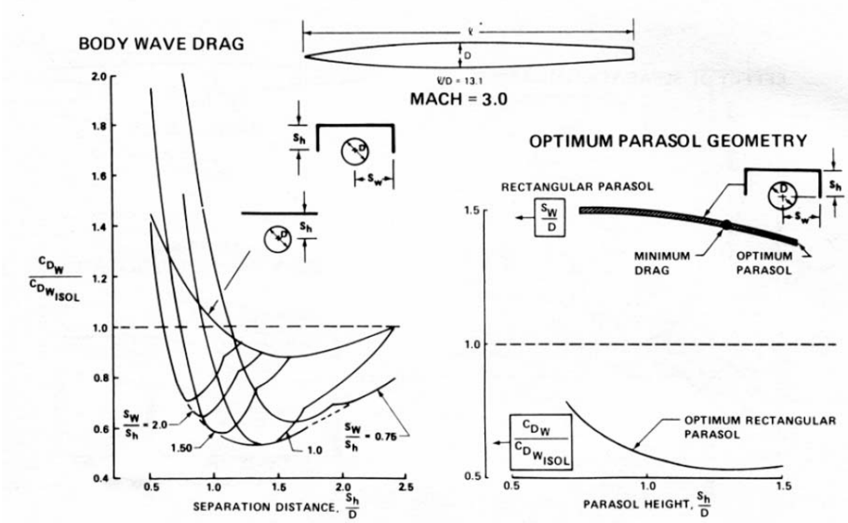

Figure 67. Optimum Rectangular Parasol Geometry

Using the image analogy, we can also calculate the effects of wing anhedral angle on the interference lift for a simple parasol wing as shown in figure 68. The slender body interference depends only on the cross-section area of the last station for which the pressures are captured on the wing.

The interference lift for a wing without dihedral is equal to $\left(\Delta CL\right)_{\Gamma=0\deg} = 2\left\{\frac{1}{\beta}\frac{A_{END}}{S_{REF}}\right\}$ 101

The "2" in equation corresponds to the total number of bodies required to simulate the solid surface. In this case this represents the body plus the single image body.

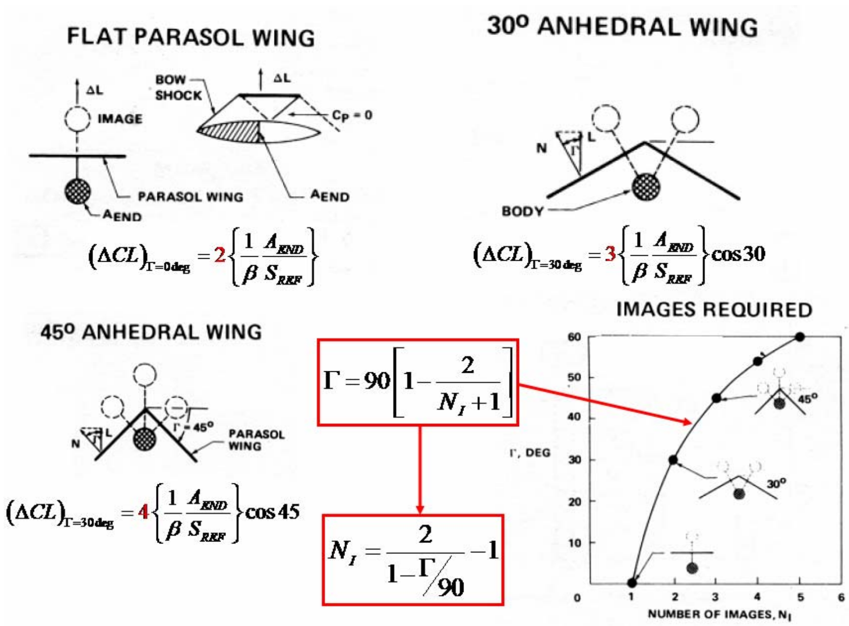

Figure 68. Image Representation of Parasol Wing Anhedral Effects on Interference Lift

Two images are required to simulate 30 degrees of anhedral. However the interference lift is rotated by the cosine of the anhedral angle. Consequently the interference lift is equal to:

$$\left(\Delta CL\right)_{\Gamma=30\deg} = 3\left\{\frac{1}{\beta}\frac{A_{END}}{S_{REF}}\right\}\cos 30 \qquad 102$$

By similar reasoning , the interference lift for 45 degrees of anhedral is equal to.

$$\left(\Delta CL\right)_{\Gamma=30\deg} = 4\left\{\frac{1}{\beta}\frac{A_{END}}{S_{REF}}\right\}\cos 45 \qquad 103$$

The number of images to represent a specific anhedral angle can be generalized and expressed as

$$\Gamma = 90\left[1-\frac{2}{N_I+1}\right] \qquad 104$$

Conversely, the number images required for a specific anhedral angle is:

$$N_I = \frac{2}{1-\Gamma/90}-1 \qquad 105$$

The interference lift can therefore be expressed as : $\Delta CL\left(\Gamma\right) = \frac{2K_\Gamma}{\beta}\frac{A_{END}}{S_{REF}}$ 106

Where the dihedral interference lift factor is: $K_{\Gamma} = \left(\frac{N_I + 1}{2}\right)\cos\Gamma = \frac{\cos\Gamma}{1 - \Gamma/90}$ 107
is shown in figure 69.

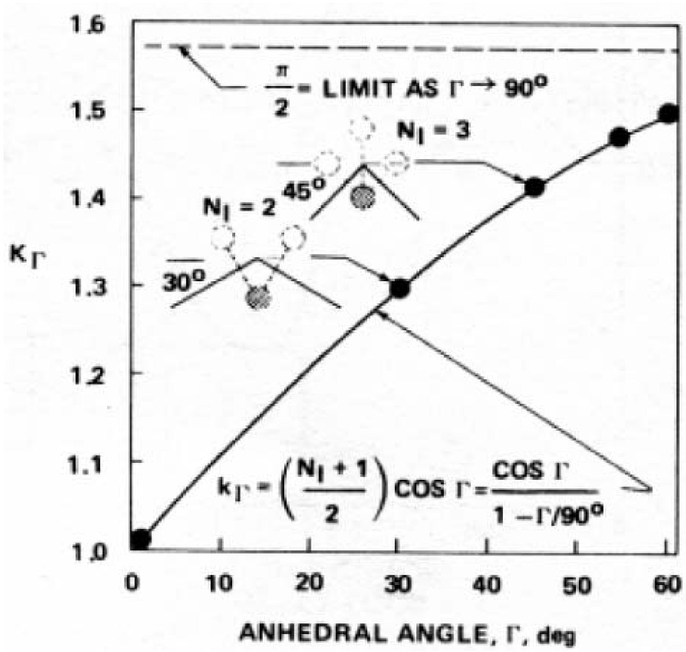

Figure 69. Interference Lift Anhedral Factor

<u>Paradox 4:</u> *From the discrete calculations of the number of images necessary to calculate the interference lift for specific anhedral angles we can develop a general analytic relation for the effect of any anhedral angle on the induced lift for a parasol wing.*

In order to validate the simple slender body predictions, a planform study was made to evaluate the effects of anhedral effects using the FLEXSTAB program [48]. This program is a linear potential flow program in which the singularity strengths are adjusted to satisfy the boundary conditions required by the geometry of the particular configuration. The interference potentials are therefore captured by this methodology. The study planforms were developed from the flat parasol configuration and are described in detail in reference 9. The results are compared with the simple slender predictions in figure 70. The anhedral effects on interference lift predicted by FLEXSTAB are very similar to the simple slender body trends.

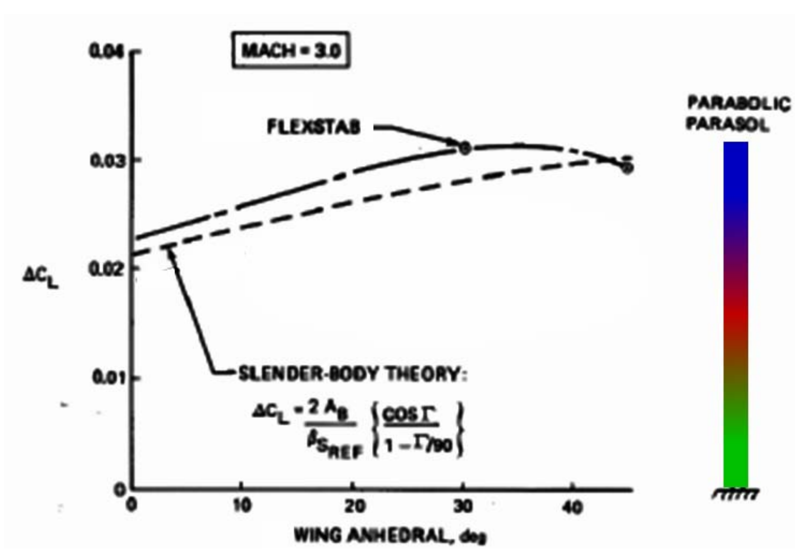

Figure 70. Anhedral Effect on Interference Lift.

The previously discussed fundamental parasol wing concepts were used to develop an advanced technology Mach 3 small supersonic fighter. The complete details of the development and configuration assessment processes are discussed in references [9, 47, 48]. The basic aerodynamic design considerations are illustrated in figure 71.

The wing planform was tailored to capture the positive pressure field of long conical fore-body nacelles. The nacelles were positioned to enhance the wave cancellation effects. The variable wing anhedral was defined as a "near parabolic" shape to maximize the nacelles induced interference.

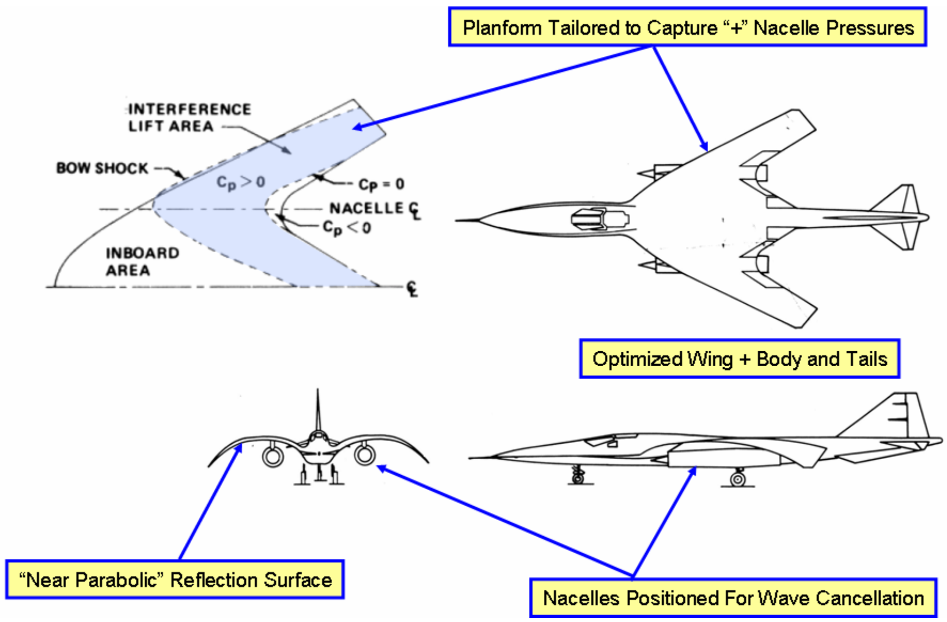

Figure 71. Double Parasol Wing Configuration Basic Design Features

Figure 72 is an artist's sketch of the resulting double parasol wing Mach 3 fighter.

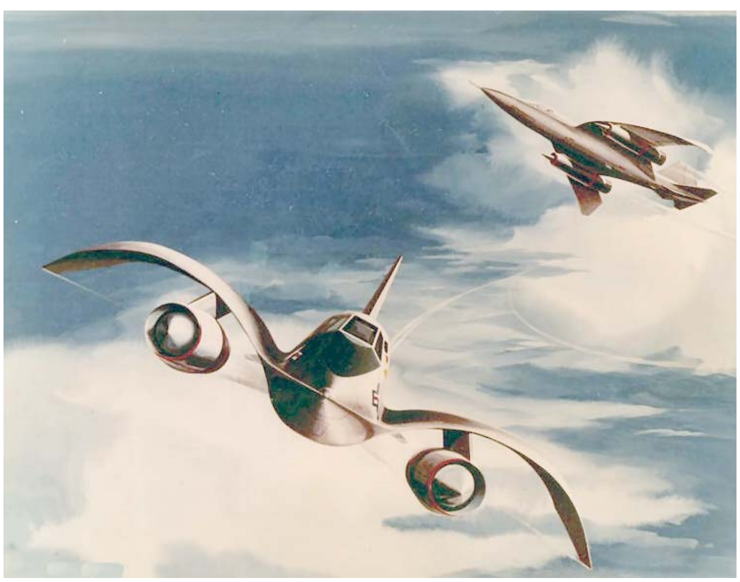
Figure 72. Double Parasol Wing Mach 3 Fighter

Figure 73 shows the relatively small double parasol fighter along with a supersonic transport aircraft. Both of these configurations utilize the same favorable aerodynamic concepts. It is readily apparent that the actual deployment of an aerodynamic concept is strongly dependent on the relative sizes of the primary aircraft components.

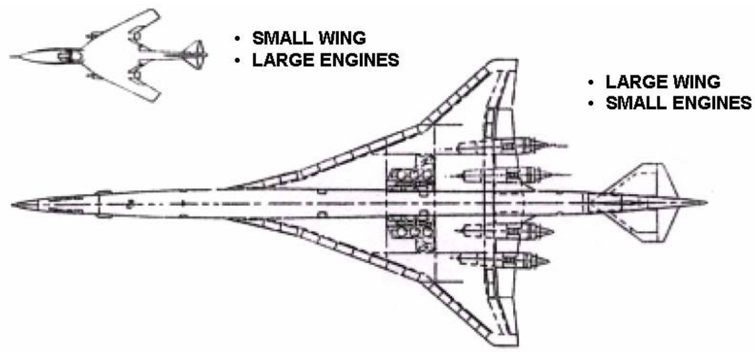

Figure 73. Size effect on Deployment of favorable aerodynamic concepts

XV. Fundamental Sonic Boom Concepts

When an airplane is flying over the ground the weight of the airplane is transferred to the ground as an increased pressure field on the ground [49] as shown in figure 74. For a low speed subsonic airplane, the increased pressure field has rotational symmetry with respect to the airplane and extends over a very large area. The increased pressure field travels at subsonic speeds with the airplane.

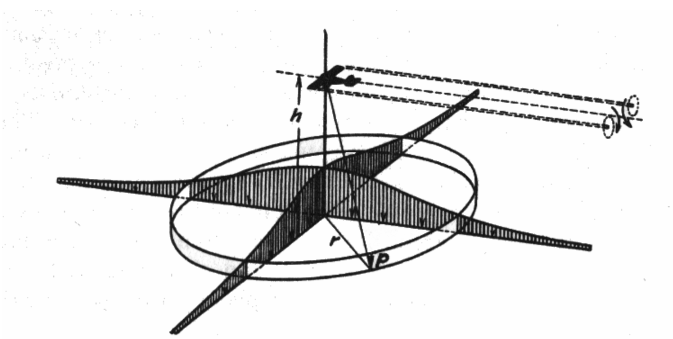

Figure 74. Subsonic Airplane Ground Pressure Field

The center of pressure of the induced pressure field is directly below the airplane. The maximum pressure occurs at the center of pressure and is given by the expression:

$$p_{\max} = \frac{W}{2\pi h^2} \qquad 108$$

The maximum ground pressure is extremely small since it varies inversely with the height of the airplane squared.

Consider for the example, a typical subsonic transport with a weight of 400,000 lbs flying at an altitude of 35,000 ft, the maximum pressure for this configuration is an imperceptible level equal to 0.000052 lbs/ft2

The pressure field generated by a supersonic airplane, however, is confined to the region between two shock cones. One emanating from the nose of the airplane, called the bow shock cone, and a second emanating from the tail which is called the aft or tail shock cone. The intersections of the shock cones with the ground each delineates a hyperbola, figure 75.

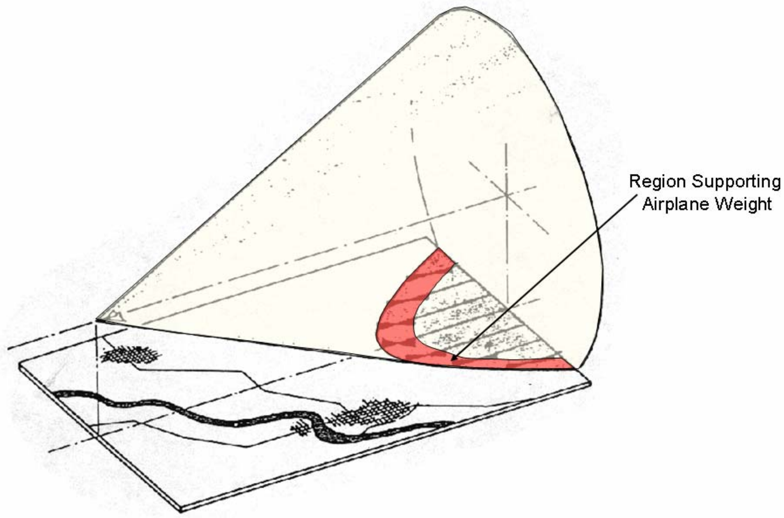

Figure 75. Supersonic Airplane Ground Pressure Field.

The characteristic shock generated flow features below the F-18 aircraft are shown in figure 76.

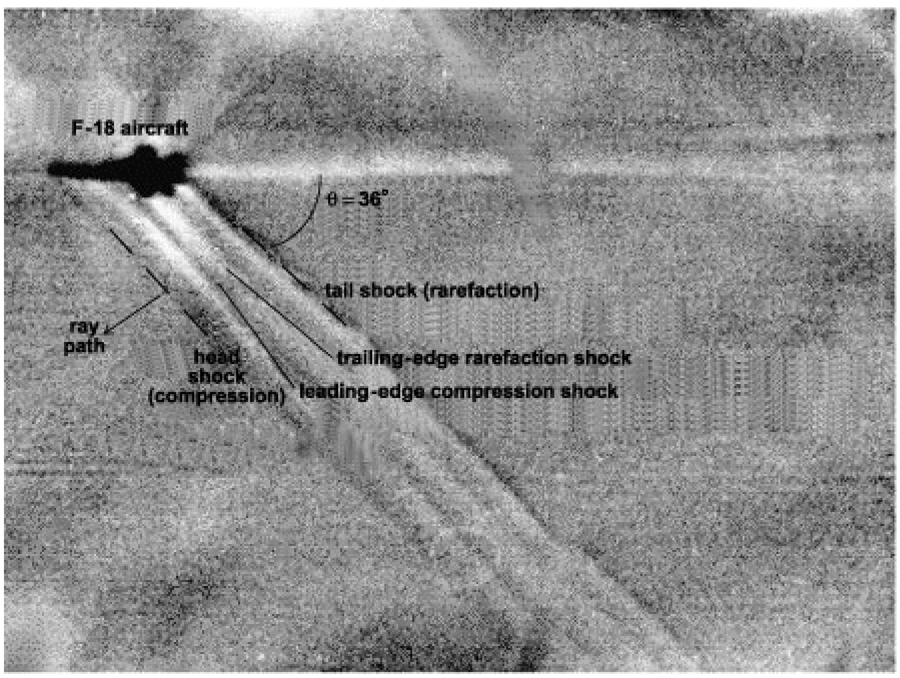

Figure 76: F-18 Shock Generated Flow Features

A typical HSCT configuration typically generates an entire system of shock waves in the near field close to the airplane [50, 5,1 523] as shown in figure 77. At large distances from the airplane, as indicated by the mid field, the shock wave system tends to steepen and begin to coalesce. At extremely large distances in the far field near the ground, the shock system will typically coalesce into a bow shock and a tail shock.

At the bow shock, a compression occurs in which the local pressure rises rapidly to a value "Δp", above the atmospheric pressure. Then a slow expansion occurs until some value below atmospheric pressure is reached, after which there is another rapid compression at the aft shock.

Generally the bow shock and the aft shock are of similar strengths, and the pressure varies linearly between the two shocks. This nominal sonic boom signature is called the "N" wave. This "N" wave moves at supersonic speeds with the aircraft.

The region between the defined by the area between the intersections of the bow shock and the tail shock is known as the primary sonic boom carpet. Receivers in this carpet detect the sonic boom, that is the “N” wave as the airplane passes.

The primary carpet sweeping past a person outside on the ground would result in a audible response as shown in the figure. Since the ear detects changes in pressures only above a certain frequency, it will respond only to the high frequency steep parts of the pressure waves and not to the low frequency gradual pressure changes in between.

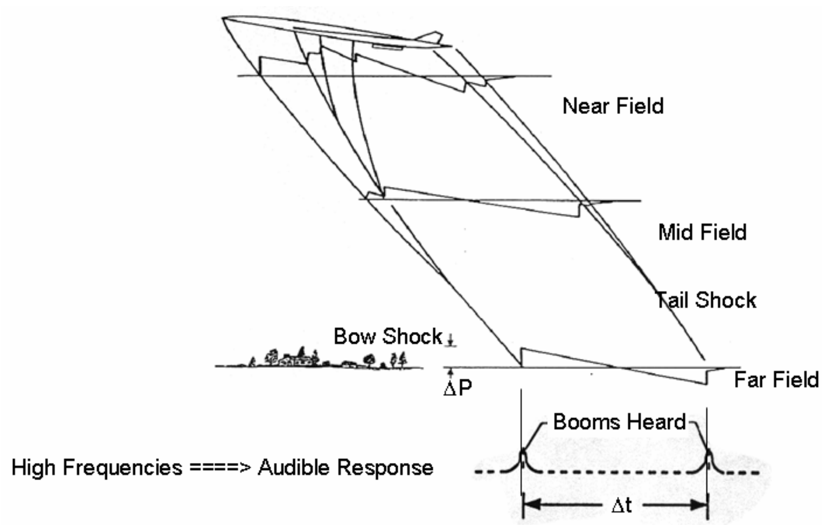

Figure 77. Shock Wave Structure and Sonic Boom

Similar to the subsonic airplane example shown in figure 74, the weight on the airplane must be supported by the integrated pressures in the sonic boom footprint area. Since this footprint is much smaller than the area supporting a subsonic aircraft, the pressures by necessity must be significantly larger than in the subsonic case. Such a result would seem to be self-evident since it is a direct consequence of the laws of classical mechanics, and the laws of mechanics are not violated by aerodynamic theory [53]. The system forces are shown in Figure 78.

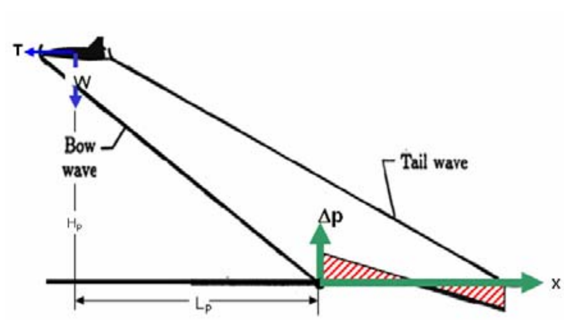

Figure78. The Fundamental Nature of Sonic Boom

1. Pressure supports the airplane weight. Therefore $$W = \iint_{A_{CARPET}} \Delta p dxdy \qquad 109$$

The fundamental laws of mechanics also require that there are no unbalanced forces or moments in a balanced system. The weight vector of the airplane is far forward of the supporting pressure field on the ground. Therefore the ground pressure signature must have both positive and negative areas to be able to create a moment that balances the weight vector moment. This leads to the typical “N” wave shape of a sonic boom signature.

2. Therefore the ground pressure distribution cancels the airplane moment. This was originally mentioned to the author by R.T. Jones.

$$W \cdot L_P = -\iint_{A_{CARPET}} (x \cdot \Delta p)dxdy \qquad 110$$

Where x is measured from the front of the pressure signature, and L is the distance

3. A non-lifting configuration such as a body of revolution also creates an "N" wave signature. Since there is no lift, the areas of the front lobe and aft lobe must be equal. The "N" wave thus results in a ground reaction moment. It is postulated by the author that this moment is the ground reaction to balance a force equal to the wave drag force acting on the body at an height H_P above the ground.

$$D_W \cdot H_P = -\iint_{A_{CARPET}} (x \cdot \Delta p)dxdy \qquad 111$$

4. For the general case of a lifting configuration that has volume wave drag, the ground moment must balance both the weight and the drag moments. This requires:.

$$W \cdot L_P + D_W \cdot H_P = -\iint_{A_{CARPET}} (x \cdot \Delta p)dxdy \qquad 112$$

Although we have continually referred to the ground pressure signature as an "N" wave, it is possible under certain under certain situations the shape may be substantially different that the "N" shape. However, even this modified pressure signature must still abide by the fundamental laws of mechanics.

Fundamentals of sonic boom:

- *Sonic boom for "Supersonic Flight" is fundamentally inevitable for a lifting configuration*
- *The pressure footprint must have both positive and negative regions*
- *The positive region must exceed negative region by an amount to balance the airplane weight.*
- *The pressure magnitudes in the positive and negative press must also produce a moment to balance the drag force moments.*
- *Design changes that modify the positive region by necessity will also modify the negative region in order to maintain the condition of force and moment balance.*
-

Shock waves produced by an airplane flying at speeds only slightly in excess of the local speed of sound potentially may not reach the ground 54 as shown in figure 79. This is caused by warm layers of air below the airplane that refract or bend the path of the shock wave. The higher atmospheric temperatures below the airplane lead to an increase in the local speed of the shock wave. If the local speed of the shock wave is the same as the airplane speed, at some altitude below the airplane the shock wave will be refracted back into the atmosphere and will not reach the ground. It will be perpendicular to the horizontal at that altitude. Below that altitude, the local speed of pressure disturbance is greater than the airplane speed, and a subsonic pressure disturbance with a gradual pressure rise will occur. When an airplane speed is just equal to the speed of sound at the ground, the airplane Mach number is defined as "the threshold Mach number"

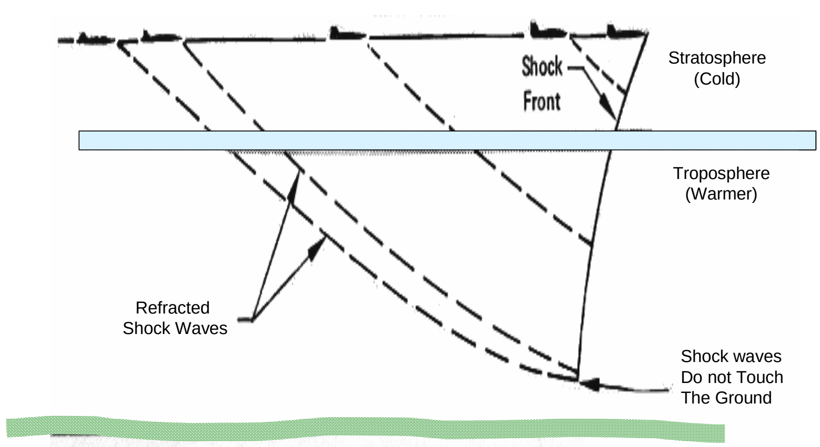

Figure 79. Flight at Mach Numbers Lower Than the Threshold Mach Number

The Threshold Mach number is dependent on variations in temperature and wind gradients between the airplane and the ground [55]. As a result, it can vary from day to day and place to place. Head winds in the vicinity of the airplane increase the threshold Mach number while tailwinds tend to decrease it. Consequently as shown in figure 80, depending on the local cruising wind conditions and the seasonal atmospheric temperature variations, it is possible to fly at local cruise Mach numbers between 1.04 and 1.25 without producing a ground sonic boom.

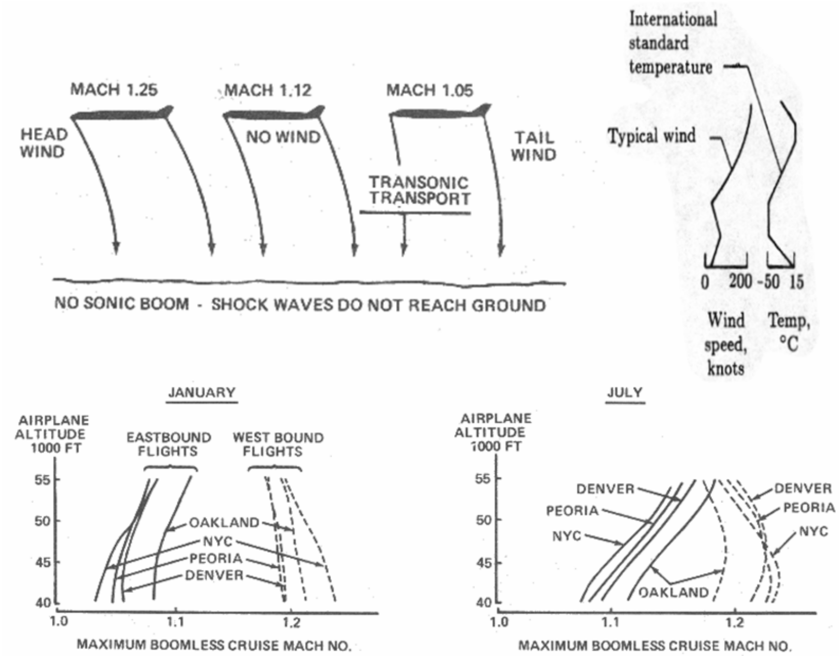

Figure 80 Low Supersonic Cruise Boom Free Flight Conditions

Physically, this means that,

- *Supersonic boom free flight is possible when the ground Speed of the airplane is less than the Local Speed of Sound on the Ground*

The use of advanced Global Positioning Systems, can provide a continuous and accurate measure of the ground speed. This together with local information about the temperature and wind could allow the boom free flight conditions to be determined and maintained.

Since boom free flight is an atmospheric phenomenon, the possibility of low supersonic speeds boom free flight cannot be validated in the wind tunnel. However flight test data such as shown in figure 81 have demonstrated that boom free flight at low supersonic speeds can be achieved.

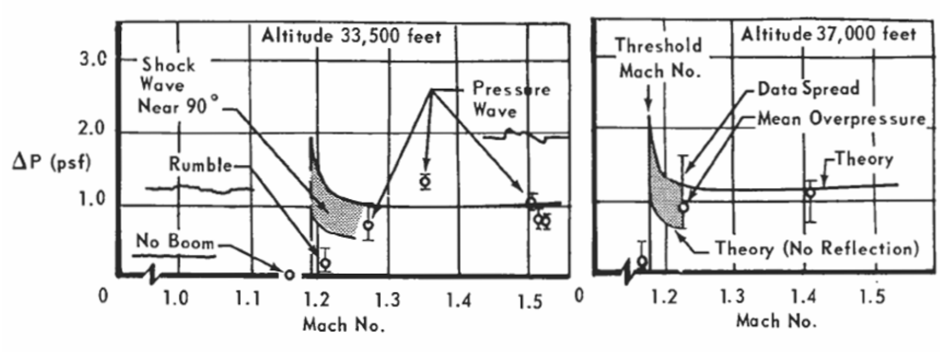

Figure 81. Flight Test Threshold Mach Number Measurements

Summary

A primary objective of this report was to use simple concepts and ideas to discuss the fundamental physics of supersonic wave drag and to the physically related phenomena of sonic boom. Some of the interesting results, observations and conclusions are summarized below.

1. Aerodynamic cruise drag has a highly leveraged effect on the size and performance of an HSCT design. A design improvement that results in a reduction of supersonic drag of 1% , which is approximately 1 drag count, ($\Delta CD \sim 0.0001$), will result in a reduction of approximately 10,400 lb. in the design Maximum Takeoff Gross Weight, MTOW. This also results in a fuel saving of about 7,500 lb. The net benefits are equivalent to reduction in the structural weight of more then one ton.

2. A number of apparent paradoxes were presented including:
   - **Paradox* 1**: *The Karmen-ogive minimum wave drag body for a specified base area can be derived directly from the subsonic optimum lift distribution for minimum induced drag.*
   - **Paradox 2**: *Numerical methods used to compute the supersonic wave drag for a body or revolution can be used to numerically compute induced drag for a specified lift distribution.*
   - **Paradox 3:** *The supersonic area rule, which is based on the implicit assumption that the control volume surfaces are so far from the body axes that shape does not matter, can define the shape of the optimum body to minimize the wing-body wave drag.*
   - **Paradox 4:** *From discrete calculations of the number of images necessary to calculate the interference lift for specific anhedral angles we can develop a general analytic relation for the effect of anhedral angle on the induced lift for a parasol wing.*

3. **The Reverse flow theorems can be easily derived from the wave drag equation:**
   - *The drag of a linear source distribution is equal in forward and reverse flow.*
   - *The drag of a given volume or thickness distribution is the same in forward reverse flows*
   - *The drag of a given distribution of lift is unchanged by a reversal of the flow direction.* In this case however the physical geometry such as camber, twist and angle of attack will by necessity be different for the forward and reverse flows.
   - *The drag of a general distribution of thickness, lift and side force elements in supersonic flow is the same in forward and reverse flight.*
   -

4. **The four Area Rules of Supersonic Flow Include:**
   - Near-Sonic Area Rule: Smooth cross-section area distribution to delay drag rise
   - Transonic Area Rule: wave drag of a configuration is equal to that of an equivalent equal cross-sectional body of revolution.
   - Supersonic Area Rule: Wave drag can be calculated as the averaged sum of "q" dependent equivalent bodies of revolution
   - Transfer Rule: For a given wing the minimum wave drag body is determined by optimizing the combined area plot

5. **Wave Drag Due to Lift:**
   - *The wave drag due to lift is proportional to β^2 and consequently vanishes as $M \rightarrow 1.0$*
   - *The wave drag due to lift is an absolute minimum of the lift distribution for each θ cut is elliptic.* This condition is known as the Jones lower bound wave drag due to lift which can only be achieved with yawed elliptic wing with a uniform load distribution
   - *The wave drag due to lift can be calculated using the volume wave drag equation with the local steamwise integrals of lift input as equivalent blunt base airfoils and accounting for the β^2 and $\sin^2\theta$ in equation 99*

6. **Sonic Boom Fundamentals**
   - *Sonic boom for "Supersonic Flight" is fundamentally inevitable for a lifting configuration*

- *The pressure footprint must have both positive and negative regions*
- *The positive region must exceed negative region by an amount to balance the airplane weight.*
- *The pressure magnitudes in the positive and negative press must also produce a moment to balance the drag force moments.*
- *Design changes that modify the positive region by necessity will also modify the negative region in order to maintain the condition of force and moment balance.*
- *Supersonic boom free flight is possible when the ground Speed of the airplane is less than the Local Speed of Sound on the Ground*

Acknowledgement

I should most likely have included the name of my long time mentor Armand Sigalla. Although he had nothing to do with the writing of this paper, he had everything to do with the content. It was through his great patience and willingness to share with me and my colleges, his unique wisdom and understanding of fluid dynamics, aerodynamics and sophisticated mathematical techniques, he not only made great contributions to the field of practical supersonic aerodynamics, but he also enabled all of us to grow in our careers.

Thank you my dear friend.

References

1. Kulfan, R.M. and Sigalla, A., “Real Flow Limitations in Supersonic Airplane Design:, AIAA-78-147, Jan. 1978
2. Kulfan, B. M., Reynolds Numbers Considerations for Supersonic Flight", AIAA-2002-2839, Jun 2002
3. Kulfan, B. M., “Assessment of CFD Predictions of Viscous Drag”, AIAA 2000-2391, June 2000
4. Harris, R. V., Jr., “An Analysis and correlation of Aircraft Wave Drag”, NASA TMX 947, Oct. 1961
5. Middleton, W. D., and Lundry, J. L., A Computational System for Aerodynamic Design and Analysis of Supersonic Aircraft. NASA CR-2715, March 1976.
6. Middleton, W.D., and Lundry, J. L., "A system for Aerodynamic Design and Analysis of Supersonic Aircraft", Sept. 1980
   Part 1 - "General Description and Theoretical Development"; NASA CR-3351
   Part 2 - "User's Manual"; NASA CR-3353
   Part 3 - "Computer Program Description", NASA CR-3353
   Part 4 - "Test Cases", NASA CR-3354
7. Hollenback, D.M., and Blom, G.A., “Applications of a parabolized Navier-Stokes Code to an HSCT Configuration and Comparison to Wind Tunnel Data”, AIAA-93-3537, August 1993
8. Blom, G.A., Ball, D.N., Bussoletti, J.E., and Yu, N.J., “Computations of the Supersonic Flow Over an HSCT Type Configuration and Comparison With Wind Tunnel Data”, AIAA-91-3290, Sept. 1991
9. Kulfan, R. M., Friebel, G. O., Lord, B. J. and Yoshihara, H., "Application of Supersonic Favorable Aerodynamic Interference to Fighter Type Aircraft". AFFDL-TR-78-33, April 1978.
10. Morris, O. A. and Mack, R. J., "Aerodynamic Characteristics of a Parasol-Wing-Body Combination Utilizing Favorable Lift Interference at Mach Numbers from 3.00 to 4.63", NASA TN D-4855, Oct 1968
11. Ward, G. N., LINEARIZED THEORY OF STEADY HIGH-SPEED FLOW, Cambridge University Press, 1955, Pg 50-51
12. Robinson, A. and Laurmann, J. A., WING THEORY, Cambridge University Press, 1956, pp 320-323
13. Jones, R. T.; "Leading Edge Singularities in Thin - Airfoil Theory," Journal of the Aeronautical Sciences, Vol 17, No. 5, pp 307-310, May 1950
14. Jones, R. T., and Van Dyke, M. D.: "The Compressibility Rule for Drag of Airfoil Noses," Journal of the Aeronautical Sciences, Vol 25, No. 3, pp 171-172, 180, March 1958
15. Kulfan, B. M., “A New Supersonic Wing Far-Field Composite Element Wave Drag Optimization Method, “FCE””, AIAA-2008-0132, January 2008
16. von Karman, Th. “The Problem of Resistance in Compressible Fluids”, Atti del V Convegno della, “Fondazione Alessandro Volta Congress”, Rome 1935, pp. 222-276
17. Ashley, H. and Landahl, M., AERODYNAMICS OF WINGS AND BODIES, Addison – Wesley Publishing Co., 1965.
18. Lighthill, M. J., “Supersonic Flow Past Slender Bodies of Revolution the Shape of Whose Meridian Section is Discontinuous”, Quart J. Mech. App. Math, Vol. 1, Part 1, March 1948
19. Lighthill, M. J., “Higher Approximations”, GENERAL THEORY OF HIGH SPEED AERODYNAMICS, Volume VI of High Speed Aerodynamics and Jet Propulsion, Princeton University Press, 1954
20. Kulfan, R.M., “Aerodynamics Program TEA-210, Pressures on Bodies of Revolution at Supersonic Speeds”, Unpublished Boeing Note, November 1970
21. von Karman, T., “Supersonic Aerodynamics – Principles and Applications”, J. Aero. Sci., No. 14, pp 373-409, 1947
22. Sears,W.R., “On Projectiles of Minimum Wave Drag”, Quart Appl Math, Vol IV, No. 4, 1947, pp 361-366
23. Nielson, J. N., MISSILE AERODYNAMICS, McGraw Book Company, 1960

24. Eminton, E., and Lord, W. T., “Note on the Numerical Evaluation of the Wave Drag of Smooth Slender Bodies Using Optimum Area Distributions for Minimum Wave Drag”, Journal RAeS Technical Note. Vol.60, No. 1 , Jan. 19561
25. Harris, Jr., R.V. "A Numercial Technique for Analysis of Wave Drag at Lifting Conditions" NASA TV D-3586, Oct. 1966
26. Whitcomb, R.T., “A Study of the Zero-Lift Drag-Rise Characteristics of Wing-Body Combinations Near the Speed of Sound”, NACA RM-L52H08, September 1952
27. Hayes, W. D., “Linearized Supersonic Flow”, Cal. Tech Thesis, North American Aviation Report AL-222, 1947
28. Lomax, H. and Heaslet, M. A., “A Special Method for Finding Body Distortions that Reduce the Wave Drag of Wing and Body Combinations at Supersonic Speeds”, NACA RM A55B16, May 1955
29. Lomax, H. and Heaslet, M. A., “Recent Developments in the theory of Wing-Body Wave Drag”, J. Aeronautical Sci., vol. 23, no 12, pp 1061-1074, 1956
30. Lomax, H., "The Wave Drag of Arbitrary Configurations in Linearized Flow as Determined.by Areas and Forces in Oblique Planes.", NACA RM A55A18, 1955
31. Jones, R.T., “Theory of Wing-Body Drag at Supersonic Speeds”, NACA RM-A53H18a, Sept. 1953
32. Kulfan, B.M., "Aerodynamic Issues Involved in Sonic Flight", Boeing Technology Excellence Conference (BTEC), Transonic/Supersonic Aero-science Technology Session, July 12, 200
33. Jones, R. T. and Cohen, D., “Aerodynamics of Wings at High Speeds” pp 156-157, AERODYNAMIC COMPONENTS OF AIRCRAFT AT HIGH SPEEDS, Princeton University Press, 1957
34. Kulfan, R. M., and Sigalla, A. "Airframe-Propulsion System Aerodynamic Interference Predictions at High Transonic Mach Numbers Including Off-Design Engine Airflow Effects", Paper in AGARD Conference Proceedings No. 301, AERODYNAMICS OF POWER PLANT INSTALLATION, 1981
35. Sigalla, A; Hallstaff, T. H.: Aerodynamics of Powerplant Installation on Supersonic Aircraft, Journal of Aircraft, July-August 1967, pp 273-277
36. Kane, E. J.; and Middleton, W. D.: Considerations of Aerodynamic Interference in Supersonic Airplane Design, AGARD Conference on Aerodynamic Interference, Proceedings No. 71, paper 3, September 1970
37. Bencze, D. P., "Wind Tunnel Investigation of Nacelle-Airframe Interference at Mach Numbers of 0.9 to 1.4", NASA TMX-62, 489; 1976
38. Bencze, D. P., "Wind Tunnel Investigation of Nacelle-Airframe Interference at Mach Numbers of 0.9 to 1.4", NASA TMX-73, 088, 1976
39. Bencze, D. P., "Experimental Evaluation of Nacelle-Airframe Interference Forces and Pressures at Mach Numbers of 0.9 to 1.4", NASA TMX-3321, March 1977
40. Kulfan, R. M., and Blissell, W. A., "Analysis of Nacelle Transonic Interference Test Data", Section 4.0 of "Advanced Concept Studies for Supersonic Vehicles", NASA CR-159244, MAy 1980
41. Boyd, J. A., "Optimal Utilization of Supersonic Favorable lnterference to Obtain High Lift-Drag Ratios", AlAA Paper 65-752. November 1965.
42. Chen. C. F., and Clarke, J. H., "A Study of Configurations Composed of a Body Under a Lifting Wing in Supersonic Flow", Air Force Office of Scientific Research TN 59.1276, 1960.
43. Chen. C. F.. and Clarke, J. H., "Body Under Lifting Wing," J.A.S., Vol 28, No. 7, pp 547-562, July 1961.
44. Clarke, J. H., "The Forces on Wing-Fuselage Combinations in Supersonic Flow", Boeing Document D1-82-0018, August 1959.
45. Cook, P. H., "Further Experimental Results on the Mutual lnterference Between Separated Wings and Bodies a tM=2.49", R.A.E. Tech. Report No. 66228, July 1966.
46. Kulfan, R.M. “Application of Hypersonic Favorable Aerodynamic Concepts to Supersonic Aircraft” AIAA 78-1458, Aug. 1978
47. Kulfan, R.M., “Application of Favorable Aerodynamic Interference to Supersonic Airplane Design”, SAE 901988, Oct. 1990
48. Carmichael, R.L. and Woodward, F.A., "An Integrated Approach to the Analysis and Design of Wings and Wing-Body Combinations in Supersonic Flow", NASA TN D-3685, Oct. 1966
49. Prandtl, L. and Tietjens, O. G., APPLIED HYDRO- AND AEROMECHANICS, Dover Publications, 1957
50. Carlson, H.W., and Maglieri, D. J., “Review of Sonic-Boom Generation Theory and Prediction Methods”, Journal of Acoustics Society of America 52, pd 675-685, 1972.
51. Carlson, H. W., Mack, R. J., and Morris, O. A., ”Sonic Boom Pressure-Field Estimation Techniques”, Journal of the Acoustical Society of America, vol 39, no 5 part 2, 1966, pages 510-518
52. Maglieri, D. J., and Plotkin, K. J., “Sonic Boom” , AEROACOUSTICS OF FLIGHT VEHICLES: THEORY AND PRACTICE, Vol 1 Chapter 10, NASA Reference Publication 1258, Vol. 1, WRDC TR 90-3052, Aug 1991
53. Sigalla, A.,"Note on Some Theoretical Aspects of Lift Produced Sonic Boom", Boeing Document D6-7996 TN, Sept.961
54. Kane, E.J., "Review of Current Sonic Boom Studies", Journal of Aircraft, VOL. 10, NO. 7, JULY 1973, pp 395-399
55. Kulfan, R. M., et al, “High Transonic Transport Study” , Final Report, NASA CR-114658